GALAXY FORMATION WITH ULTRALIGHT BOSONIC DARK MATTER

Dissertation
zur Erlangung des mathematisch-naturwissenschaftlichen Doktorgrades
"Doctor rerum naturalium"
der Georg-August-Universität Göttingen
im Promotionsstudiengang Physik
der Georg-August University School of Science (GAUSS)

vorgelegt von
Jan Veltmaat
aus Bietigheim-Bissingen
Göttingen, 2019

Betreuungsausschuss

Prof. Dr. Jens Niemeyer, Institut für Astrophysik, Universität Göttingen
Prof. Dr. Steffen Schumann, Institut für Theoretische Physik, Universität Göttingen

Mitglieder der Prüfungskommission

Referent:
Prof. Dr. Jens Niemeyer, Institut für Astrophysik, Universität Göttingen

Korreferent:
Prof. Dr. David Marsh, Institut für Astrophysik, Universität Göttingen

Weitere Mitglieder der Prüfungskommission:
Prof. Dr. Fabian Heidrich-Meisner, Institut für Theoretische Physik, Universität Göttingen
Prof. Dr. Wolfram Kollatschny, Institut für Astrophysik, Universität Göttingen
Prof. Dr. Steffen Schumann, Institut für Theoretische Physik, Universität Göttingen
Dr. Michael Wilczek, Max-Planck-Institut für Dynamik und Selbstorganisation, Göttingen

Tag der mündlichen Prüfung: 12.12.2019

Abstract

Ultralight bosonic particles forming a coherent state are dark matter candidates with distinctive wave-like behaviour on the scale of dwarf galaxies and below. In this thesis, a new simulation technique for ultralight bosonic dark matter, also called fuzzy dark matter, is developed and applied in zoom-in simulations of dwarf galaxy halos. When gas and star formation are not included in the simulations, it is found that halos contain solitonic cores in their centers reproducing previous results in the literature. The cores exhibit strong quasi-normal oscillations, which are possibly testable by observations. The results are inconclusive regarding the long-term evolution of the core mass. It is shown that the Fourier spectrum of the entire halo is related to the velocity distribution in collisionless N-body simulations in a simple way, contributing to a better understanding of the empirically-found core-halo mass relation. When gas and star formation are included, it is found that the collapsing baryonic component heats up the inner halo region, resulting in more compact and massive cores. Their radial profiles are determined by the inner halo velocity and the external potential sourced by the baryon density. This finding has direct consequences for observational constraints on fuzzy dark matter which are so far based on radial density profiles from dark matter only simulations.

Contents

List of Figures

Chapter 1

Introduction

Although dark matter is an integral constituent of the cosmological standard model (ΛCDM), its exact nature is still unknown. Since most trivial explanations like massive clumps of ordinary matter (MACHOs) are tightly constrained [5; 6; 7; 8], present-day dark matter research combines methods and theoretical framework from two large areas of physics: astrophysics and particle physics. Astrophysicists use increasingly precise observational data from telescopes to derive basic properties like abundance, temperature and interaction strengths. On the particle physics side, theorists look for natural extensions to the standard model of particle physics fulfilling these properties and laboratory experiments then try to detect the particle candidates - so far unsuccessfully. Within this broad picture, numerical simulations, the topic of this thesis, serve as a connection between observations of the late universe and fundamental properties of dark matter candidates. They are necessary because the formation of collapsed objects like galaxies or galaxy clusters involves many non-linear processes.

Sometimes motivated by alleged deviations between ΛCDM predictions and observations on the scale of dwarf galaxies and sometimes motivated by theories beyond the standard model of particle physics, fuzzy dark matter (FDM) has gained increased attention in the scientific community in recent years. FDM is described by an ultralight scalar field producing distinctive wave-like patterns in the density distribution. The absence of strong density gradients explains its name. In this thesis, implications for the detailed structure of dwarf galaxies are studied using 3D cosmological simulations. The simulations follow the formation process of dwarf galaxies in a realistic cosmological environment starting from small initial fluctuation of the cosmic density field. Their aim is to quantify and understand the properties of FDM halos in order to derive observational constraints on FDM model parameters. While simulations that only follow the dark matter part of FDM halo formation already exist in the literature [1; 9], this thesis presents the first high resolution simulations with ordinary matter included.

One major obstacle for FDM simulations is the requirement of dedicated numerical techniques. The author of this thesis together with his collaborators Bodo Schwabe and and Jens Niemeyer developed a new numerical method for cosmological structure formation with FDM. Using this method, the author conducted two suites of dwarf galaxy formation simulations. In the first suite, only the dark matter contribution to the cosmic matter field was simulated, neglecting the influence of gas and star formation. The second suite also includes ordinary matter. The results of both suites were published in *Physical Review D* [3; 4].

The thesis is organized as follows. Chapter 2 discusses the basic theory of cosmological structure formation, the state of knowledge about dwarf galaxies and theoretical aspects of the FDM model. In chapter 3, the numerical methods used in the following chapters are introduced with emphasis on techniques for FDM and the new hybrid approach. Chapters 4 and 5 present and discuss results from the two simulation suites. Finally, conclusions and possible directions for further research based on the findings in this thesis can be found in chapter 6.

Chapter 2

Theoretical Background

2.1 The ΛCDM model

Over the past century, our knowledge of the history of the universe has gradually increased leading to the development of the now widely accepted ΛCDM model of cosmology. Soon after Albert Einstein formulated the theory of general relativity in 1916, the isotropic and homogeneous Friedmann-Robertson-Walker (FRW) metric was proposed to describe the overall space-time shape of the universe.

$$ds^2 = dt^2 - a^2(t)\left(\frac{dr^2}{1-kr^2} + r^2 d\Omega^2\right) \tag{2.1}$$

Here, the spatial part of the metric is expressed in spherical coordinates with a radial component dr and angular component $d\Omega$. $k = +1, 0, -1$ determines if the geometry of space is closed, flat or open. a is the scale factor describing the expansion (or contraction) of the universe and in the case of $k = +1, -1$ the curvature radius. Wavelengths emitted at the time t_{em} and observed today, t_0, appear redshifted by a factor

$$1 + z = \frac{a(t_0)}{a(t_{em})}\,. \tag{2.2}$$

According to the Einstein equation of general relativity, the evolution of the scale factor is described by the Friedmann equation

$$H^2 + \frac{k}{a^2} = \frac{8\pi G}{3}\epsilon \tag{2.3}$$

To find a solution for a, energy density components ϵ with their respective equation of state parameters w and one initial value for $\dot{a}$, often expressed in terms of the Hubble parameter today $H_0 = \dot{a}(t_0)/a(t_0)$, have to be specified. The equation of state parameter determines how the energy density evolves with respect to the scale factor according to

$$\epsilon \sim a^{-3(1+w)} \tag{2.4}$$

Initially, some scientists favored a static universe with $H_0 = 0$ for aesthetic reasons. This requires an energy component with an equation of state parameter $w < -1/3$ or a cosmological constant, equivalent to $w = -1$, to balance the contraction effect of the matter content of the universe. However, Edwin Hubble measured in 1929 that nearby galaxies recede from the Milky Way [10], which was interpreted as cosmological expansion and the cosmological constant was abandoned.

Tracing the evolution of the expanding universe backwards in time shows that it was much denser and hotter in the past. This fact is commonly referred to as Hot Big Bang model. George Gamov and his student Ralph Alpher proposed two testable consequences of this model in the 1940s [11]. At about a redshift of $z = 1000$ the cosmic gas forms neutral atoms such that photons within the gas do not scatter off the electrons anymore, which were previously present in the ionized plasma. The photons released back then and redshifted in the meantime are detectable in form of the cosmic microwave background (CMB) today. This was first measured in 1964 by Arno Penzias and Robert Woodrow Wilson [12]. Going further back in time and to higher temperatures atomic nuclei are formed out of a plasma of protons and neutrons. The theory of Big Bang Nucleosynthesis predicts the relative abundances of elements in primordial gas.

A major pillar of modern cosmology is the theory of structure formation. It revolves around the question of how the state of the universe today with its inhomogeneous distribution of matter on scales smaller than ~ 100 Mpc (galaxies, galaxy clusters, etc.) has evolved out of a homogeneous distribution at earlier times. Assuming initially small perturbations of the otherwise homogeneous density field, the equations of motion of gas and radiation (in the early times dark matter was not considered) can be linearized with respect to overdensity and solved analytically. Before the first precision measurements of CMB anisotropies took place in the early 90s by the COBE satellite, the initial conditions for structure formation were hard to constrain and highly idealized set-ups were studied. Nevertheless, Harrison [13] and Zel'dovich [14] independently found in 1970 and 1972 that only a certain type of spectrum of initial perturbations, later called Harrison-Zel'dovich spectrum, can account for the observed galaxy distribution. The power spectrum of density perturbations is in this case given by $P(k) \sim k$.

An important development for the theoretical framework of cosmology was the theory of inflation in the 1980s by Guth and Linde [15; 16] - a phase of accelerated expansion in the very early universe. Originally proposed to explain the absence of magnetic monopoles it can also explain various properties of the initial state of the universe like the observed isotropy of the CMB: Before the start of inflation the entire observable universe was in causal contact which would not have been the case without an inflationary phase. Furthermore, it gives an explanation for the initially high degree of spatial flatness that is necessary because the universe would otherwise recollapse too early or expand too fast. Last but not least, vacuum fluctuations of the inflaton field, which drives inflation, are stretched to macroscopic scales. This provides a mechanism for the production of initial perturbations acting as seeds for structure formation.

Although Fritz Zwicky had already argued in 1933 that a much larger amount of mass than observable in the form of stars is needed to explain the high velocity dispersion of galaxies in the Coma Cluster [17], it was not until the 1970s that dark matter was widely considered in astronomy. At this time, extended analysis of galaxy clusters, as well as first measurements of rotation curves of disk galaxies gave further evidence for a large amount of matter not interacting significantly with electromagnetic radiation and, thus, only detectable via its gravitational influence. Subsequently, dark matter was incorporated into cosmological structure formation. While baryonic explanations for dark matter like black holes, brown dwarfs and white dwarfs were also considered, the idea that dark matter is composed of non-baryonic particles lead to a large number of proposed dark matter candidates motivated by particle physics. Those candidates were typically categorized according to their initial velocity dispersion into hot dark matter (HDM), for example massive neutrinos, warm dark matter (WDM) like gravitinos or sterile neutrinos and cold dark matter (CDM) like weakly interaction massive particles (WIMPs) or QCD axions. The higher the velocity dispersion of dark matter, the larger the length scale below which perturbations are suppressed due to free-streaming in the linear evolution of the density field. HDM was soon shown to disagree with observations of galaxy clustering for the above reason. The maximum allowed velocity dispersion for WDM has decreased more and more in recent years due to observations probing the smallest scales of the power spectrum like Lyman-α forest spectra [18].

As the latest addition to the cosmological standard model, the cosmological constant Λ, which also goes by the name dark energy, was reintroduced in the 1990s after galaxy surveys [19] and the first measurements of anisotropies in the CMB [20] favoured a flat universe which today contains ~ 70 % dark energy and ~ 30 % dark matter over other models like open universes or flat ones with 100 % matter domination. The late time effect of dark energy, the accelerated expansion of the universe, was detected in 1998 using supernova Ia data [21; 22].

Today, the ΛCDM model convincingly describes the large scale structure of the galaxy distribution as observed in galaxy surveys like the Sloan Digital Sky Survey

(SDSS) [23] and the CMB anisotropies as measured most precisely by the Planck satellite [24]. In its most basic form, the model assumes spatial flatness and contains 6 free parameters which have now been constrained up to ≈ 1 percent. From those 6 parameters other parameters like the today's energy densities of dark matter, baryons and dark energy can be derived. They are often expressed as fractions Ω of the critical density needed for a spatially flat universe given the Hubble parameter

$$\epsilon_{cr} = \frac{3H^2}{8\pi G} \tag{2.5}$$

2.1.1 Structure formation and halo properties

In agreement with cosmological measurements [24], a spatially flat universe is assumed in the following. The scale factor a can then be scaled arbitrarily. Comoving distances, used in the definition of the metric in equation (2.1), are translated to physical distances by a multiplication by a.

The evolution of a non-relativistic ideal fluid with Newtonian treatment of gravity in comoving coordinates is described by the following set of equations [25]

$$\frac{\partial \rho}{\partial t} + 3\frac{\dot{a}}{a}\rho + \frac{1}{a}\nabla(\rho \mathbf{v}) = 0 \quad \text{(continuity)} \tag{2.6}$$

$$\frac{\partial \mathbf{v}}{\partial t} + \frac{\dot{a}}{a}\mathbf{v} + \frac{1}{a}(\mathbf{v}\cdot\nabla)\mathbf{v} + \frac{1}{a}\frac{\nabla p}{\rho} + \frac{1}{a}\nabla V = 0 \quad \text{(Euler)} \tag{2.7}$$

$$\nabla^2 V = 4\pi G a^2(\rho - \bar{\rho}) \quad \text{(Poisson)} \tag{2.8}$$

Here, ρ denotes the density, $\mathbf{v}$ the velocity and p the pressure of the fluid. V is the gravitational potential and $\bar{\rho}$ the mean density. The above equations have only limited applicability in cosmological structure formation for several reasons. The Newtonian treatment of gravity is only valid on sub-horizon scales ($\ll cH^{-1}$), which can be understood as requiring that the expansion velocity must not be comparable to the speed of light so that the effect of gravity can be considered instantaneous. Moreover, the Euler equation only considers non-relativistic fluids. Due to the absence of collisions between individual particles, dark matter is not an ideal fluid in general. However, it can be described by the fluid equations with $p = 0$ as long as its velocity dispersion is negligible. In the case of CDM, this condition is fulfilled on all relevant length scales until first shell-crossing. In the case of WDM, the velocity dispersion is only negligible on length scales larger than the free-streaming length λ_{fs}.

For an ideal fluid the pressure is given by an equation of state of the form

$$p = p(\rho, S) \tag{2.9}$$

where S is the specific entropy. Thus, the term $\frac{\nabla p}{\rho}$ can be expressed as

$$\frac{\nabla p}{\rho} = \frac{1}{\rho}\left[\left(\frac{\partial p}{\partial \rho}\right)_S \nabla\rho + \left(\frac{\partial p}{\partial S}\right)_\rho \nabla S\right] = \frac{1}{\rho}\left[c_s^2 \nabla\rho + \sigma\nabla S\right] , \tag{2.10}$$

where $c_s = (\partial p/\partial\rho)_S^{1/2}$ is the adiabatic sound speed. After writing $\rho = \bar{\rho}(1+\delta)$ and keeping only linear terms in δ and $\mathbf{v}$ and using equation (2.10) the fluid equations read

$$\frac{\partial\delta}{\partial t} + \frac{1}{a}\nabla\cdot\mathbf{v} = 0 \tag{2.11}$$

$$\frac{\partial\mathbf{v}}{\partial t} + \frac{\dot{a}}{a}\mathbf{v} + \frac{c_s^2}{a}\nabla\delta + \frac{\sigma}{a\bar{\rho}}\nabla S + \frac{1}{a}\nabla V = 0 \tag{2.12}$$

$$\nabla^2 V = 4\pi G a^2 \bar{\rho}\delta \tag{2.13}$$

Differentiating equation (2.11) with respect to t and using equations (2.12) and (2.13) gives

$$\frac{\partial^2\delta}{\partial t^2} + 2\frac{\dot{a}}{a}\frac{\partial\delta}{\partial t} = 4\pi G\bar{\rho}\delta + \frac{c_s^2}{a^2}\nabla^2\delta + \frac{\sigma}{a\bar{\rho}}\nabla S \tag{2.14}$$

This partial differential equation becomes an ordinary differential equation after applying the Fourier transformation.

$$\frac{\partial^2\delta_\mathbf{k}}{\partial t^2} + 2\frac{\dot{a}}{a}\frac{\partial\delta_\mathbf{k}}{\partial t} = \left[4\pi G\bar{\rho} - \frac{k^2 c_s^2}{a^2}\right]\delta_\mathbf{k} - \frac{\sigma k^2}{a\bar{\rho}}S_\mathbf{k} \tag{2.15}$$

In the special case of a pressureless fluid without entropy perturbations the equation reads

$$\frac{\partial^2\delta_\mathbf{k}}{\partial t^2} + 2\frac{\dot{a}}{a}\frac{\partial\delta_\mathbf{k}}{\partial t} = 4\pi G\bar{\rho}\delta_\mathbf{k} \tag{2.16}$$

It has the general solution [25]

$$\delta_{\mathbf{k}} = C_1 H \int \frac{\mathrm{d}t}{a^2 H^2} + C_2 H \tag{2.17}$$

where the first term is the growing mode and the second one is the decaying mode. This solution is applicable to the linear evolution of CDM on sub-horizon scales after it has decoupled from the baryonic particles under the assumption that gravity is dominated by dark matter perturbations. In the case of a flat matter-dominated universe it becomes

$$\delta_{\mathbf{k}} = C_1 t^{2/3} + C_2 t^{-1} \tag{2.18}$$

A Gaussian random field is completely specified in the statistical sense by its power spectrum $P(k)$

$$\langle \delta_{\mathbf{k_1}} \delta_{\mathbf{k_2}} \rangle = V_u^{-1} P(k) \delta_{\mathbf{k_1 k_2}} \tag{2.19}$$

where V_u is a large volume in which the density field is assumed to be periodic (it enters in the definition of the Fourier transform $\delta_{\mathbf{k}}$) and $\delta_{\mathbf{k_1 k_2}}$ is the Kronecker delta. This means that different Fourier modes are uncorrelated. The probability distribution for the real and imaginary parts of a single mode is a Gaussian distribution around 0 with a variance of $V_u^{-1} P(k)$. Data from the Planck satellite [24] is in agreement with a Gaussian spectrum of adiabatic initial conditions with a power spectrum close to the Harrison-Zel'dovich one ($P(k) \sim k$). "Adiabatic" means that entropy perturbations are not present corresponding to $S_{\mathbf{k}} = 0$ in the treatment above. Such a spectrum is a natural outcome of single field inflation models.

Since Fourier modes evolve independently in the linear theory, the spectrum of cosmological perturbations remains Gaussian until non-linear evolution sets in. The power spectrum after recombination is often expressed in terms of the initial spectrum $P_i(k)$ as

$$P(k,t) = P_i(k) T^2(k) D^2(t) \tag{2.20}$$

where $D(t)$ is the growing mode (C_1) in equation (2.17). $T(k)$ is the transfer function, which encapsulates all deviations from the sub-horizon pressureless fluid description of $D(t)$. The most important of those effects stems from the fact that, due to cosmic expansion and the different equation of state parameters in equation (2.4), there is a transition between radiation-domination to matter-domination at around $z \approx 3000$. In comparison to super-horizon modes, whose evolution can be computed by linearizing the general relativistic equations of motion, the sub-horizon modes grow extremely slowly during radiation domination. This imprints a characteristic tilt from the initial $\sim k$ scaling to a $\sim k^{-3}$ scaling at large k into the power spectrum. In the case of warm dark matter with a non-vanishing velocity dispersion, free-streaming leads to a suppression of modes below the free-streaming length corresponding to sharp decline of the power spectrum at large k. Minor changes to the total power spectrum are introduced by the baryonic fraction of the cosmic matter density. One effect is caused by the non-vanishing pressure of the baryon-photon plasma prior to recombination. This is apparent in equation (2.15): If $k > c_s^{-1} a \sqrt{4\pi G\bar{\rho}}$ the solution becomes oscillatory instead of growing. Since these baryonic acoustic oscillations take place only before recombination and the baryon fraction is low, the amplitude of the resulting oscillatory pattern the power spectrum is small. However, it is still observable in the galaxy-galaxy correlation function. Apart from that, the imperfect coupling between photons and baryons before recombination allows for long mean-free paths of photons and, in turn, photon diffusion which damps small scale perturbations in the baryon power spectrum further (Silk damping).

When perturbations have grown so much that δ becomes of order unity, the linearized equations of motion are invalid. Insight into the nonlinear evolution can be gained analytically by using approximations or by studying idealized situations. For example, in the case of a one-dimensional perturbation, matter elements move along the following trajectories according to the pressureless fluid equations:

$$\mathbf{x} = \mathbf{x_i} - \frac{D(t)}{4\pi G\bar{\rho}a^3}\nabla V_i(\mathbf{x_i}) \tag{2.21}$$

$$\mathbf{v} = -\frac{\dot{D}(t)}{4\pi G\bar{\rho}a^2}\nabla V_i(\mathbf{x_i}) \tag{2.22}$$

In the Zel'dovich approximation [26], these equations are also used for 3-dimensional perturbation fields. This is only approximately correct and, while linear evolution is reproduced, the error grows with increasing overdensity δ. An important prediction of the Zel'dovich approximation is that in regions where a perturbation along a certain direction dominates over the other directions, the density field will form 2-dimensional sheets, the so-called pancakes. In any case, the Zel'dovich approximation becomes invalid, when the trajectories of matter elements cross each other (shell-crossing).

Besides one-dimensional perturbations, the case of a perfectly spherical overdensity also allows for an analytical solution for nonlinear collapse. The physical radius of of a mass shell in the overdensity is given by the equation [27]

$$\frac{\mathrm{d}^2 r}{\mathrm{d}t^2} = -\frac{GM}{r^2} + \frac{\Lambda}{3} r \tag{2.23}$$

where M is the enclosed mass and Λ the cosmological constant. Initially, the radius nearly expands like the rest of the universe ($\dot{r}_i / r_i \approx H_i$). Due to the enclosed overdensity, the expansion slows down, turns around and the sphere eventually collapses. Although overdensities with perfect spherical symmetry do not exist in the cosmological density field, the solution to the spherical collapse problem is often invoked for the analysis of non-linear collapse. Two important quantities stand out: Firstly, it is possible to relate the time of collapse of a spherical mass shell to the overdensity δ that it encloses initially. This overdensity can also be expressed in terms of the value it would have according to linear theory at the time of collapse. The computation yields a nearly time indepedent value $\delta_c \approx 1.686$. This critical overdensity is used in the Press-Schechter formalism to predict the halo mass function out of the linear perturbation spectrum [28]. Secondly, the total energy of a sphere is conserved and is given completely in the form of gravitational potential energy at the turnaround. According to the virial theorem, the energy should eventually be distributed in the following way:

$$-2K = W \tag{2.24}$$

where K is the kinetic and W the potential energy. This condititon leads to a characteristic average overdensity of the final virialized object. For a flat universe with cosmological constant it reads [29]

$$\zeta \approx (18\pi^2 + 82[\Omega_m(t) - 1] - 39[\Omega_m(t) - 1]^2)/\Omega_m(t) \tag{2.25}$$

This value often serves as a definition for virial radius and virial mass in the analysis of simulation results.

In general, dark matter in the non-relativistic sub-horizon regime is described by the Vlasov equation for the phase space density $f(\mathbf{x}, \mathbf{p} \equiv ma^2\dot{\mathbf{x}}, t)$ [25]

$$\frac{\partial f}{\partial t} + \frac{1}{ma^2}\mathbf{p} \cdot \nabla f - m\nabla V \frac{\partial f}{\partial \mathbf{p}} = 0 \tag{2.26}$$

In comparison to solving for the 6-dimensional phase space density directly, it is less computationally expensive to employ N-body simulations for studying non-linear structure formation of CDM. The basic procedure is to initialize a set of particles according to the Zel'dovich approximation (equations (2.21) and (2.22)) at a time when perturbations are still linear and then to evolve them under the gravitational influence of the other particles. This can be understood as a Monte-Carlo sampling of the phase space density in the Vlasov equation. Even though basic properties of non-linear structure formation can be derived with analytical arguments, numerical simulations are necessary to obtain a full picture which can be linked to observations of galaxy distribution, for example. On length scales right below the scale where the universe is homogeneous (today ≈ 100 Mpc), dark matter forms the so-called 'cosmic web' consisting of 2-dimensional walls (the pancakes predicted by the Zel'dovich approximation), which connect 1-dimensional filaments, which connect spherical halos of dark matter. Going to smaller scales, gravitational collapse has already progressed further resulting in the fact that walls, filaments and large halos themselves consist of smaller halos. Numerical simulations also make predictions for the internal properties of dark matter halos, which is nearly impossible analytically. Their radial density profile, for example, was shown to be universally described by the Navarro-Frenk-White profile [30]:

$$\rho(r) = \frac{4\rho_s}{(r/r_s)(1 + r/r_s)^2} \tag{2.27}$$

where r_s is a characteristic radius marking a tilt from a central r^{-1} behaviour to a r^{-3} scaling and ρ_s is the density at that radius.

After recombination, baryons lose the additional pressure support formerly provided by the photons. In turn, they fall into the potential wells that dark matter has already built up. If the virial temperature of a halo exceeds 10^4 K primordial gas can cool by means of atomic processes which radiate photons. This allows the gas to contract more than the dark matter component and eventually form a galaxy. The formation of stars complicates the process further as the additional energy gained by nuclear fusion has a significant impact on the environment of the stars. Supernova explosions inject a large amount of energy into the interstellar medium preventing further star formation or even expelling gas from the halo. Highly energetic UV radiation from massive stars permeates the universe and leads to a reionization of the cosmic gas at around $z = 6 - 10$ and provides further heating.

The details of galaxy formation and evolution seem infinitely complex due to the many physical processes and many length and time scales involved. The discussion above does not mention the role of active galactic nuclei or mergers between galaxies, for example. Because of its relevance for the general topic of this thesis, the next chapter focuses on a special type of galaxy.

2.2 Dwarf galaxies

Galaxies at the low luminosity end of the distribution of galaxies are called 'dwarf galaxies'. It was observed that the surface brightness profiles of galaxies with magnitudes $M_B \gtrsim -18$ are better described by an exponential law instead of the Vaucouleurs law $\mathrm{R}^{1/4}$ which describes brighter galaxies [25; 31; 32]. However, more recent results show that both populations can be described by a Sérsic profile with a Sérsic index that is smoothly varying with brightness [25; 33]. Hence, the distinction between 'dwarf' galaxies and 'regular' galaxies is mostly due to historical reasons and the threshold of $M_B \sim -18$, which roughly corresponds to a stellar mass of $M_* \sim 10^9$ $\mathrm{M}_\odot$ and a virial mass of $M_h \sim 10^{11}$ $\mathrm{M}_\odot$, is somewhat arbitrary [25].

Dwarf galaxies are by number the most abundant type of galaxies in the universe but contain only a small fraction of the total number of stars [25]. With the faintest galaxy discovered so far having an absolute magnitude of $M_V \approx 0.0$ [34], dwarf galaxies span a larger range of magnitudes than 'regular' galaxies. Their morphological properties are also diverse. A distinction can be made between gas-rich galaxies with ongoing star formation, so called dwarf irregulars (dIrr), and gas-poor ones without young stars, the dwarf spheroidal (dSph) and dwarf ellipticals (dE) [25]. Bright dwarf irregulars often contain rotating gas disks [25]. Dwarf spheroidal galaxies have a very low surface brightness and a relatively regular shape [25]. They include the subgroup of ultrafaint dwarf galaxies which are the faintest galaxies discovered so far with stellar masses of $M_* \approx 10^{2-5}$ $\mathrm{M}_\odot$. Many known dwarf galaxies are satellite galaxies of larger galaxies but field dwarfs are also known to exist. The majority of field dwarfs are dwarf irregulars whereas most dwarf spheroidals are satellite galaxies [35].

Because of their low luminosity, the detection of dwarf galaxies is limited to the local universe. While brighter dwarf galaxies have been observed in nearby galaxy clusters like Virgo or Fornax, the maximum observable distance decreases with decreasing luminosity. The only known ultrafaint dwarf galaxies, for example, are satellites of the Milky Way. The detection of new dwarf galaxies and the study of their properties is an active field of research. The number of known systems has been steadily increasing over the past years owing to large-area digital sky surveys like the Sloan Digital Sky Survey (SDSS) [36; 37; 38], the Pan-Andromeda Archaeological Survey (PAndAS) [39] and the Dark Energy survey (DES) [34; 40; 41]. Today, ~ 59 satellite galaxies of the Milky Way are known which is ~ 5 times more than in the year 2004. Equally, the stellar mass of the smallest known dwarf has decreased from $M_* \approx 5 \times 10^5$ $\mathrm{M}_\odot$ in the year 2004 to more than 1000 times less [35]. Future telescopes like the Large Synoptic Survey Telescope will push the boundary of detectability even further.

As the amount of observational data on dwarf galaxies increases, more effort is being put into the task to understand their properties and formation history within the ΛCDM framework. The most naive interpretations of cosmological dark-matter-only simulations have shown to disagree with observations. In fact, dwarf galaxies are at the core of the three often-cited problems that the ΛCDM model faces on small scales, the missing-satellite problem, the cusp-core problem and the too-big-to-fail problem.

2.2.1 Missing satellites

The missing-satellite problem consists of an apparent mismatch between the number of low-mass halos predicted by ΛCDM and the number of observed dwarf galaxies [42; 43]. High-resolution cosmological N-body simulations show that dark matter halos exist at all masses and there is no minimum halo mass. The halo mass function rises steeply with decreasing mass with $\mathrm{d}n/\mathrm{d}M \sim M^{-1.9}$. Comparing the numbers, one expects thousands of subhalos in the Milky Way halo that could support molecular cooling ($M_h \gtrsim 10^7$ M$_\odot$ [44; 45]) and, thus, are in principle able to form stars [35]. On the other hand, we only know ~ 59 Milky Way satellites today and it is not to be expected that future surveys can find enough satellites to alleviate this discrepancy. Taking the ΛCDM model for granted, it is therefore obvious that a linear relation between halo mass M_h and and stellar mass M_* of the type

$$M_* = \epsilon_* f_b M_h \tag{2.28}$$

with a constant efficiency ϵ_* and the cosmic baryon fraction $f_b = \Omega_b/\Omega_m$ cannot exist. Instead, the efficiency must vary with halo mass and become zero for low mass halos. One way to find the relation between M_* and M_h is abundance matching. Starting from the most massive ones, the number density of dark matter halos is matched with the most massive observed galaxies that are not yet associated with more massive halos. A more sophisticated model is presented in [46] with a ratio up to 10^3 between M_h and M_*. Extrapolating to ultrafaint dwarfs ($M_h \lesssim 10^9$ M$_\odot$) yields even higher ratios. Such high mass-to-light ratios are in agreement with kinematic measurements of the dark matter mass of dwarf galaxies. These can be done either by measuring the rotation velocity of gas disks [35; 47], which is only possible for bright dwarfs ($M_h \gtrsim 10^{10}$ M$_\odot$) containing disks, or by measuring the stellar velocity dispersion [35; 48; 49; 50; 51]. The measurements yield mass-to-light ratios up to ~ 1000 times the ratio of the sun [35]. Thus, dwarf galaxies, especially ultrafaint ones, are the most dark matter dominated systems in the universe.

Under the assumption that the ΛCDM model is correct, the explanation for the small number of dwarf galaxies and their high mass-to-light ratio must be found in the physics of the baryonic component of galaxies. Supported by numerical simulations [52; 53; 54; 55; 56; 57], two effects have been identified as the most relevant: The UV background responsible for the reionization of the universe leads to a heating of the gas in low mass halos and suppresses gas accretion. Apart from that, if the UV background does not shut off star formation completely, stellar feedback by supernova explosions inside the low mass halos inhibits further star formation and expels large fractions of the gas from the halo's potential well.

Heating by the UV background prevents star formation at halo masses below $M_h \approx 10^9$ M$_\odot$ [35; 58; 59] which is roughly the size of ultrafaint dwarfs. Consequently, it is debated, with the support of observations [60] and simulations [57; 61; 62], whether ultrafaint dwarfs could be so-called 'fossils' of reionization with all their stars having formed before UV radiation eventually prevented additional gas accretion [63].

Apart from UV background and stellar feedback, the baryon fraction in satellite dwarfs can be affected by ram pressure stripping and tidal stripping [27; 64].

2.2.2 Cusp-core controversy

Cosmological dark-matter-only simulations predict that the NFW-profile is more or less universally applicable to all halo masses [30]. The profile has a steeply increasing density towards the center with $\rho \sim r^{-1}$ forming a 'cusp'. Such a cuspy profile is, however, in disagreement with measurements of rotation curves of gas disks in bright dwarf galaxies preferring constant ('cored') central density profiles [47; 65; 66; 67; 68]. For low mass dwarf spheroidal galaxies, similar results can obtained by Jeans analysis of stellar kinematics [69; 70]. However, these methods are less reliable because of the degeneracy of mass and anisotropy in such models [71]. Analysis methods based on different stellar populations also favour cores [72]. Taking into account the uncertainties of the methods and the fact that some results favour cuspy profiles [70; 73] one can summarize that, in contrast to brighter dwarf galaxies, the evidence for cored profiles in dwarf spheroidal galaxies is less firm.

Like in the case of the missing-satellite problem, many researchers have pointed out that the discrepancy is probably a result of an overinterpretation of dark-matter-only simulations neglecting baryonic effects. Indeed, various numerical studies show that the repeated expulsions of gas caused by supernova explosions lead to temporal fluctuations of the central gravitational potential and, in turn, to cored dark matter density profiles in dwarf galaxies [35; 53; 57; 74; 75; 76; 77; 78]. Most simulation results [57; 77; 78] agree that the ability to form cores is limited to a certain range of stellar masses with a peak at $M_* = 10^{8-9}$ M$_\odot$ corresponding to bright dwarfs ($M_h \approx 10^{11}$ M$_\odot$). Below $M_* \approx 10^6$ M$_\odot$ there are not enough stars being formed to move gas outwards by supernova explosions. However, as discussed above, there is less observational evidence for cores at these mass scales (discussed further in the next section). Owing to the variety of subgrid models and resolution choices, some numerical results deviate from the above picture. While [55] do not produce cores in any of their halos, [79] see cores in halos of all masses.

Another mechanism proposed to turn cuspy profiles into cores is dynamical friction of cold gas clumps transferring energy to the dark matter component in a halo [80; 81; 82].

2.2.3 Too-big-to-fail

As pointed out by Boylan-Kolchin et al. [83; 84], the central masses of the most massive subhalos produced in dark matter only simulations of Milky Way-like systems do not agree with the observed central mass of any Milky Way satellite. Instead, the simulated subhalos are too dense in the center. On the one hand, the favoured mechanisms for the solution of the missing-satellites problem cannot be invoked here, because the subhalos are too massive for reionization and supernova feedback to prevent star formation. Thus, the simulated massive subhalos should host an observable satellite galaxy. This explains the name of the problem. On the other hand, the relevant Milky Way satellites have stellar masses around $M_* \approx 10^6\ \mathrm{M}_\odot$ which is the scale where stellar feedback becomes inefficient at moving dark matter outwards and thereby reducing the central density. This makes the high central densities of simulated subhalos harder to explain. Supported by hydrodynamical simulations, it is often argued that environmental effects like tidal stripping, disk shocking and ram pressure stripping can account for the discrepancy [35; 55; 85; 86].

2.3 Alternatives to CDM

To summarize the last section, it is debatable if the small scale problems exist at all or if they simply result from insufficient modelling of baryonic physics in cosmological simulations. Still, it is viable to consider solutions involving alternatives to the CDM paradigm under the constraint that the successes of ΛCDM on large cosmological scales are preserved. If baryonic explanations turn out to be insufficient, alternative dark matter models might at least play a supportive role in explaining the small scale problems.

Baryonic solutions to the missing-satellite problem rely on the fact that of the many small subhalos of the Milky Way only the most massive ones host galaxies. A more radical solution is to reduce the number of small halos by changing the behaviour of dark matter. Warm dark matter with a mass that is still allowed by Lyman-α forest constraints is one simple way to achieve this. If thermally produced, the WDM mass m_{WDM} is related to its velocity dispersion and, thus, to the effective free-streaming scale λ_{fs} according to [87]

$$\lambda_{fs} = 0.07 \left(\frac{m_{WDM}}{1\ \text{keV}}\right)^{-1.11} \left(\frac{\Omega_{DM}}{0.25}\right)^{0.11} \left(\frac{H_0}{70\ \text{km/s/Mpc}}\right)^{0.22} \text{Mpc}\,. \tag{2.29}$$

The suppression of power at large wavenumbers k caused by free-streaming in the linear regime leads to fewer small dark matter halos [88]. Furthermore, WDM can help to alleviate the too-big-too-fail problem, because halos of a given size form later with WDM compared to CDM leading to a reduced central density [35; 89]. However, WDM is unable to explain the presence of cores in bright dwarf galaxies of the local group (cusp-core problem). Although a thermal velocity distribution of dark matter can produce cored profiles, the necessary WDM mass to agree with observations is so low ($m_{WDM} \sim 0.1$ keV) that it prevents the formation of the halo in the first place [90] and is ruled out by Lyman-α forest constraints ($m_{WDM} > 3.5$ keV) [18].

The cusp-core problem can be addressed by self-interacting dark matter (SIDM). Self-interactions between dark matter particles with a cross-section per unit mass of $\sigma/m = 0.45 - 450\ \text{cm}^2/\text{g}$ increases the entropy of dark matter in high density environments like centers of halos and this flattens the density profile [91]. Such a high cross-section is in tension with the central densities of galaxy clusters [92], which can be solved by considering velocity dependent cross-sections $\sigma(v)$ [35]. SIDM alone does not have an effect on the halo mass function and, thus, cannot explain the missing-satellite problem.

2.4 Fuzzy dark matter

An alternative dark matter model to explain the small scale tensions was proposed by Hu, Barkana and Gruzinov [93] in 2000, although the idea that dark matter is a light scalar field had been around before that [94]. In the fuzzy dark matter model, dark matter consists of ultralight bosonic particles with negligible self-interaction. They form a coherent state governed by the Lagrangian of a classical real scalar field

$$\mathcal{L} = \frac{\hbar^2}{2} g^{\mu\nu} \partial_\mu \Phi \partial_\nu \Phi - \frac{1}{2} m^2 c^2 \Phi^2 \tag{2.30}$$

The corresponding equation of motion is the Klein-Gordon equation

$$\Box\Phi - \frac{m^2c^2}{\hbar^2}\Phi = 0 \tag{2.31}$$

On a curved space-time, the d'Alembert operator is given by

$$\Box = \frac{1}{\sqrt{-g}}\partial_\mu[\sqrt{-g}g^{\mu\nu}\partial_\nu] \tag{2.32}$$

If one is interested in the behaviour of FDM on sub-horizon scales, it is prudent to consider the non-relativistic limit with Newtonian gravity. This is achieved by considering only small scalar perturbations V to the FRW metric in Newtonian gauge, factoring out fast oscillations due to the rest mass energy

$$\Phi = \frac{1}{\sqrt{2ma^3}}\left(\Psi \mathrm{e}^{-\frac{imc^2t}{\hbar}} + \Psi^* \mathrm{e}^{\frac{imc^2t}{\hbar}}\right) \tag{2.33}$$

and keeping in the equation of motion for Ψ only the linear terms in $\hbar\dot{\Psi}$, $\hbar^2\nabla^2\Psi$ and V [95]. The result is the well-known Schrödinger equation

$$i\hbar\dot{\Psi} = -\frac{\hbar^2}{2ma^2}\nabla^2\Psi + Vm\Psi\,, \tag{2.34}$$

where V is the Newtonian gravitational potential given by the Poisson equation (equation (2.8))

$$\nabla^2 V = 4\pi G a^2(\rho - \bar{\rho}) \tag{2.35}$$

The scalar field contributes in the following way to the mass density with spatial average $\bar{\rho}$:

$$\rho = ma^{-3}|\Psi|^2 \tag{2.36}$$

If the mass of the scalar field is chosen to be $m \approx 10^{-22}$ eV, the de Broglie wavelength $\lambda_{db} = 2\pi\hbar/mv$ becomes of the order of kiloparsecs in dwarf galaxy halos. Analogous to the uncertainty principle of quantum mechanics, this prevents the formation of cuspy density profiles. Approximately the same mass is necessary to achieve a suppression of the linear power spectrum at large k, in order to have an effect on the abundance of low mass halos similar to the WDM solution to the missing-satellites problem. Thus, FDM is potentially an elegant solution to the small scale problems of ΛCDM as it relies on a single mechanism to explain all of them.

To get an understanding of the linear evolution of FDM, the Schrödinger-

Poisson system can be cast to a similar form as the non-relativistic fluid equations (equations (2.6) to (2.8)) using the Madelung transformation [96]. Substituting

$$\Psi = \sqrt{\frac{\rho(\mathbf{x},t)a^3}{m}}\exp(iS(\mathbf{x},t)/\hbar) \tag{2.37}$$

and $\mathbf{v} = (ma)^{-1}\nabla S$ and separating real and imaginary parts yields

$$\frac{\partial\rho}{\partial t} + 3\frac{\dot{a}}{a}\rho + \frac{1}{a}\nabla(\rho\mathbf{v}) = 0 \tag{2.38}$$

$$\frac{\partial\mathbf{v}}{\partial t} + \frac{\dot{a}}{a}\mathbf{v} + \frac{1}{a}(\mathbf{v}\cdot\nabla)\mathbf{v} + \frac{\hbar^2}{2m^2a^3}\nabla\frac{\nabla^2\sqrt{\rho}}{\sqrt{\rho}} + \frac{1}{a}\nabla V = 0 \tag{2.39}$$

These equations are exactly the continuity and euler equations, but with the hydrodynamic pressure replaced by a term involving the second derivative of the density field. The quantity

$$Q = \frac{\hbar^2}{2m^2a^2}\frac{\nabla^2\sqrt{\rho}}{\sqrt{\rho}} \tag{2.40}$$

is often called 'quantum pressure' for this reason. Analogous to section 2.1.1 the equations can by linearized and combined to give [97]

$$\frac{\partial^2\delta}{\partial t^2} + 2\frac{\dot{a}}{a}\frac{\partial\delta}{\partial t} = 4\pi G\bar{\rho}\delta + \frac{\hbar^2}{4m^2a^4}\nabla^2\nabla^2\delta \tag{2.41}$$

After applying the Fourier transformation this becomes

$$\frac{\partial^2\delta_{\mathbf{k}}}{\partial t^2} + 2\frac{\dot{a}}{a}\frac{\partial\delta_{\mathbf{k}}}{\partial t} = \left[4\pi G\bar{\rho} - \frac{\hbar^2k^4}{4m^2a^4}\right]\delta_{\mathbf{k}} \tag{2.42}$$

This shows that, similar to the pressure of the baryon-photon plasma before recombination, the quantum pressure introduces a Jeans scale

$$k_J = 2\pi^{1/4}\hbar^{-1/2}a(G\bar{\rho})^{1/4}m^{1/2} \tag{2.43}$$

Perturbations with $k < k_J$ grow, while perturbations with larger wavenumbers undergo oscillations. Since $\bar{\rho} \sim a^{-3}$ during matter-domination, the comoving Jeans scale changes only mildly ($k_J \sim a^{1/4}$). This leads to a cut-off in the power spectrum which is sharper than the one introduced by WDM free-streaming [98]. The effect can be expressed as a transfer function $T(k)$ relative to the ΛCDM

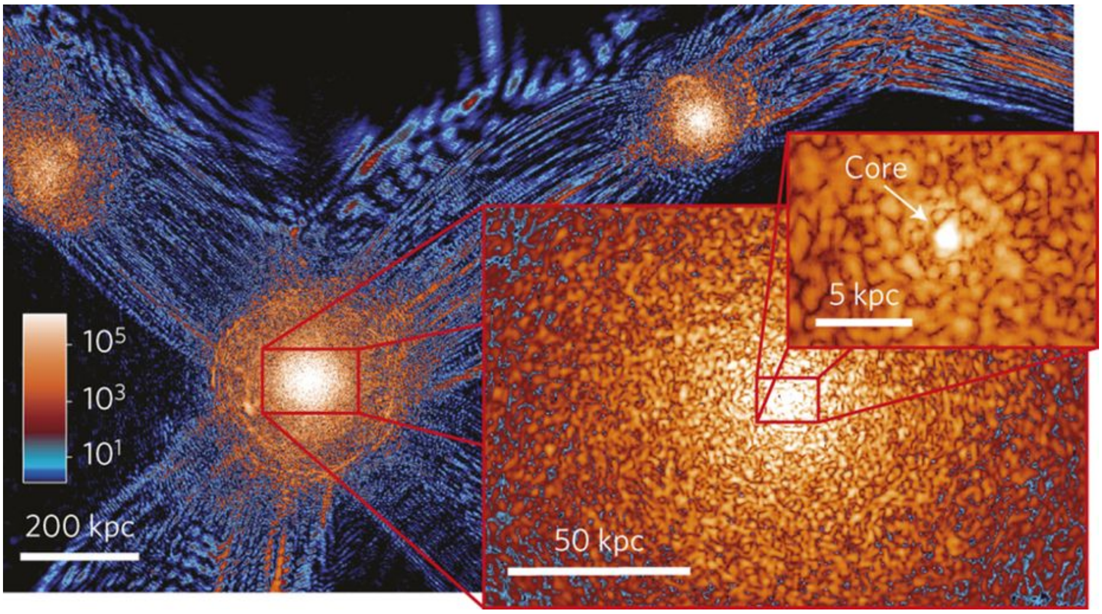

Figure 2.1: Cosmological FDM simulation with a zoom-in on the central region of a halo.
Reprinted by permission from Springer Nature: Nature Physics [1] © 2014

prediction [93]

$$P_{SFDM}(k,z) = T^2(k) P_{CDM}(k,z) \tag{2.44}$$

where $T(k)$ can be approximated by the analytical expression

$$T(k) = \frac{\cos x^3}{1+x^8} \tag{2.45}$$

with $x = 1.61 m^{1/18} k/k_{Jeq}$ and k_{Jeq} is the Jeans scale at matter-ratiation equality. WDM with a mass

$$m_{WDM} = 0.84 \left(\frac{m}{10^{-22}\ \mathrm{eV}} \right)^{0.39}\ \mathrm{keV} \tag{2.46}$$

produces a cut-off with the same half-mode $k_{1/2}$, defined by $T(k_{1/2}) = 0.5$ [98].

Inserting a value for $\bar{\rho}$ that is characteristic for centers of dark matter halos in equation (2.43) gives a rough estimate for the radius below which the density profile must be flattened [93]. In 2014, cored density profiles were confirmed for the first time in 3D cosmological simulations integrating the Schrödinger-Poisson system [1]. The simulations show that FDM behaves like CDM on large scales. On smaller scales, comparable to the local de Broglie wavelength, however, the density fields of collapsed objects like halos and filaments show wave-like patterns. In particular, while the overall shape of halos is still described by an NFW profile, their small scale structure looks 'granular'. Since radial profiles average over cocentric shells, they only show the central granule in the form of a flattened core while the outer parts look similar to the NFW profile. The cores are well described by solitonic solutions to the Schrödinger-Poisson system. Figure 2.1 shows a snapshot of the simulations.

The term 'soliton' refers to ground state solutions of the Schrödinger-Poisson system. For a given total mass they are the configurations with lowest energy. In the Madelung picture, the quantum pressure exactly balances the gravitational pull, similar to a gas cloud in hydrostatic equilibrium. Solitons fulfill the virial condition (equation (2.24)), where the kinetic energy of the scalar field is given by

$$K = \int \frac{\hbar^2}{2a^5 m} |\nabla\Psi|^2 \mathrm{d}^3\mathbf{x} \tag{2.47}$$

and the potential energy by

$$W = \frac{1}{2} \int V a^{-3} m |\Psi|^2 \mathrm{d}\mathbf{x}^3 \tag{2.48}$$

The radial profile of a soliton is approximated by the analytical expression [1]

$$\rho_s(r) \approx \frac{1.9(m/10^{-23}\mathrm{eV})^{-2}(r_c/\mathrm{kpc})^{-4}}{[1 + 9.1 \times 10^{-2}(r/r_c)^2]^8}\ \mathrm{M}_\odot\mathrm{pc}^{-3} \tag{2.49}$$

For a given scalar field mass m the profile is specified by a single free parameter, here expressed as the radius r_c at which the density has dropped to one half of its maximum value in the center. It is related to the mass it encloses according to [1]

$$M_c \approx \frac{5.5 \times 10^9}{(m/10^{-23}\mathrm{eV})^2 (r_c/\mathrm{kpc})}\ \mathrm{M}_\odot \tag{2.50}$$

Spherically symmetric perturbations lead to pulsating oscillations of the density distribution with a frequency [99]

$$f = 10.94 \left(\frac{\rho_c}{10^9\,\mathrm{M}_\odot \mathrm{kpc}^{-3}} \right)^{1/2} \mathrm{Gyr}^{-1}\,, \tag{2.51}$$

where ρ_c is the central density of the soliton in its ground state.

In their cosmological simulations, Schive et al. [100] empirically found a relation between core mass M_c and the virial mass of its host halo M_h

$$M_c = \frac{1}{4} a^{-1/2} \left(\frac{\zeta(z)}{\zeta(0)} \right)^{1/6} \left(\frac{M_h}{M_0} \right)^{1/3} M_0 \tag{2.52}$$

with $M_0 = 4.4 \times 10^7 (m/10^{-22}\mathrm{eV})^{-3/2} M_\odot$ and ζ given by equation (2.25).

2.4.1 Observational constraints

Under the assumption that dark matter is completely made up of FDM, the ΛCDM model is augmented by a single additional free parameter, the scalar field mass m. This parameter has become increasingly constrained by observations casting doubt on the existence of a value small enough to be relevant for the small scale problems of ΛCDM.

The dark matter only simulations in [1] make a generic prediction for density profiles of FDM halos. Solitonic cores with a mass given by equation (2.52) are embedded in NFW profiles. This prediction can be fit to stellar kinematics data of dwarf spheroidals (dSph) which, as discussed in section 2.2.2, might have cored dark matter profiles. The inferred masses are $0.81^{+0.16}_{-0.17} \times 10^{-22}$ eV [1], $m = 1.18^{+0.28}_{-0.24} \times 10^{-22}$ eV [101], $m = 3.7 - 5.6 \times 10^{-22}$ eV [102], $m < 1.1 \times 10^{-22}$ eV [103], $m < 0.4 \times 10^{-22}$ eV [104], $0.8 - 1.2 \times 10^{-22}$ eV [105]. Using only the mass versus half-light radius relation, [106] pointed out, that it is impossible to fit all Milky Way satellites with a single mass m. In [107], the soliton+NFW profile was fitted to rotation curves of bright dwarf galaxies with rotating disks, for which cored profiles are more established. The analysis yielded an even lower mass of $m = 0.554 \times 10^{-23}$ eV. [108; 109] also found rotation curve measurements to be incompatible with masses in the usual range for FDM ($m = 10^{-22} - 10^{-21}$ eV). [110] pointed out a general problem of the FDM explanation to the cusp-core problem in bright dwarf galaxies: The core-halo mass relation (equation (2.52)) predicts the core radius to scale inversely with virial velocity of a halo, but rotation curve measurements suggest that the core radius increases with increasing velocity.

Like in the case of WDM, strong constraints on the minimal allowed field mass are imposed by Lyman-α forest measurements. This is because the method probes scales near to the linear power spectrum cut-off at redshifts where they are still only slightly non-linear. The term "Lyman-α forest" refers to hydrogen absorption line features in highly redshifted quasar spectra, tracing the distribution of neutral hydrogen and, in a biased manner, the underlying dark matter distribution. Because of the non-linear evolution involved, the analysis typically requires hydrodynamical cosmological simulations to predict flux power spectra from a given linear transfer function. [111] found a lower mass of 20×10^{-22} eV using quasars with redshift $z = 3.5 - 5.4$. Using data from SDSS, [112] constrained the field mass to be larger than 23×10^{-22} eV. These values are in strong tension with the ones obtained from stellar kinematics in dwarf spheroidals. However, interpretations of Lyman-α forest observations, especially at high redshifts, are arguably not entirely trustworthy because the effect of inhomogeneous reionization is difficult to account for in the modelling of flux spectra [113]. Furthermore, the hydrodynamical simulations in [18] and [112] employed standard N-body methods instead of solving the Schrödinger-Poisson system. Thus, the small scale effects of FDM relative to CDM in the non-linear evolution was not covered.

In the ΛCDM model small perturbations collapse first [25]. Consequently, the suppression of linear small scale power in FDM can significantly delay the formation of the first galaxies. Early time galaxy formation can be probed in a number of ways. Using abundance matching together with the halo mass function inferred from analytical methods [114] or cosmological simulations [115; 116; 117] the luminosity function (number of galaxies with UV magnitude below a certain value) of FDM can be constructed. The luminosity function can be directly compared to the observed UV luminosity function as derived from high redshift observations of galaxies with the Hubble space telescope up to a redshift of $z = 10$ [118]. Alternatively, the luminosity function can be used to predict the reionization history of the universe as the first galaxies, among quasars, are considered its primary cause. The reionization history is probed by hydrogen absorption in quasar spectra [119] (Gunn-Peterson trough) or by Thomson scattering of CMB photons with free electrons [24]. The inferred lower bounds for the FDM mass m are lower than the Lyman-α forest constraints. They are slightly higher than 10^{-22} eV [114; 115; 117] or even lower than that [116] depending on the specific model and data analyzed. Recently, the EDGES experiment found an absorption feature in the sky-averaged CMB spectrum which corresponds to the 21 cm line (hyperfinestructure of neutral hydrogen) redshifted to $z \sim 15 - 20$ [120]. This is interpreted as a signature of star formation at that redshift, because the spin temperature of neutral hydrogen would otherwise equilibrate with the CMB, leading to the absence of net absorption or emission. Since FDM delays star formation, this imposes a constraint of $m \geq 5 \times 10^{-21}$ eV [121].

Turning away from the high redshifts, a number of implications of the specific behaviour of FDM on de Broglie scales were proposed in [113]. These include interactions between the granular density structure of FDM halos with the stellar component leading to the disruption of star clusters or, generally, to a heating of the stellar component, which was further investigated in [122]. This lead to constraints of $m \geq 0.6 \times 10^{-22}$ eV from the thickness of the galactic disks [123] and $m \geq 1.5 \times 10^{-22}$ eV from the heating of stellar streams [124]. From the stability of a central star cluster in the ultrafaint dwarf Eridanus II, [125] derived a lower bound of $m \geq 10^{-19}$ eV but with a mass window $10^{-21} \gtrsim m \gtrsim 10^{-20}$

that could not be unambiguously excluded with the employed approximations. Subhalos in the FDM model react differently to tidal forces exerted by the host halo, because of quantum pressure effects [113]. From the survival of Milky Way satellites despite tidal forces, [126] derived a bound of $m \gtrsim 2 \times 10^{-21}$ eV.

To summarize, it is unlikely that FDM density profiles found in the simulations in [100] can solve the cusp-core problem for all dwarf galaxy masses. What is worse, FDM with a relevant scalar field mass is even disfavoured by some observations. Fits to kinematic data of dwarf galaxies seem to favour different field masses m depending on the galaxy mass. Apparently, there is a trend towards smaller field masses m the more massive a galaxy is. Constraints from the Lyman-α forest and others exclude the masses necessary to explain density distribution of bright and intermediate dwarf galaxies.

Note that so far fits of dwarf galaxies profiles are all based on simulations that do not take the effect of gas and stars on the halo structure into account. This approximation might be reasonable because dwarf galaxies are strongly dark matter dominated. However, a critical examination is necessary and will be provided in chapter 5.

All the constraints listed above are modified if FDM is considered to be only a fraction of the total dark matter density. These mixed dark matter models are considered in various published works.

2.4.2 Theoretical description of FDM dynamics

For the lack of laboratory experiments, progress in the theory of cosmological structure formation is often made by a combination of numerical simulations and analytical models. While simulations allow us to see the grand picture, analytical descriptions isolate and give an understanding of individual mechanisms at work, which can then be generalized to situations that cannot be probed by simulations, because of limited computational resources for example. The same is true for FDM theory. For instance, the similarity of FDM and CDM on large scales has become known as Schrödinger-Vlasov correspondence. More or less heuristically, it can be understood in terms of the Ehrenfest theorem: A localized wave packet in an external potential moves according to the classical trajectory of a single particle. A general wavefunction can be decomposed into a collection of localized wave packets. Thus, since the Schrödinger equation with external potential is linear, the collection of wave packets behaves like a collection of classical particles.

There are two factors that the above discussion fails to take into account: First, the gravitational potential of FDM is actually not external, but instead sourced by the FDM density itself. This makes the Schrödinger equation non-linear. Secondly, under time evolution, wave packets do not stay localized. Free wave packets disperse gradually with time and interactions with the gravitational potential can potentially disrupt them completely (tunnel effect). To quantify the deviations from CDM, the Schrödinger-Vlasov correspondence can be described in terms of phase space densities. The Wigner distribution of a Schrödinger wavefunction is given by

$$f_W(\mathbf{x},\mathbf{p}) = \int \frac{\mathrm{d}^3\tilde{\mathbf{x}}}{(\pi\hbar)^3} \exp\left[2\frac{i}{\hbar}\mathbf{p}\cdot\tilde{\mathbf{x}}\right] \Psi(\mathbf{x}-\tilde{\mathbf{x}})\Psi^*(\mathbf{x}+\tilde{\mathbf{x}}) \tag{2.53}$$

It can be thought of as an equivalent to the phase space density of a classical ensemble of particles like in the Vlasov equation (equation (2.26)). However, unlike the Vlasov phase space density, it allows for negative values and often has strong oscillatory behaviour on small scales in position and momentum space [127]. Coarse-graining the Wigner distribution with a Gaussian filter

$$\bar{f}_W \sim \int \exp\left(-\frac{1}{2\sigma_x^2}(\Delta x)^2 - \frac{1}{2\sigma_p^2}(\Delta p)^2\right) f_W \tag{2.54}$$

with $\sigma_x\sigma_p \geq \hbar/2$ makes the Wigner distribution strictly positive. Using the Schrödinger equation, the evolution equation for $\bar{f}_W$ can be derived showing that it agrees with the Vlasov equation coarse-grained in the same way as f_W, if $\sigma_x\sigma_p \geq \hbar/2$ [127].

The special case of $\sigma_x = \sigma_p = \sqrt{\hbar/2}$ is the so-called Husimi representation

$$f_H = |\Psi_H(\mathbf{x},\mathbf{p})|^2 \tag{2.55}$$

with

$$\Psi_H(\mathbf{x},\mathbf{p}) = \left(\frac{1}{2\pi\hbar}\right)^{3/2} \left(\frac{1}{2\pi\sigma_x^2}\right)^{3/4} \int \mathrm{d}^3\tilde{\mathbf{x}} \exp\left[-\frac{(\mathbf{x}-\tilde{\mathbf{x}})^2}{4\sigma_x^2} - \frac{i}{\hbar}\mathbf{p}\cdot\left(\tilde{\mathbf{x}}-\frac{1}{2}\mathbf{x}\right)\right] \Psi(\tilde{\mathbf{x}}) \tag{2.56}$$

In this expression, a decomposition into localized Gaussian wave packets, like in the heuristic discussion above, is explicitly visible.

During the linear regime of cosmological structure formation, the points in 6D phase space with non-zero density approximately form a 3D hyperplane. The velocity distribution of CDM at a given point in space is single-valued and, thus, can be described by the pressure-less fluid description (equations (2.6) to (2.8)). At this time, the phase space distribution is easily translated to a Schrödinger wavefunction by reverting the substitution in equation (2.37) for the Madelung transformation [128]. After shell-crossing, the fluid description of CDM breaks down as the velocity distribution of CDM becomes multi-valued. Due to the Schrödinger-Vlasov correspondence the Husimi distribution for FDM starting from the same

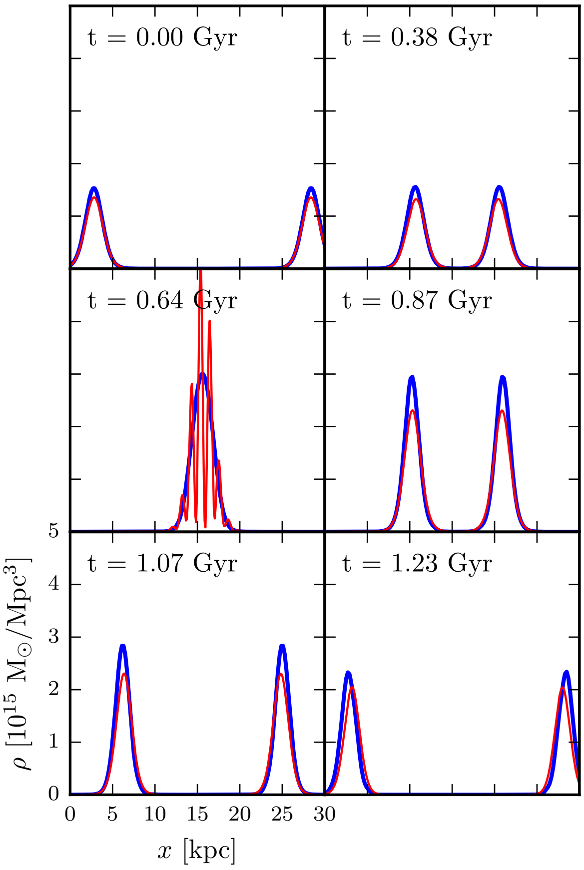

Figure 2.2: This figure illustrates the different behaviours of particles (blue) and Schrödinger field (red) when the velocity distribution is multi-valued. At the time of collision, the kinetic energy is stored in the velocity dispersion of particles in one case and in the interference pattern in the other case.
© 2016 American Physical Society [2]

initial conditions does the same. However, the underlying Schrödinger wavefunction or the equivalent Madelung equations with a single velocity at a given point always remain valid. For FDM, having multiple velocities in the Husimi representation corresponds to the formation of interference patterns in the density field. This can be most easily seen in simulations of idealized set-ups like the interference of two solitons shown in figure 2.2. In virialized dark matter halos, one expects many different velocity vectors at any given point. Their interference explains the granular structure observed in FDM halos. Indeed, a similar pattern can be produced by superimposing an isotropic distribution of plane waves with random phases like in equation (2.57) of the next paragraph.

A specific effect, which is potentially able to cause super de Broglie scale deviations between CDM and FDM and thereby spoiling the Schödinger-Vlasov correspondence is relaxation by gravitational interaction between the granules within dark matter halos. It is possible because of the non-linear nature of the Schrödinger-Poisson system. The phenomenon was numerically studied in [129]. A simulation was initiated with a wavefunction given in Fourier space as

$$\tilde{\Psi}(\mathbf{k}) = N \exp(-|\mathbf{k}|) \exp(i\varphi_{\mathbf{k}}) \tag{2.57}$$

where N is a prefactor factor related to the average density of the field and $\varphi_{\mathbf{k}}$ is a random phase for each Fourier mode. If N is sufficiently small, the contribution of the gravitational potential energy to the energy of Fourier mode can be neglected. In this case, each $\mathbf{k}$ can be associated to an energy ω according to $\omega \sim \mathbf{k}^2$. Thus, the energy distribution of mass ($|\Psi|^2$) in the initial state is

$$\begin{aligned} F(\mathbf{k})\mathrm{d}\mathbf{k} &\sim \exp(-\mathbf{k}^2)\mathrm{d}\mathbf{k} \sim k^2 \exp(-k^2)\mathrm{d}k \\ &\sim \omega \exp(-\omega)\frac{\mathrm{d}k}{\mathrm{d}\omega}\mathrm{d}\omega \sim \omega^{1/2} \exp(-\omega)\mathrm{d}\omega \sim F(\omega)\mathrm{d}\omega \end{aligned} \tag{2.58}$$

Thermalization of a classical field leads to equipartition of energy among its degrees of freedom, which are the Fourier modes in this case. Then, the energy distribution is given by

$$F(\mathbf{k})\mathrm{d}\mathbf{k} \sim \frac{1}{\mathbf{k}^2}\mathrm{d}\mathbf{k} \sim \frac{k^2}{k^2}\mathrm{d}k \sim \frac{\mathrm{d}k}{\mathrm{d}\omega}\mathrm{d}\omega \sim \omega^{-1/2}\mathrm{d}\omega \sim F(\omega)\mathrm{d}\omega \tag{2.59}$$

Exactly this shift from the spectrum in equation (2.58) to the one in equation (2.59) was observed in the simulations in [129]. Moreover, the formation of a soliton at a random point in the simulation box was observed. Over time, the soliton accumulates mass. This phenomenon was interpreted as Bose-Einstein condensation, because a soliton is the lowest energy state of the Schödinger-Poisson system.

The spectrum shift, the formation of the soliton and its growth all happen on a single timescale τ_{gr}. In [129], this timescale was derived via the Landau scattering intergral, which describes wave interaction by long range forces. More heuristically, but leading to the same result, the relaxation time can be derived by treating the granules as quasi-particles and considering two body relaxation between them [113]. Accordingly, the relaxation time in a halo consisting of N particles is given by [130]

$$\tau_{gr} \approx 0.1 \left(\frac{N}{\log \Lambda} \right) t_{cr} \tag{2.60}$$

where $\log \Lambda$ is the Coulomb logarithm and t_{cr} the crossing time. The size of the quasi-particles is determined by the de Broglie wavelength corresponding to the virial velocity v of the halo $l_{granule} \approx 0.5\lambda_{dB} = \pi\hbar/mv$. Thus, taking the quasi-particle number in terms of the halo radius R to be $N \approx (R/l_{granule})^3$ and using that $t_{cr} = R/v$ gives

$$\tau_{gr} \approx 0.1 \left(\frac{Rmv}{\hbar\pi} \right)^3 \left(\frac{R}{v} \right) (\log \Lambda)^{-1} \tag{2.61}$$

Plugging in realistic physical quantities gives [113]

$$\tau_{gr} \sim \frac{10^{10}\text{yr}}{f_{relax}} \left(\frac{v}{100\text{km s}^{-1}} \right)^2 \left(\frac{R}{5\text{kpc}} \right)^4 \left(\frac{m}{10^{-22}\text{eV}} \right)^3 \tag{2.62}$$

Here, the Coulomb logarithm $\log \Lambda \approx \log(R/l_{granule})$ was absorbed into the dimensionless constant $f_{relax} \lesssim 1$, which also accounts for other approximations in the derivation.

2.4.3 Candidates from particle physics

FDM requires a spin-zero field Φ with a very low mass. Such fields naturally occur in extensions to the standard model of particle physics, where Φ is an angular variable, so that the potential $V(\Phi)$ is periodic with $V(\Phi + 2\pi) = V(\Phi)$. The potential can be induced by non-perturbative quantum effects which often implies low masses m with $V(\Phi) = \frac{m^2c^2}{\hbar^2}\Phi^2 + \mathcal{O}(\Phi^4)$ [113].

One example is the Axion, a particle proposed to solve the CP-problem of Quantum Chromodynamics by Peccei and Quinn [131]. QCD allows for a CP violating term in its Lagrangian

$$\mathcal{L}_{\theta QCD} = \frac{\theta_{QCD}}{32\pi^2} \epsilon^{\mu\nu\lambda\rho} \text{Tr} G_{\mu\nu} G_{\lambda\rho} \tag{2.63}$$

where $G_{\mu\nu}$ is the gluon field strengh tensor. The term leads to a neutron electric dipole moment, which is experimentally constrained, implying $\theta_{QCD} \lesssim 10^{-10}$ [132]. This is a fine tuning problem since θ_{QCD} gets a $\mathcal{O}(1)$ contribution from the chiral anomaly in the presence of fermions

$$\theta_{QCD} = \bar{\theta}_{QCD} + \arg\, \det M_u M_d \tag{2.64}$$

where M_u and M_d are the quark matrices. Thus, the free parameter $\bar{\theta}_{QCD}$ has to be tuned to cancel the second term.

In the axion solution to this problem, θ_{QCD} is the angular component of an additional complex scalar field $\varphi = |\varphi| e^{i\theta_{QCD}}$. The total Lagrangian obeys a global U(1) symmetry acting as a shift on θ_{QCD}. Similar to the Higgs field, the complex field has a symmetry breaking potential

$$V(\varphi) = \lambda \left(|\varphi|^2 - \frac{f_a^2}{2} \right)^2 \tag{2.65}$$

Thus, at an energy scale f_a the global U(1) symmetry is spontaneously broken and $\Phi = \theta_{QCD} f_a$, which is now called the "axion" emerges as a Nambu-Goldstone boson. Depending on the concrete model the axion is coupled to $\epsilon^{\mu\nu\lambda\rho} G_{\mu\nu} G_{\lambda\rho}$ in one way or another. Non-perturbative effects of QCD (instantons) then give the axion a potential which drives the CP-violating term to zero.

Directly after spontaneously breaking the U(1) symmetry, the axion does not have a preferred value. Instead, θ_{QCD} takes a random value between $-\pi$ and π. When non-perturbative effects switch on, this results in a residual excitation of the axion field. This so-called "misalignment production" is the primary mechanism, by which a cosmological population of axions, which potentially makes up the dark matter is produced. Since initially the axion field has a value $\Phi_i = \theta_i f_a \sim f_a$ and the energy density is given by $\rho \sim m^2 |\Phi|^2$, the resulting dark matter fraction is strongly influenced by the two parameters m and f_a. In the case of the QCD-axion, the two parameters are related [133]

$$m \approx 6 \times 10^{-10} \mathrm{eV} \left(\frac{10^{16} \mathrm{GeV}}{f_a} \right) \tag{2.66}$$

For this reason, the mass m is the main parameter, which determines the axion relic-density. Masses below $m \sim 10^{-6}$ eV can be excluded because they would produce too much dark matter [134]. Thus, although axions in general are a candidate for dark matter (CDM in this case) and they are rather light particles, they do not allow the ultralight masses needed in the FDM model.

However, particles with similar properties as the axion arise generically, if the standard model is derived from string theory [113; 133]. They appear in compactifications of extra space-time dimensions as Kaluza-Klein zero modes of antisymmetric tensor fields. In these models, the constant of proportionality in equation (2.66) can assume a large range of values [113]. This allows for an axion-like particle with $m \approx 10^{-22}$ eV making up the dark matter content of the universe, like in the FDM model. In order to produce enough dark matter by misalignment, f_a must be of the order $f_a \sim 10^{16}$ GeV, which means that Φ takes its initial value before inflation. Inflation then homogenizes the field. After the end of inflation, the axion-like field falls into the potential wells that the inflaton fluctuations have generated. This defines the initial spectrum of adiabatic perturbations of the dark matter field [98].

While string theory explains why an ultralight scalar with $m \approx 10^{-22}$ eV can exist, it does not motivate why the mass has the specific value. In fact, most models predict the existence of several axion-like particles with a homogeneous distribution of masses on a logarithmic scale [133]. If any of those additional ALPs has a mass in the range 0.4 GeV $\gtrsim m \gtrsim 10^{22}$ eV, they pose a potential problem to cosmology as they would predict to much dark matter [113]. It therefore has to be stressed that, although string theory can produce FDM, the main motivation for the ultralight mass stems from its astrophysical implications. Another line of reasoning is also possible: String theory motivates the hypothesis that dark matter is given by a light scalar field with negligible self-interaction. Studying the implications on cosmological structure formation can potentially constrain the mass range around $m \sim 10^{-22}$ eV.

2.4.4 Quantum or classical?

Despite the mentioning of "particles" in the last section, the dynamics of FDM can be entirely understood in terms of classical field theory. This can be seen in the governing Schrödinger equation (equation (2.34)), where the fundamental constant of quantum mechanics only shows up in the combination $\hbar/m$. It serves as a definition of the mass m, which itself does not show up alone. $\hbar$ and m would acquire a meaning if the field Ψ was treated in the framework of quantum field theory, but that is not the case in the FDM model. In the FDM literature, this is often justified with a "high occupancy number" [93]. Indeed, it might seem absurd to talk about quantum effects on cosmological length scales. However, in the FDM model, the de Broglie wavelength, a quantum mechanical quantity, is explicitly stretched to those scales. Based on quantum mechanical calculations, several authors claim that quantum effects in FDM are significant and, as a consequence, the classical field description is invalid [135; 136; 137].

Although eventually every classical theory must be derivable from the more fundamental quantum theory, classical field descriptions are perfectly valid in various fields of physics. Laser light, for example, can be well described by classical electromagnetic field equations. Bose-Einstein condensates produce macroscopical wave functions, which can be understood as classical fields. In fact, quantum field theory admits quantum states with properties very close to those of classical fields. They are called coherent states and the two phenomena mentioned above can be described by those states [138; 139].

Coherent states play an important role in theories of spontaneous symmetry breaking. In the case of the axion, the global U(1) symmetry is broken when φ in equation (2.65) obtains a non-zero expectation value for the field operator $\langle\hat{\varphi}\rangle = |\varphi|e^{i\theta_{QCD}}$. This is impossible if the quantum state of the axion field is an eigenstate of the particle number operator, as those would always give $\langle\hat{\varphi}\rangle = 0$. In contrast, coherent states allow for a non-zero expectation value. Because the misalignment population of axions is nothing but the symmetry breaking field θ_{QCD}, it is already produced in a coherent state or at least close to one [140]. The same fact is often referred to as axions forming a "condensate" [113].

Coherent states were already discovered in the early days of quantum mechanics by Erwin Schrödinger for the quantum mechanical harmonic oscillator [141]. Here, coherent states are states with minimum uncertainty $\Delta x \Delta p = \hbar/2$ with the expectation values of $\hat{x}(t)$ and $\hat{p}(t)$ exactly given by the classical trajectory of a single particle. Since in a free scalar field, the Fourier modes can be thought of as independent harmonic oscillators, the concept can be easily generalized to such fields. For brevity, the discussion below copes with real scalar fields, like the axion field, instead complex ones. A coherent state can then be written in terms of the creation operator $\hat{a}_k^\dagger$ and the Fourier transform of the classical field $\tilde{\Phi}$ as [140]

$$|\Phi\rangle = \frac{1}{N} \exp\left[\int \frac{\mathrm{d}^3\mathbf{k}}{(2\pi)^3} \sqrt{\frac{E_k}{2}} \tilde{\Phi}(\mathbf{k}) \hat{a}_k^\dagger\right] |0\rangle \tag{2.67}$$

where N is a normalization factor, so that $\langle\Phi|\Phi\rangle = 1$. As can be seen in this notation, the coherent state is a superposition of an infinite number of particle number eigenstates. Note, that the classical field can always be decomposed into $\tilde{\Phi} = \tilde{\Phi}_1 + \tilde{\Phi}_2$ and the state can then be written with a subsequent application of the operator above.

$$|\Phi\rangle = \frac{1}{N} \exp\left[\int \frac{\mathrm{d}^3\mathbf{k}}{(2\pi)^3} \sqrt{\frac{E_k}{2}} \tilde{\Phi}_1(\mathbf{k}) \hat{a}_k^\dagger\right] \exp\left[\int \frac{\mathrm{d}^3\mathbf{k}}{(2\pi)^3} \sqrt{\frac{E_k}{2}} \tilde{\Phi}_2(\mathbf{k}) \hat{a}_k^\dagger\right] |0\rangle \tag{2.68}$$

Thus, coherent states do not have any notion of particles being in certain 1-particle states. In summary, coherent states can be thought of being the most "field-like" and the least "particle-like" states in the Hilbert space of a quantum field.

Using the commutation relation $[\hat{a}_k, \hat{a}_p^\dagger] = \delta^3(k-p)(2\pi)^3$, the computation of expectation value of the field operator gives the classical field $\Phi(\mathbf{x})$

$$\begin{aligned}\langle\Phi|\hat{\Phi}(\mathbf{x})|\Phi\rangle &= \langle\Phi|\int \frac{\mathrm{d}^3\mathbf{k}}{(2\pi)^3}\frac{1}{\sqrt{2E_k}}\left(\hat{a}_k e^{-i\mathbf{k}\cdot\mathbf{x}} + \hat{a}_k^\dagger e^{i\mathbf{k}\cdot\mathbf{x}}\right)|\Phi\rangle \\ &= \int \frac{\mathrm{d}^3\mathbf{k}}{(2\pi)^3}\frac{1}{2}\left(\tilde{\Phi}(\mathbf{k})e^{-i\mathbf{k}\cdot\mathbf{x}} + \tilde{\Phi}^*(\mathbf{k})e^{i\mathbf{k}\cdot\mathbf{x}}\right) = \mathrm{Re}\ \Phi(\mathbf{x}) = \Phi(\mathbf{x}) \qquad (2.69)\end{aligned}$$

The time evolution of the coherent state is given by the classical evolution of the field $\Phi(\mathbf{x}, t)$

$$\begin{aligned}e^{-i\hat{H}t}|\Phi\rangle &= \frac{1}{N}\exp\left[\int \frac{\mathrm{d}^3\mathbf{k}}{(2\pi)^3}\sqrt{\frac{E_k}{2}}\tilde{\Phi}(\mathbf{k})\left(e^{-i\hat{H}t}\hat{a}_k^\dagger e^{i\hat{H}t}\right)\right]|0\rangle \\ &= \frac{1}{N}\exp\left[\int \frac{\mathrm{d}^3\mathbf{k}}{(2\pi)^3}\sqrt{\frac{E_k}{2}}\tilde{\Phi}(\mathbf{k})e^{-iE_k t/\hbar}\hat{a}_k^\dagger\right]|0\rangle \\ &= \frac{1}{N}\exp\left[\int \frac{\mathrm{d}^3\mathbf{k}}{(2\pi)^3}\sqrt{\frac{E_k}{2}}\tilde{\Phi}(\mathbf{k}, t)\hat{a}_k^\dagger\right]|0\rangle \\ &= |\Phi_t\rangle \qquad (2.70)\end{aligned}$$

To estimate the significance of quantum fluctuations, the variance of the field operator convoluted with a localized smooth function $F(x)$ can be computed ($\hat{\Phi}(F) = \int \mathrm{d}^3\mathbf{x}F(x)\hat{\Phi}(\mathbf{x})$)

$$\begin{aligned}\langle\Phi|\hat{\Phi}(F)^2|\Phi\rangle =&\langle\Phi|\int \mathrm{d}^3\mathbf{x}F(x)\int \mathrm{d}^3\mathbf{x}'F(x')\int\frac{\mathrm{d}^3\mathbf{k}}{(2\pi)^3}\int\frac{\mathrm{d}^3\mathbf{p}}{(2\pi)^3}\frac{1}{\sqrt{2E_k}}\frac{1}{\sqrt{2E_p}} \\ &\hat{a}_k e^{-i\mathbf{k}\cdot\mathbf{x}}\hat{a}_p e^{-i\mathbf{p}\cdot\mathbf{x}'} + \hat{a}_k^\dagger e^{i\mathbf{k}\cdot\mathbf{x}}\hat{a}_p e^{-i\mathbf{p}\cdot\mathbf{x}'} + \hat{a}_k^\dagger e^{i\mathbf{k}\cdot\mathbf{x}}\hat{a}_p^\dagger e^{i\mathbf{p}\cdot\mathbf{x}'} \\ &+ \hat{a}_p^\dagger e^{i\mathbf{p}\cdot\mathbf{x}'}\hat{a}_k e^{-i\mathbf{k}\cdot\mathbf{x}} + \delta^3(k-p)(2\pi)^3 e^{-i\mathbf{k}\cdot\mathbf{x}}e^{i\mathbf{p}\cdot\mathbf{x}'}|\Phi\rangle \\ &= \left(\int \mathrm{d}^3\mathbf{x}F(x)\Phi(\mathbf{x})\right)^2 + \int\frac{\mathrm{d}^3\mathbf{k}}{(2\pi)^3}\frac{1}{2E_k}\tilde{F}(k)^2 \\ &= \left(\int \mathrm{d}^3\mathbf{x}F(x)\Phi(\mathbf{x})\right)^2 + const. \qquad (2.71)\end{aligned}$$

The relative quantum mechanical uncertainty of the convoluted field operator is thus given by

$$\frac{\sqrt{\langle\hat{\Phi}(F)^2\rangle - \left(\langle\hat{\Phi}(F)\rangle\right)^2}}{\Phi(F)} \sim \frac{1}{\Phi(F)} \tag{2.72}$$

This shows that, since for axion dark matter $\Phi(F)$ is sufficiently high, quantum fluctuations can be neglected as long as the axions are in a coherent state [142].

Returning to the question of whether the classical treatment of the axion field is valid, the above discussion favours a positive answer. In fact, some of the papers criticizing the classical treatment do not assume the axion field to be in a coherent state, but instead in a state with a sharp particle number [135; 136]. One might object that, in the above discussion of coherent states interactions between field modes via gravity were not taken into account. Indeed, in [143], it was shown in a simplified model of coupled quantum mechanical harmonic oscillators that the expectation values for the occupation numbers (corresponding to $\langle\hat{a}_k\hat{a}_k^\dagger\rangle$ in the notation above) still start to differ from their classical analogues on short timescales. This might be due to the highly chaotic nature of the problem studied, where classical treatments are known to break down very quickly [144]. As a final remark, it is questionable if the comparison between the quantum mechanical expectation value $\langle\hat{a}_k\hat{a}_k^\dagger\rangle$ and the classical density is meaningful at all. The cosmic dark matter field is not a closed system, but instead, via its gravitational interaction coupled to everything else in the universe including ourselves. Human observers will always experience the wavefunction of the axion field in a "collapsed" state.

Chapter 3

Numerical methods

This chapter describes the numerical methods employed in chapters 4 and 5. In both projects, a modified version of the public cosmology code Enzo [145] was used. Enzo combines a particle-mesh algorithm for dark matter with grid-based solvers for hydrodynamics or magnetohydrodynamics on an expanding cosmological background. It furthermore provides modules for radiative heating and cooling, star formation and feedback and radiation transport. It supports parallel computation with distributed memory using the Message Passing Interface (MPI) and allows for adaptive mesh refinement, meaning that in some regions of the simulation box fulfilling user-defined criteria the spatial resolution is increased compared to the root-grid resolution. To solve the equations of motion of FDM, the author of this thesis took part in the development of a new hybrid method using both particle-based and grid-based algorithms and its implementation into Enzo together with his collaborators Bodo Schwabe and Jens Niemeyer. It was first published in the article corresponding to chapter 4 [3]. The hybrid method is described in section 3.1.4 after giving an overview of existing algorithms for FDM in the preceding subsections. Other physics modules of Enzo used in chapters 4 and 5 and the generation of initial conditions are discussed in section 3.2.

Figure 3.1 shows the result of a scaling test conducted on the computer cluster of the North-German Supercomputing Alliance (HLRN). The code version and the test problem are the same as in chapter 4. Using 384 processor cores, like in most of the runs in chapters 4 and 5, leads to a speed-up by a factor of 20.5 compared to using only 4. Thus, the strong scaling efficiency is 21.3 % compared to linear scaling.

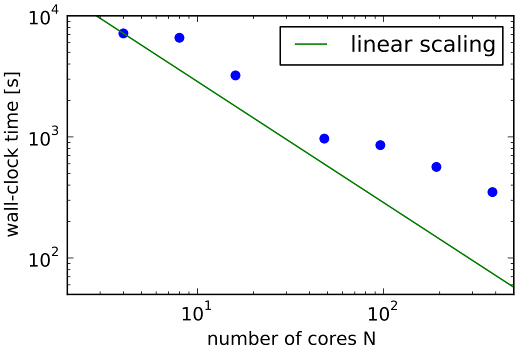

Figure 3.1: Elapsed real time during a complete root grid time step involving many time steps on finer resolution levels vs. number of employed processor cores.

3.1 Simulating fuzzy dark matter

3.1.1 An explicit and stable solver for the Schrödinger equation

The numerical solver for the Schrödinger equation presented here is based on the so-called ”method of lines” [146]. This means, as a first step, the spatial coordinates of the wavefunction are discretized transforming the partial differential equation into an ordinary differential equation. This ODE can then be integrated with an appropriate method with respect to the remaining parameter t. For better readability, the spatial discretization is written out in one dimension here:

$$\Psi_j(t) = \Psi(j * \Delta x, t) \tag{3.1}$$

with a constant spatial separation Δx. The second derivative in the Schödinger equation is replaced with the discretized expression

$$\nabla^2 \Psi_j = \frac{\Psi_{j-1} - 2\Psi_j + \Psi_{j+1}}{(\Delta x)^2} \tag{3.2}$$

which is second-order accurate in Δx, yielding

$$i\hbar \frac{\partial \Psi_j}{\partial t} = -\frac{\hbar^2}{2ma^2(\Delta x)^2}(\Psi_{j-1} - 2\Psi_j + \Psi_{j+1}) + V_j m \Psi_j \tag{3.3}$$

This is now a set of coupled ordinary differential equations. It can be written with a matrix $\mathcal{A}$ as

$$\frac{\partial \Psi_j}{\partial t} = \mathcal{A}\Psi_j \tag{3.4}$$

In principle, an arbitrary integration scheme with desired accuracy in terms of the timestep Δt can now be chosen. However, because the Schrödinger equation is a "stiff" equation, special care has to be taken regarding the stability of the employed method. While the concept of "accuracy" measures the numerical error induced in a single timestep, "stability" describes the long-term effect on the numerical solution induced by small errors in the initial conditions. A specific criterion for stability is to require the numerical solution to be bounded when the exact solution is bounded [146]. Assuming that $\mathcal{A}$ is constant, the exact solution to equation (3.4) after n timesteps of the length Δt is

$$\Psi_j(n\Delta t) = \exp(n\Delta t\mathcal{A})\Psi_j(0) \tag{3.5}$$

Because $\mathcal{A}$ is symmetric, it can be diagonalized. Thus, changing the basis of Ψ_j the equation can be written in terms of the eigenvalues λ_j of $\mathcal{A}$

$$\tilde{\Psi}_j(n\Delta t) = \exp(n\Delta t\lambda_j)\tilde{\Psi}_j(0) \tag{3.6}$$

Since $\mathcal{A}$, on top of being symmetric, has only imaginary entries, its eigenvalues are also imaginary. Thus,

$$|\exp(n(\Delta t)\lambda_j)| = 1 \tag{3.7}$$

which is just an expression of the unitary nature of the Schrödinger equation. In the context presented here, it means that the exact solution is bounded everywhere. For a general time integration scheme the equivalent to equation (3.6) is [146]

$$\tilde{\Psi}_j(n\Delta t) = R^n((\Delta t)\lambda_j)\tilde{\Psi}_j(0) \tag{3.8}$$

Now, if $|R((\Delta t)\lambda_j)| > 1$ for some eigenvalue λ_j, the corresponding eigenvector will grow exponentially, spoiling the boundedness of the solution and accumulating numerical errors. Thus, stability requires $|R(\Delta\lambda_j)| \leq 1$. The third-order Runge-Kutta solver is the lowest-order Runge-Kutta scheme fulfilling this stability criterion for the Schrödinger equation given that Δt is sufficiently small [147]. However, the fourth-order Runge-Kutta integration allows for a larger timestep.

Here, the update from t_0 to $t_0 + \Delta t$ is given by

$$\Psi_j(t_0 + \Delta t) = \Psi_j(t_0) + \Delta t \cdot \frac{1}{6}\left(k_{1j} + 2k_{2j} + 2k_{3j} + k_{4j}\right) \tag{3.9}$$

with

$$k_{1j} = \mathcal{A}\Psi_j(t_0) \tag{3.10}$$

$$k_{2j} = \mathcal{A}(\Psi_j(t_0) + \frac{\Delta t}{2}k_{1j}) \tag{3.11}$$

$$k_{3j} = \mathcal{A}(\Psi_j(t_0) + \frac{\Delta t}{2}k_{2j}) \tag{3.12}$$

$$k_{4j} = \mathcal{A}(\Psi_j(t_0) + \Delta t k_{3j}) \tag{3.13}$$

Using the fact that $\mathcal{A}$ has only imaginary eigenvalues, the stability function R is then [146; 147]

$$|R((\Delta t)\lambda_j)|^2 = 1 + \frac{(\Delta t)^8\lambda_j^8}{576} - \frac{(\Delta t)^6\lambda_j^6}{72} \tag{3.14}$$

It is less or equal to 1 for

$$\Delta t < \frac{\sqrt{8}}{|\lambda_{max}|} \tag{3.15}$$

where λ_{max} is the largest absolute eigenvalue of $\mathcal{A}$. For the Schrödinger equation (equation (3.3)) in three dimensions, it can be computed, giving [147]

$$\Delta t < \frac{\sqrt{8}}{6 - \frac{m^2a^2(\Delta x)^2}{\hbar^2}V_{min}}\frac{m}{\hbar}a^2(\Delta x)^2 \tag{3.16}$$

where V_{min} is the most negative value of the gravitational potential. If the gravitational potential is neglected, the maximum timestep scales with the square of the spatial resolution

$$\Delta t < \frac{\sqrt{2}}{3}\frac{m}{\hbar}a^2(\Delta x)^2 \tag{3.17}$$

This can be interpreted as requiring that the change of the Fourier mode with wavelength $2\Delta x$ (Nyquist frequency) in one timestep must not be too large. Note, that the kinetic operator in the Schrödinger equation scales with the inverse square of the wavelength. Thus, taking for instance a spatial grid of 512^3 cells, the timescale of the Nyquist mode is 256^2 times faster than the largest wave length contained in the grid. This is the common property of ”stiff” differential equations: Stability of certain numerical algorithms requires an extremely small timestep compared to most of the physical timescales involved in the problem.

3.1.2 Alternative grid-based solvers for the Schrödinger equation

Not every numerical algorithm shares the restrictive timestep requirement of the 4th-order Runge-Kutta method. Actually, there are various algorithms for the Schödinger equation, which are unconditionally stable, meaning that there is no upper limit for the timestep to ensure stability. The Crank-Nicholson scheme, for example, is second order accurate in Δt and unitary ($|R((\Delta t)\lambda_j)| = 1$) for all timesteps [148]. It is given by

$$\Psi_j(t_0 + \Delta t) = \Psi_j(t_0) + \Delta t \mathcal{A} \left(\frac{\Psi_j(t_0) + \Psi_j(t_0 + \Delta t)}{2} \right) \tag{3.18}$$

Note, that the updated wavefunction shows up on the right hand-side. Finding $\Psi_j(t_0 + \Delta t)$, thus, requires to solve a linear equation system. Using matrix inversion, the equation can be written as

$$\Psi_j(t_0 + \Delta t) = (I - \frac{\Delta t}{2} \mathcal{A})^{-1} (\Psi_j(t_0) + \frac{\Delta t}{2} \mathcal{A} \Psi_j(t_0)) \tag{3.19}$$

Another popular unitary algorithm is the pseudo-spectral method. Here, kinetic operator $-\frac{i\hbar}{2ma^2}\nabla^2$ and the gravitational operator iVm are applied separately in an alternating fashion. The kinetic operator is applied in Fourier space, where it reduces to the favorable expression $-\frac{i\hbar}{2ma^2}k^2$ with wavenumber k, and the gravitational operator is applied in real space. Sticking to the language with the matrix $\mathcal{A}$, both operators are represented by diagonal matrices with imaginary entries when evaluated and the update is performed by the unitary expression in equation (3.7) respectively.

The downside to the two algorithms is that in both cases the update of one grid cell depends on every other cell on the grid. This can be seen by the fact that the inverted matrix in equation (3.19) is not sparse unlike $\mathcal{A}$ and by the necessity of Fourier transforms in the pseudo-spectral method. The non-local nature of these algorithms makes their implementation into parallel codes less straightforward, because it is unclear how to distribute the grid data among several processors or even compute nodes with separate memory. For the pseudo-spectral method, one can make use of various libraries for fast Fourier transformation (FFT) with distributed memory parallelization [149].

Pseudo-spectral methods require rectangular grids and assume periodic boundaries. For this reason, they are less suited for implementation into existing codes for cosmological structure formation with adaptive mesh refinement like Enzo. Different resolution levels in AMR codes are not necessarily of rectangular shape and level boundaries are not periodic except for the root grid. Furthermore, the existing parallelization concept in terms of workload and memory distribution is not necessarily the same as the one used in the FFT libraries.

In contrast to implicit or pseudo-spectral methods, the update step in the explicit Runge-Kutta method in section 3.1.1 depends only on local grid cells with a maximum distance of 4 cells. This is similar to the hydrodynamics solvers used in grid based cosmology codes like Enzo. Thus, the 4th-order Runge-Kutta method can be straightforwardly implemented into the existing parallelization schemes of those codes.

In line with the above discussion, the pseudo-spectral method has mostly been used for simulations with uniform computational grids in the context of FDM [9; 97; 126; 150]. As is evident from the Schrödinger-Vlasov correspondence (equation (2.53)) or from the Madelung transformation (equation (2.37)), capturing the dynamics of the FDM wavefunction requires to resolve the de Broglie wavelength $\lambda_{dB} = 2\pi\hbar/(mv)$. Gravitational collapse of cosmological perturbations involves de Broglie wavelengths, which are typically very small compared to the initial size of the perturbations. For this reason, uniform grid simulations are most of the time applied to idealized set-ups of already-collapsed structures.

3.1.3 Madelung methods and N-body simulations of FDM

The necessity to resolve the de Broglie wavelength is avoided by using algorithms, that do not solve the Schrödinger equation directly, but instead use a representation in terms of velocities $\mathbf{v} = (ma)^{-1}\nabla S$ and not the phase of the Schödinger wavefunction S. One possibility is to numerically solve the Madelung equations (equations (2.38) and (2.39)). Analogous to the developments in numerical hydrodynamics, two approaches can be found in the literature: on the one hand, Lagrangian particle based methods, where elements of fixed mass represent the flow of matter and interact with each other due to pressure forces (in this case the quantum pressure) [2; 151; 152] and, on the other hand, Eulerian grid based solvers [153]. However, the accuracy and convergence behaviour of these Madelung based methods are not well tested. Specifically, all of them more or less fail to produce the correct interference patterns in situations where matter flows with different velocity vectors overlap.

A more pragmatic approach is to make use of the Schrödinger-Vlasov correspondence without attempting to cover the small scale deviations at all. Then, a standard N-body scheme, like in simulations of CDM is sufficient. This approach has been used in studies of the effect of the linear power spectrum suppression

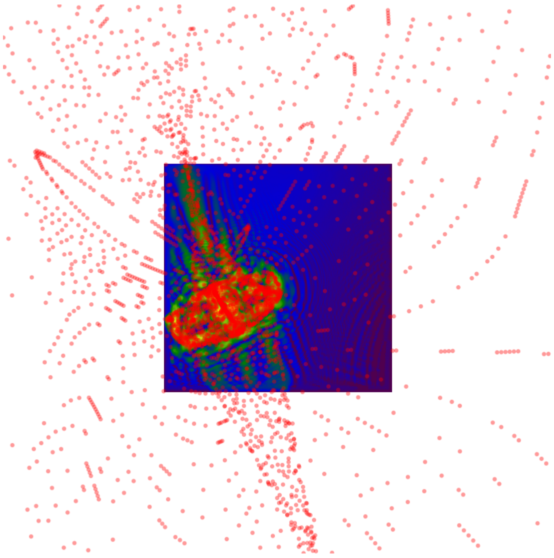

Figure 3.2: Illustration of the hybrid method with N-body particles in red and Schrödinger field in blue and green.

(equation (2.43)) on the non-linear evolution [115; 116]. All relevant effects of FDM are then already present in the initial conditions. The same approach is typically used in WDM simulations [88].

3.1.4 A hybrid approach

The general idea behind the hybrid method used in chapter 4 and chapter 5 is to combine the accurate, stable and easy-to-parallelize 4th-order Runge-Kutta solver of section 3.1.1 with the cost-efficient pragmatic approach of using N-body simulations described at the end of the last section. This method is especially well suited for simulations of galaxy formation with FDM. Inside a dark matter halo, the Runge-Kutta solver computes the detailed behaviour of the Schrödinger field at de Broglie scales. In the greater environment of the halo, the N-body solver is responsible for the initial collapse of the seed overdensity, subsequent mass accretion and for the large scale gravitational field in which the halo resides. The method requires to resolve the de Broglie wavelength only in the domain of the Schrödinger solver. Thus, it can use different levels of refinement avoiding the limitations of uniform grid simulations.

The crucial point in the realization of this idea are the boundary conditions of the Schrödinger solver. Obviously, they must be defined in some way by the N-body solver, such that particles entering the Schrödinger domain, for example, are converted into a field representation. Due to the approximate nature of the

Schrödinger-Vlasov correspondence, the exact solution to the Schrödinger equation can only be approximately constructed from the information provided by the N-body particles. The aim of any adopted prescription must be to reproduce important statistical properties the exact solution would have.

Concretely, in the prescription adopted here, the particle density directly determines the field density $\rho = a^{-3}m|\Psi|^2$ in the boundary region. Particles with index i, mass m_i, position $\mathbf{x_i}$ and velocity $\mathbf{v_i}$ are smoothed with a second order interpolation kernel

$$W(|\mathbf{x}-\mathbf{x_i}|) = m_i \frac{3}{\pi\xi^3}\left(1 - \frac{|\mathbf{x}-\mathbf{x_i}|}{\xi}\right) \tag{3.20}$$

for $|\mathbf{x}-\mathbf{x_i}| < \xi$ and 0 elsewhere. Then, the amplitude of the Schrödinger field is given by

$$|\Psi(\mathbf{x})| = \sqrt{\frac{1}{m}\sum_i W(\mathbf{x}-\mathbf{x_i})} \tag{3.21}$$

With this formulation, the boundary conditions obviously do not contain interference fringes, even if the velocity distribution is multi-valued. On the positive side, mass is exactly conserved in the conversion from particles to field.

The complex phase of the constructed boundary conditions is obtained by letting each N-body particle carry a phase S_i, which is interpolated onto the grid according to

$$S(\mathbf{x}) = \arg\left[\sum_i \sqrt{W(\mathbf{x}-\mathbf{x_i})}e^{i(S_i+\mathbf{v_i}\cdot a(\mathbf{x}-\mathbf{x_i}))m/\hbar}\right] \tag{3.22}$$

The phase of each particle is initialized at the beginning of a simulation from the initial velocity field by solving the Poisson equation

$$\nabla\cdot\mathbf{v} = a^{-1}\nabla^2 S \tag{3.23}$$

on the computational grid and interpolating to the particle positions. The equation is obtained by applying the ∇-operator on both sides of the relation $\mathbf{v} = (a)^{-1}\nabla S$, which, as discussed in section 2.4.2, can be used for the initialization of the wavefunction in cosmological simulations [128]. The particle phase is evolved according to the equation

$$\frac{\mathrm{d}S_i}{\mathrm{d}t} = \frac{1}{2}\mathbf{v_i}^2 - V(\mathbf{x_i}) \tag{3.24}$$

To illustrate this overall prescription for the boundary conditions, it is useful to note that it computes the so-called ”classical wave function” as long as the velocity distribution is single-valued [154; 155]. The classical wave function is derived by dropping the quantum pressure term in the Madelung equations, resulting in the pressureless fluid equations, and then transforming back to a wave function representation. Specifically, the polar decomposition of the Schrödinger equation yields the following equation for the complex phase S

$$-\frac{\partial S(x,t)}{\partial t} = \frac{1}{ma^2}\left(\nabla S(x,t)\right)^2 + V(x,t) - \frac{\hbar^2}{2m^2a^2}\frac{\nabla^2\sqrt{\rho}}{\sqrt{\rho}} \tag{3.25}$$

Now, dropping the quantum pressure and using $\mathbf{v} = (ma)^{-1}\nabla S$ gives the classical Hamilton-Jacobi equation

$$-\frac{\partial S(x,t)}{\partial t} = \frac{m}{2}\mathbf{v}^2 + V(x,t) \tag{3.26}$$

Writing this equation in terms of the total derivative $\frac{\mathrm{d}S(x,t)}{\mathrm{d}t} = \frac{\partial S(x,t)}{\partial t} + a^{-1}\mathbf{v}\nabla S(x,t)$ yields equation (3.24). The equation of motion for the classical wave function reads [154]

$$i\hbar\dot{\Psi}_{cl} = -\frac{\hbar^2}{2ma^2}\nabla^2\Psi_{cl} + Vm\Psi_{cl} + \frac{\hbar^2}{2ma^2}\frac{\nabla^2|\Psi_{cl}|}{|\Psi_{cl}|} \tag{3.27}$$

which is equivalent to the Schrödinger equation apart from the last term canceling quantum pressure effects. The smaller the quantum pressure, the better will be the approximation of the exact Schrödinger equation.

Another way to understand the prescription is to think of the particles as independent wave packets like in the discussion at the beginning of section 2.4.2. If their widths are sufficiently large, the contribution of the quantum pressure in equation (3.25) is negligible and their central phases are given by equation (3.24). For the construction of the total wave function, the wave packets are superimposed, but in a way that erases interference patterns.

Since a 4th-order Runge-Kutta update of single cell depends on all cells in a box with 4 cells radius centered on that cell, the boundary region of the Schrödinger domain requires a minimum thickness of 4 cells. Before each timestep, the hybrid algorithm constructs the wavefunction according to equations (3.21) and (3.22) in this boundary region. N-body particles inside the Schrödinger domain are passively co-evolved. They do not contribute to the gravitational field. Instead, the Schrödinger density $\rho = a^{-3}m|\Psi|^2$ does.

3.2 Standard ingredients to cosmological simulations

3.2.1 Initial conditions

Since cosmological simulations of structure formation typically start at redshifts where perturbations are still linear, producing initial conditions for them amounts to producing a realization of a Gaussian random field with a given power spectrum $P(k)$. A common way to achieve this, is to generate Gaussian white noise $\mu(\mathbf{x})$ first. This is done by assigning each cell of the computational grid a random overdensity drawn from a Gaussian distribution centered around zero with a standard deviation of 1. Since Gaussian white noise is a Gaussian random field with constant power spectrum $P(k) = 1$, a field with a different power spectrum can now be obtained by multiplying μ with the desired power spectrum in Fourier space

$$\delta_{\mathbf{k}} = \sqrt{P(k)} \cdot \mu(\mathbf{k}) \tag{3.28}$$

Baryon acoustic oscillations and Silk damping cause the baryon power spectrum to differ from the dark matter one. This can be accounted for by using different power spectra in the multiplication in equation (3.28) to produce the respective density fields. Given those density fields, the initial displacements of an otherwise uniform distribution of dark matter particles, as well as their initial velocities and the velocities of the baryon field are computed by the Zel'dovich approximation (equations (2.21) and (2.22)). The public code MUSIC [156] is able to perform all of the steps just described.

3.2.2 Poisson equation

In each timestep involving the update of dark matter particles or FDM wavefunction and, if present, the baryon field, the gravitational potential V has to be computed via the Poisson equation

$$\nabla^2 V = 4\pi G a^2 (\rho - \bar{\rho}) \tag{3.29}$$

where ρ is the total matter density. In Enzo, the Poisson equation on the root grid is solved by fast Fourier transformation, as the differential operator reduces to a multiplication by k^2 in Fourier space. On additional refinement levels, the gravitational potential is computed with a multigrid relaxation technique where the boundary conditions are provided by the next coarser level respectively.

3.2.3 Collisionless particles

Positions $\mathbf{x}$ and velocities $\mathbf{v}$ of collisionless N-body particles in Enzo are advanced by a drift-kick-drift method. This symplectic scheme ensures energy conservation.

$$\mathbf{x}^{n+1/2} = \mathbf{x}^n + \frac{\Delta t}{2a^n}\mathbf{v}^n \tag{3.30}$$

$$\mathbf{v}^{n+1} = \mathbf{v}^n \left(1 - \frac{\dot{a}^{n+1/2}}{a^{n+1/2}}\right) + \frac{\Delta t}{a^{n+1/2}}\mathbf{g}^{n+1/2} \tag{3.31}$$

$$\mathbf{x}^{n+1} = \mathbf{x}^{n+1/2} + \frac{\Delta t}{2a^{n+1}}\mathbf{v}^{n+1} \tag{3.32}$$

The upper indices denote the timestep. The gravitational acceleration $\mathbf{g}$ is determined for each particle by computing the gradient of the potential V on the grid and then interpolating it to the particle position.

3.2.4 Hydrodynamics

The evolution of baryonic matter is governed by the fluid equations equations (2.6) and (2.7)

$$\frac{\partial \rho}{\partial t} + 3\frac{\dot{a}}{a}\rho + \frac{1}{a}\nabla(\rho\mathbf{v}) = 0 \tag{3.33}$$

$$\frac{\partial \mathbf{v}}{\partial t} + \frac{\dot{a}}{a}\mathbf{v} + \frac{1}{a}(\mathbf{v}\cdot\nabla)\mathbf{v} + \frac{1}{a}\frac{\nabla p}{\rho} + \frac{1}{a}\nabla V = 0 \tag{3.34}$$

To close the system, an additional evolution equation for the specific internal energy density e is needed

$$\frac{\partial e}{\partial t} + \frac{1}{a}(\mathbf{v}\cdot\nabla)e + \frac{2\dot{a}}{a}e + \frac{p}{\rho a}\nabla\cdot\mathbf{v} + \frac{a^3\Lambda}{\rho} = 0 \tag{3.35}$$

where Λ is an additional heating and cooling term induced by radiative processes discussed in the next section. The specific energy density is related to the pressure and density of the gas by an equation of state

$$e = \frac{p}{\rho(\gamma - 1)} \tag{3.36}$$

with $\gamma = 5/3$ for an ideal monoatomic gas. ENZO provides a variety of eulerian grid-based methods to solve the equations above. The simulations in chapter 5 use the finite-difference solver ZEUS [157]

3.2.5 Heating and cooling

Heating and cooling of gas by radiative processes is an important factor in simulations of galaxy formation. On the one hand, as discussed in section 2.1.1, it is the ability to cool that allows baryons to contract inside dark matter halos and form galaxies. On the other hand, heating by the metagalactic UV background prevents galaxy formation in halos below $M_h \approx 10^9$ $\mathrm{M}_\odot$. These two examples show, why it is of high importance to model radiative processes as accurately as possible in simulations of galaxy formation.

The simulations in chapter 5 make use of ENZO's non-equilibrium chemical network routine to compute heating and cooling rates. It solves the rate equations for reactions between the six chemical species H, H^+, He, He^+, He^{++}, e^-. Processes leading to the emission of photons and, in turn, cooling are collisional excitations of atoms and subsequent radiative relaxation, recombination of nuclei with electrons, free-free emission by collisions of electrons, inverse Compton scattering of electrons with the CMB. Heating is provided by absorption of photons from the UV background.

Although the UV background is produced by young galaxies and quasars, in other words objects that should be contained in the cosmological volumes simulated in cosmological simulations, it is typically modelled as a uniform radiation field with predefined spectrum. The simulations in chapter 5 use the spectrum computed in [158].

Due to the many species and processes involved, the cooling provided by heavier elements than helium, produced in stellar processes, is costly to simulate with a non-equilibrium chemical network like in the case of the primordial species. For this reason, metal cooling is included in the simulations of chapter 5 by using a predefined cooling function assuming a solar composition of elements from [159]. It returns the cooling rate depending on the temperature and metallicity of the gas.

Since most of the cooling processes listed in this section are two-body processes, their rates scale with ρ^2. This is why the dominant cooling mechanism in the intergalactic medium is the expansion of the universe (the third term in equation (3.35)). The temperature of the IGM can be well approximated by assuming equilibrium of this cooling rate and heating by the UV background [25]. In collapsed objects, however, radiative cooling mechanisms dominate.

3.2.6 Star formation and feedback

The formation of individual stars in galaxies happens on spatial and temporal scales that normally are not resolved in cosmological simulations. Moreover, the process involves physics which is not modelled in those simulations at all. Star formation is known to take place in dense and cool molecular clouds and is affected by magnetic fields and turbulence. Consequently, prescriptions for star formation in cosmological simulations have to consist of coarse-grained laws depending on averaged large-scale properties of the star forming gas like density, temperature and metallicity. The fact that these laws cannot be derived from first principles but instead have to rely on heuristic reasoning and empirical findings has lead to a large variety of star formation prescriptions in the literature. They typically introduce a number of free parameters, that account for unresolved or insufficiently understood physical processes. These parameters are then tuned to reproduce empirical relations like the Kennicutt-Schmidt law, which relates the increase of the surface density of stars Σ_* to the surface density of gas Σ_{gas} in a galaxy [25; 160]

$$\dot{\Sigma}_* = (2.5 \pm 0.7) \times 10^{-4} \left(\frac{\Sigma_{gas}}{\mathrm{M_\odot pc^{-2}}} \right)^{1.4\pm0.15} \mathrm{M_\odot yr^{-1} kpc^{-2}} \tag{3.37}$$

The simulations in chapter 5 use the star formation and feedback model introduced by Cen & Ostriker [161]. It is part of the public version of Enzo. Star formation in a given cell is allowed if the following criteria are met:

- The overdensity of gas exceeds a value given by the free parameter η.

$$\frac{\rho_b}{\bar{\rho}_b} > \eta \tag{3.38}$$

- Gas flow is converging.

$$\nabla \cdot \mathbf{v} < 0 \tag{3.39}$$

- The cooling time is shorter than the dynamical time.

$$t_{cool} < t_{dyn} \equiv \sqrt{3\pi/32G\rho_{tot}} \tag{3.40}$$

- Gas in the cell is Jeans unstable (see equation (2.15)).

$$m_b > m_J \equiv \frac{\pi^{5/2}}{6} G^{-3/2} \rho_b^{-1/2} c_s^3 \tag{3.41}$$

If all the conditions are fulfilled in a timestep of the length Δt and the mass

$$m_* = f_* m_g \frac{\Delta t}{t_{dyn}} \tag{3.42}$$

is larger than a predefined threshold $m_{*,min}$, a star particle with this mass created and the same mass is subtracted from the gas density. The star particle is placed in the center of the cell and given the same initial velocity as the gas. Then, it is treated as a collisionless N-body particle like in section 3.2.3 for the rest of the simulation.

In the model of Cen & Ostriker, stellar feedback is modelled by adding a certain amount of thermal energy into the cell in which a star particle resides. This amount is commonly expressed as a fraction of the rest mass energy of a star particle

$$E = f_{SN} m_* c^2 \tag{3.43}$$

A reasonable value for f_{SN} can be found by noting that a supernova releases approximately 10^{51} erg of energy and that a supernova approximately occurs once for every 200 $\mathrm{M}_\odot$ of stars being formed [145]. This gives

$$f_{SN} \approx \frac{10^{51}\ \mathrm{erg}}{200\ \mathrm{M}_\odot c^2} \approx 3 \times 10^{-6} \tag{3.44}$$

In addition to thermal energy, star particles inject a fraction f_Z of its mass in form of metals into its environment. Since a star particle does not represent a single star, but instead an entire population of stars, the model implemented in ENZO distributes feedback over the timescale t_{dyn} in order to account for the different formation times and lifetimes in the stellar population.

$$\dot{E} \sim \frac{t}{t_{dyn}} \exp[-t/t_{dyn}] \tag{3.45}$$

Although seemingly well-motivated, this thermal-only prescription of stellar feedback is known to suffer from *overcooling* if the spatial resolution is not high enough. Since feedback energy is then injected into a region which is too large (the size of a cell), it is radiated away too efficiently. The stabilizing effect of stellar feedback is weakened leading to extreme collapse of gas in galaxies and, in turn, unrealistically high star formation rates [162]. One method to prevent this is to artificially turn off cooling in gas which has received feedback energy for a certain amount of time. This ad-hoc method was shown to achieve desired results in the sense that catastrophic gas collapse is prevented and star formation rates drop to realistic values [163]. Cooling suppression is also used in chapter 5.

Chapter 4

Dark matter only simulations

This chapter discusses results from dark matter only simulations of the formation of FDM halos in the mass range of dwarf galaxies. In 2018, the results including all figures in this chapter were published in an article with the title "Formation and structure of ultralight bosonic dark matter halos" in *Physical Review D* [3]. The author of this thesis set the simulations up, ran them and produced the figures in this chapter based on discussions with his co-authors Jens Niemeyer and Bodo Schwabe. In particular, figures 4.3, 4.4 and 4.6 resulted from ideas by the author of this thesis.

Besides providing a proof-of-concept for the newly developed hybrid algorithm, the goal of the simulations was to better understand the processes behind the small scale structure of FDM halos observed in previous simulations [1]. A specific question was how to explain the formation of solitonic cores and their core-halo mass relation equation (2.52) in the light of the concepts discussed in section 2.4.2, the Schrödinger-Vlasov correspondence and relaxation/condensation mechanisms. Answering this question would allow extrapolations to more massive halos, since cosmological FDM simulations with resolved de Broglie wavelength are so far limited to virial masses below $M_h \sim 10^{11}$ $\mathrm{M}_\odot$ [100]. There are different proposals in the literature regarding this question. While some authors invoke relaxation effects as the main mechanism [113; 129; 164], others invoke solely the Schödinger-Vlasov correspondence to explain core properties [9].

Admittedly, the more important reason for the focus on dwarf galaxies is the same resolution restriction that prevented other groups from simulating galaxies of higher mass. The larger de Broglie wavelength in dwarf galaxies is simply easier to resolve. Furthermore, dwarf galaxies form out of initial overdensities of smaller wavelength. Thus, the ratio between total box size and numerical cell size can be chosen smaller. The second reason is the high mass-to-light ratio of dwarf galaxies which allows for easier measurements of the dark matter profile in observations as discussed in section 2.2 and, consequently, constraints on the scalar field mass (see section 2.4.1).

4.1 Simulation setup

The simulations use a so-called zoom-in technique. In a low-resolution run of a cosmological volume large enough to contain several halos of a given size, a particular halo is selected and its positional data extracted. Then, the same box is resimulated with additional levels of higher resolution centered on that halo. The most refined level corresponds to the Schrödinger domain of the hybrid method. The smoothing radius ξ in the kernel function, equation (3.20), was chosen to be $\xi = 8\Delta x$, a trade-off between sufficient smoothness of the interpolation and computational cost.

Initial conditions were generated according to the procedure in section 3.2.1 with the public code Music [156]. The code supports the use of custom transfer functions for FDM with the most important effect being the small scale power suppression due to the Jeans scale (equation (2.43)). They were generated with AxionCAMB [165], which solves the relativistic equations for linear structure formation of FDM. All simulations have a side length of 2.5 Mpc/h, with $h = H_0/(100$ km/s/Mpc). The following cosmological parameters were chosen in rough correspondence to cosmological measurements [24]: $H_0 = 70$ km/s/Mpc, $\Omega_\Lambda = 0.75$, $\Omega_m = \Omega_{FDM} = 0.25$. In all runs, the scalar field mass is $m = 2.5 \times 10^{-22}$ eV and the initial redshift is $z = 60$.

On top of the root grid with 512^3 cells, two nested static refinement levels with a side length of roughly a quarter of the total domain are centered on the Lagrangian patch of a previously chosen halo. Three additional refinement levels with side lengths of 0.0625 Mpc/h trace the position of the halo. Using a refinement factor of two between levels, the finest one is resolved with a cell width of $\Delta x = 150$ pc/h.

To minimize computational cost, the Schrödinger solver is applied only after a redshift of $z \approx 7$. At this redshift, the wave function is initialized with the same prescription as the one used for the boundary conditions. Because the velocity distribution of particles is still single-valued and the gradient energy of the resulting field is negligible at this point, the approximations involved in the construction of the wavefunction according to section 3.1.4 are moderate.

In total, seven halos with a mass range between 8×10^8 $M_\odot$ and 7×10^{10} $M_\odot$ were simulated. For comparisons with standard CDM dynamics, five of these simulations were rerun with only the N-body solver using identical grid resolution, level setup and FDM initial conditions. The virial mass of a simulated halo is determined via its theoretical overdensity ζ derived from the spherical collapse model (see equation (2.25)) . It is the mass enclosed by the virial radius, r_{vir},

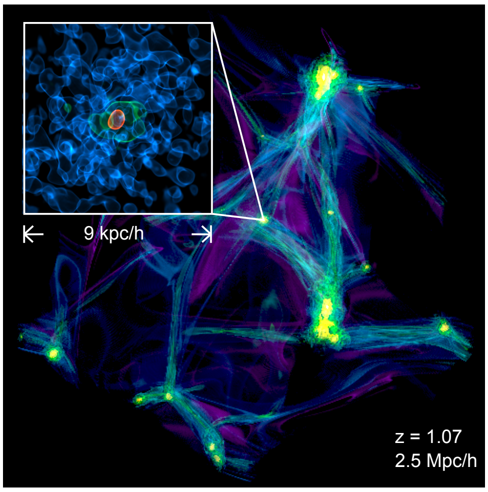

Figure 4.1: Volume rendering of a typical simulation. The large box shows the N-body density in the full simulation domain, the inlay shows the density of the Schrödinger field in the central region of the indicated halo. The density thresholds in the inlay are set to 0.75, 0.05 and 0.01 times the maximum density. © 2018 American Physical Society [3]

defined as the radius where the enclosed mean density is equal to $\zeta\bar{\rho}$. All simulated halos evolve without major mergers. Halos of this kind are more abundant in FDM cosmologies relative to CDM because of the small scale cut-off in the power spectrum.

The simulations ran on the HLRN-III system of the North-German Supercomputing Alliance. Using 16 computer nodes with 24 cores each, the FDM simulations took $\sim$ 1 week in real time. The snapshots analyzed in the next section use $\approx$ 30 Terabyte of storage space in total.

4.2 Results

4.2.1 Numerical parameters

The maximum difference between total mass of the Schrödinger field and total mass of the passively co-evolved particles in the Schrödinger domain is 10 % in all simulations. This shows that the particle-to-field conversion in the hybrid method successfully conserves an important statistical quantity, namely the rate of mass inflow. It was furthermore checked that the smoothing radius ξ of the particle kernel and the redshift of initialization of the wavefunction, have no systematic effects on the resulting core mass in figure 4.5 but produces statistical scattering of 30%.

4.2.2 General halo structure

A typical snapshot of one of the simulations is shown in figure 4.1. The zoomed-in view on the central region of the resolved halo shows the configuration found in previous simulations: A central core (in red) surrounded by granular structure of approximately the same size.

Radial density profiles centered around the maximum density of four representative halos are compared with results from pure N-body runs in figure 4.2. Taking radial density profiles already involves smoothing the density by averaging over spherical shells. Consequently, the granular structure of FDM halos which deviates strongly from the smooth CDM density field on small scales, is not visible apart from a small region around the solitonic core. The radially averaged core profile agrees well with previous results [1; 166; 167]. Among the five halos in the sample that were rerun with a pure N-body solver, the maximum FDM core density was exceeded by the maximum density of the corresponding CDM halo in all cases but one, by a maximum factor of 7.5.

Outside of the core, the FDM and N-body (CDM) profiles deviate by at most 50% while the overall density varies by multiple orders of magnitude. The residuals between the CDM and FDM halo profiles in figure 4.2 highlight the differences. The deviations are not correlated among different halos and may be caused by nonlinear amplification of numerical noise. In summary, the comparison of radial density profiles shows, that the density distribution on scales larger than the de Broglie wavelength can be explained by the Schrödinger-Vlasov correspondence.

In order to compare FDM and CDM halos in momentum space, recall that the Wigner quasi-probality distribution (equation (2.53)) is expected to resemble the phase space distribution of the Vlasov-Poisson equations, when both are coarse-grained with a Gaussian filter obeying $\sigma_x \sigma_p \geq \hbar/2$ [127; 128]. In the extreme case of averaging over the entire position space, the global momentum distribution is obtained from the Fourier transform of Ψ,

$$\begin{aligned} f_{\mathrm{W}}(\mathbf{p}) &= \frac{1}{N} \int \mathrm{d}^3x f_{\mathrm{W}}(\mathbf{x}, \mathbf{p}) \\ &= \frac{1}{N} \int \mathrm{d}^3x \int \mathrm{d}^3y \exp\left[2\frac{i}{\hbar}\mathbf{p}\cdot\mathbf{y}\right] \Psi(\mathbf{x}-\mathbf{y})\Psi^*(\mathbf{x}+\mathbf{y}) \\ &= \frac{1}{N} \int \mathrm{d}^3x \int \mathrm{d}^3y \exp\left[\frac{i}{\hbar}\mathbf{p}\cdot(\tilde{\mathbf{y}}+\tilde{\mathbf{x}})\right] \Psi(-\tilde{\mathbf{y}})\Psi^*(\tilde{\mathbf{x}}) \\ &= \frac{1}{N} \left| \int \mathrm{d}^3x \exp\left[-\frac{i}{\hbar}\mathbf{p}\cdot\mathbf{x}\right] \Psi(\mathbf{x}) \right|^2 = \frac{1}{N} |\tilde{\Psi}(\mathbf{k})|^2 \end{aligned} \tag{4.1}$$

with $\mathbf{p} = m\mathbf{v}$ and a normalization factor N.

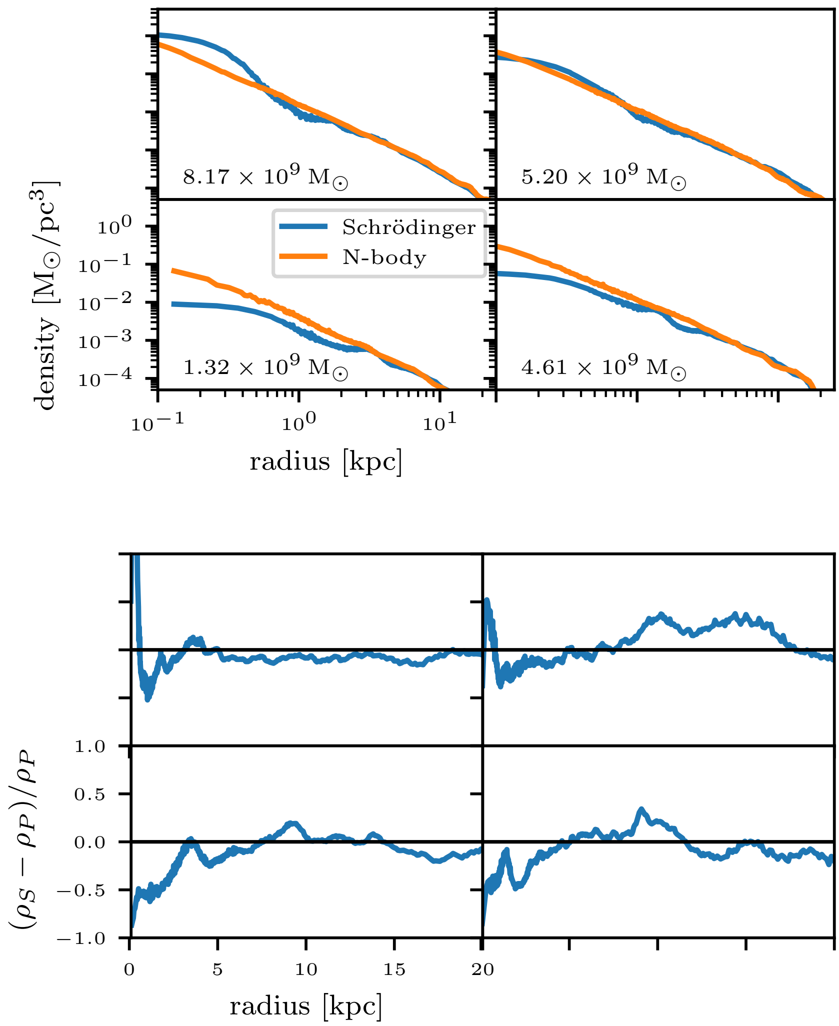

Figure 4.2: Top: Radial FDM and CDM density profiles of four representative halos. The labels indicate their virial masses. Bottom: Residuals of the same profiles in a linear plot. © 2018 American Physical Society [3]

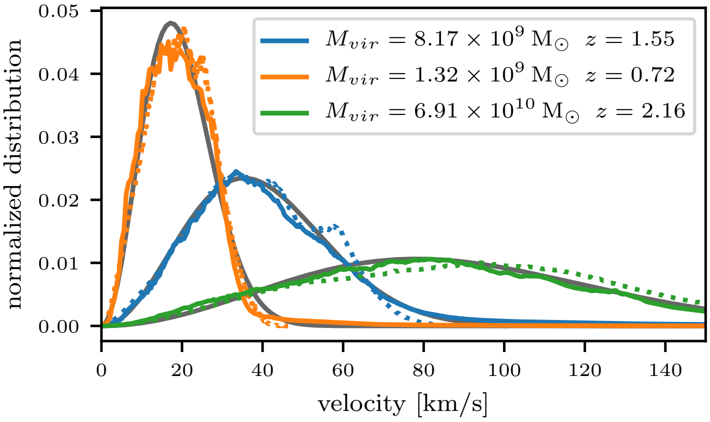

Figure 4.3: Velocity distribution of plane waves in the Schrödinger field inside the virial radius (solid lines) and of particles in the same region (dotted lines). The grey solid lines show fitted Maxwellian distributions.
© 2018 American Physical Society [3]

In figure 4.3, $f_{\mathrm{W}}(v)$ is compared to the velocity distribution $f(v)$ from the corresponding CDM simulations. As predicted by the Vlasov-Schrödinger correspondence, the normalized distribution of Fourier amplitudes matches very well the velocity distribution of particles in the N-body runs inside of the virial radius. Since the velocity distribution of virialized CDM halos is in rough approximation given by a Maxwellian distribution,

$$f(v)dv = \frac{4}{\pi}\left(\frac{3}{2}\right)^{3/2}\frac{v^2}{v_{\mathrm{rms}}^3}\exp\left(-\frac{3}{2}\frac{v^2}{v_{\mathrm{rms}}^2}\right)dv\ , \tag{4.2}$$

where v_{rms} is the root-mean-square velocity [168], figure 4.3 also shows Maxwellian distributions fitted to the Schrödinger results.

A powerful illustration of the difference between the core and the granular density fluctuations that make up the outer halo can be obtained by comparing their virial parameters (figure 4.4). They are computed by taking spherical regions around local maxima in the density field and calculating the total kinetic and potential energy in these spheres. The radii of the spheres are given by the radius at which the angular averaged density drops to half its central value r_c. The kinetic energy is computed by subtracting the center of mass velocity from the

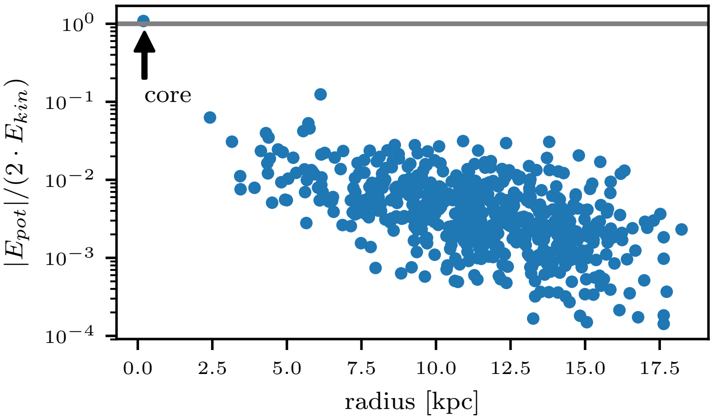

Figure 4.4: Virial parameter of local maxima (granules) at various distances to the center of the halo. © 2018 American Physical Society [3]

phase gradient and evaluating equation (2.47) expressed in physical coordinates

$$E_{\mathrm{kin}} = \int \frac{\hbar^2}{2m} |\nabla \Psi|^2 d^3\mathbf{x} \tag{4.3}$$

over the volume of the sphere. Instead of integrating exact density field like in equation (2.48), the potential energy is approximated by the expression for a uniform sphere,

$$E_{\mathrm{pot}} = -\frac{3}{5} \frac{GM^2(< r_c)}{r_c} \ . \tag{4.4}$$

This approximation is reasonable since the density profiles around local maxima are typically flattened within r_c. As can be seen in figure 4.4, the core of the halo is the only local maximum that is in itself gravitationally bound and close to virialized. It is therefore a stable object whereas the granules have a finite lifetime of order $\tau_c = \hbar/mv_{\mathrm{vir}}^2$, as confirmed by the temporal correlation functions inside and outside of the core discussed below (figure 4.7).

4.2.3 Time evolution of the core

On the one hand, the relaxation process discussed in section 2.4.2 predicts a growing core mass on the timescale of the relaxation time τ_{gr}. Equation (2.62) yields relaxation times of the order of a Hubble time $1/H_0$ for the virialized halos presented here, but the exact value depends strongly on the radius R within which the timescale is computed. On the other hand, the relation found by Schive et al. [100] (equation (2.52)) is also implicitly time-dependent via the evolving scale factor a and halo mass M_h. It is restated here for convenience:

$$M_c = \frac{1}{4} a^{-1/2} \left(\frac{\zeta(z)}{\zeta(0)} \right)^{1/6} \left(\frac{M_h}{M_0} \right)^{1/3} M_0 \tag{4.5}$$

However, there is no obvious relation between the two descriptions for core growth.

In order to test for core growth possibly allowing to distinguish between the two scenarios, figure 4.5 shows the evolution of core masses M_c in all 7 halos. M_c is defined exactly like in the core-halo mass relation given by equation (4.5): It is the mass enclosed by the half-density radius r_c. The density is assumed to follow a ground-state soliton profile (equation (2.49)), such that the core mass can be determined from its central density. As discussed below, this is only approximately true owing to the strong oscillations of the core (see figure 4.6). Spurious fluctuations of M_c resulting from oscillations of the peak density on much smaller timescales are smoothed by taking a moving average. To make core growth explicitly visible in figure 4.5, the core masses are normalized to a fixed value $M_{c,0}$, which is the core-halo mass relation evaluated roughly at the time of halo virialization. The time of virialization is determined by the requirement that the measured virial mass has settled to a slowly varying value. Using time-dependent values for a, ζ and M_h for the normalization produces differences that are small and unrelated to the halo mass. As can be seen, there is a small tendency towards smaller core masses than predicted by equation (4.5), but the relation still predicts core masses reasonable well. No systematic growth of M_c is observed for all halos but two. Thus, the simulation results do not allow for a conclusive statement on the existence of core growth or the process causing it.

Analysis of the core density with much finer temporal resolution reveals oscillations with amplitudes of more than a factor of two and a standard deviation of 33% the mean density close to the dynamical timescale of the core (figure 4.6). The frequency spectrum exhibits a peak at the quasi-normal frequency (equation (2.51)). The simulations, thus, show that cores form in a state with strong quasi-normal excitations, failing to relax to the ground state completely.

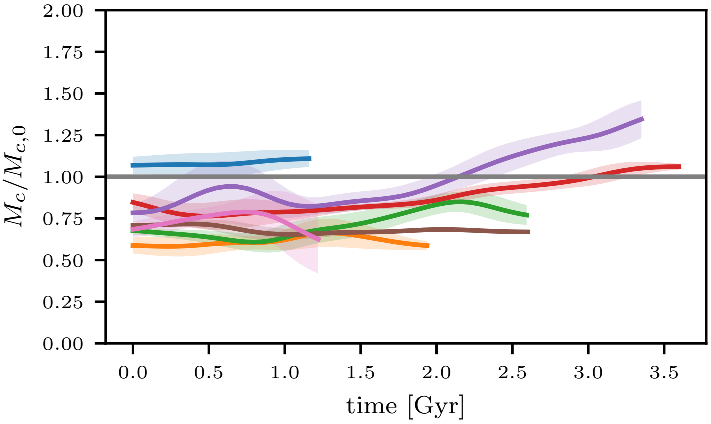

Figure 4.5: Core masses from simulated halos normalized by equation (2.52) at formation time as a function of halo age. The data points are smoothed in time with a Gaussian filter with $\sigma = 0.3$ Gyr. The shaded area represents the local standard deviation associated with the smoothing process.
© 2018 American Physical Society [3]

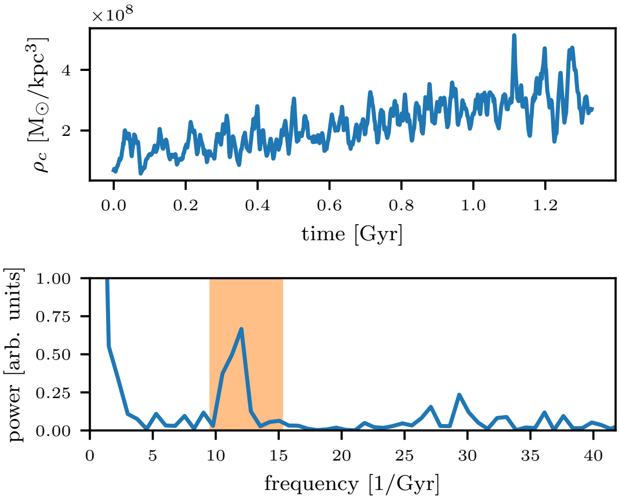

Figure 4.6: Top: Maximum comoving density of a halo over time. Bottom: Fourier transform of the same data. The boundaries of the shaded region are the expected quasi-normal periods given the minimum and maximum central density in the time series above. © 2018 American Physical Society [3]

4.2.4 Correlation functions

The spatial correlation function normalized to the virial de Broglie scale of the halo, $\lambda_{\mathrm{dB}} = 2\pi\hbar/mv_{\mathrm{vir}}$,

$$C(x) = \frac{\langle \delta(\mathbf{x_1})\delta(\mathbf{x_2})\rangle_{\mathbf{x}}}{\langle \delta^2 \rangle_{\mathbf{x}}}\,, \tag{4.6}$$

with $x = |\mathbf{x_1} - \mathbf{x_2}|$ and $\delta(\mathbf{x}) = \rho(\mathbf{x}) - \langle \rho \rangle_{\mathbf{x}}$ for a fixed halo at different redshifts can be seen in the top panel of figure 4.7. As expected, the correlation length is of order λ_{dB} across a large range of redshifts.

The temporal correlation function in the bottom panel of figure 4.7 is defined as

$$C(t, r) = \frac{\langle\langle \delta(t_1, \mathbf{x})\delta(t_2, \mathbf{x})\rangle_t\rangle_{\mathbf{x}}}{\langle\langle \delta^2(\mathbf{x})\rangle_t\rangle_{\mathbf{x}}}\,, \tag{4.7}$$

with $t = |t_1 - t_2|$, $\delta(t, \mathbf{x}) = \rho(t, \mathbf{x}) - \langle \rho(\mathbf{x})\rangle_{\mathbf{t}}$, $\langle\rangle_t$ denoting the temporal average, and $\langle\rangle_{\mathbf{x}}$ the spatial average within a radial bin with distance r to the center. $\mathbf{x}$ is comoving with the center of mass of the halo. Again, the curves are normalized to the timescales at which structure with the size of λ_{dB} is expected to evolve: $\tau_{\mathrm{c}} = \hbar/mv_{\mathrm{vir}}^2$. The temporal correlation function confirms the stability of the core apart from oscillations. In its environment, temporal correlation of the density at a fixed point is lost after $\sim \tau_{\mathrm{c}}$. The transition between the regions of long and short temporal correlation occurs at around $r = 3.5r_c$, which was previously found to be the radius where the solitonic radial profile turns into an NFW-like radial profile [167].

4.3 Discussion

Schive et al. [100] already noted, that their empirically found relation can be explained by requiring

$$M_c \sim (|E|/M_h)^{1/2} \tag{4.8}$$

The total energy of a virialized halo is given by

$$E \sim M_h^2/x_{vir} \tag{4.9}$$

and, according to the spherical collapse model, the virial radius x_{vir} by

$$x_{vir} \sim a(M_h/\zeta(z))^{1/3} \tag{4.10}$$

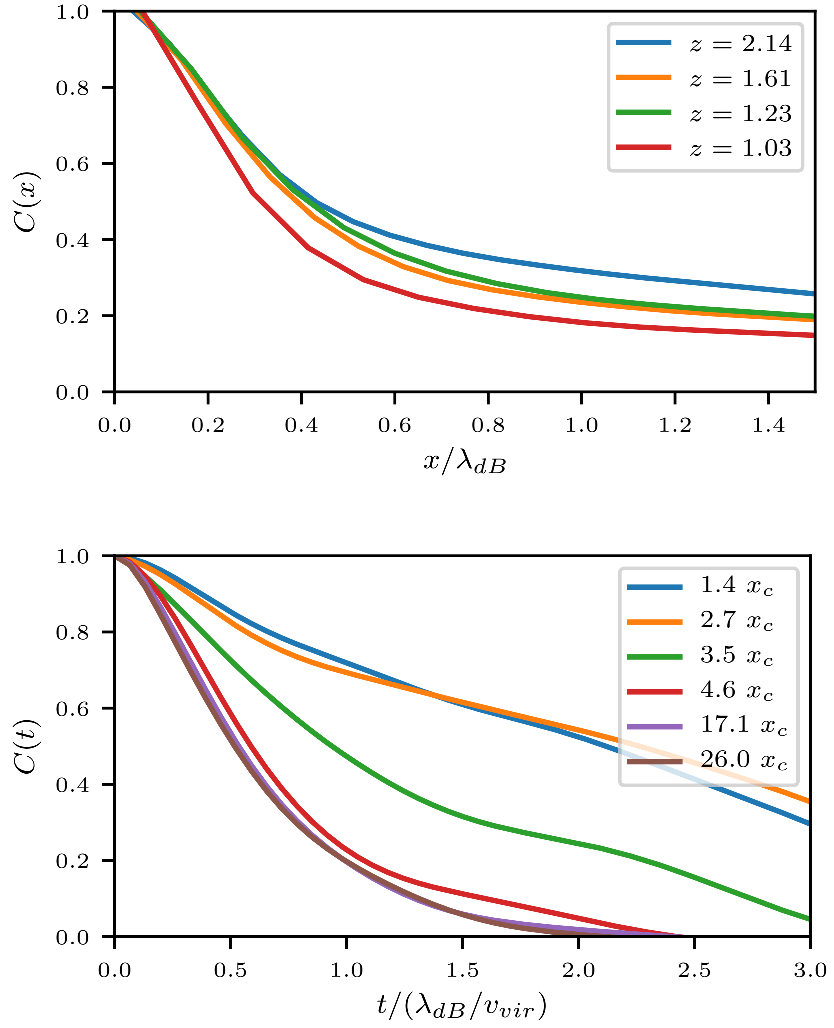

Figure 4.7: Autocorrelation function of the density field in space (*top*) and time (*bottom*) inside the virial radius of a halo. The time correlation function is averaged over locations inside a given radial bin at some factor of the core radius r_c. The coordinate system is comoving with the center of mass of the halo. Space and time units are normalized to the de Broglie wavelength corresponding to the virial velocity of the halo. © 2018 American Physical Society [3]

The scale factor a appears here, because the virial overdensity $\zeta(z)$ is defined with respect to the comoving average density of the universe, but x_{vir} has physical units. Together, the three equations yield the core-halo mass relation.

Note that, using the virial condition, equation (4.8) can also be written as

$$M_c \sim (|E|/M_h)^{1/2} \sim (K/M_h)^{1/2} \sim v_{vir} \tag{4.11}$$

Since $M_c \sim 1/r_c$ and $r_c \sim \lambda_{dB} \sim 1/v_c$, the relation requires that the velocity dispersion of the core matches the virial velocity of the halo. The comparison in figure 4.3 takes this discussion one step further, as it shows that the velocity distribution in an FDM halo, and therefore the core radius r_c, can be derived from the Schrödinger-Vlasov correspondence. However, it is unclear which mechanism is behind the formation of a soliton with the given velocity and the distinctive feature of being gravitationally self-bound as shown in figure 4.4. Furthermore, it is unclear whether the core would adapt to a changing virial velocity. The evolution of core masses over time shown in figure 4.5 unfortunately cannot answer these questions unambiguously.

Chapter 5

Simulations with gas and star formation

After performing the dark matter simulations presented in the last chapter, the obvious next step was to redo essentially the same simulations, but now with baryonic physics included making use of ENZO's standard routines for gas and star formation. Again, simulation setup and analysis of the results was done by the author of this thesis. This chapter corresponds to the *Physical Review D* article "Baryon-driven growth of solitonic cores in fuzzy dark matter halos" [4].

One might expect these hydrodynamic simulations to directly predict observables like morphology and star formation histories of dwarf galaxies possibly yielding distinctive signatures of FDM. However, due to the large diversity of those galaxy properties, such an analysis requires a large enough statistical sample. Moreover, simulating realistic galaxies is an entire steadily evolving field of research by itself requiring more considerations in terms of resolution, sub-grid models and algorithms. For these reasons, the analysis in this chapter focuses on the effect of gas and stars on the FDM distribution in halos instead of the other way around. It then suffices to use well-tested standard prescriptions for star formation together with standard parameters in order to model the baryonic content in a galaxy as realistic as possible. Nevertheless, predictions for the FDM distribution in galaxies can be equally important for comparisons with observations than more direct observables. For example, as discussed in section 2.4.1, fits to stellar kinematics or rotation curves of galaxies constraining the field mass m rely on findings from dark matter only simulations, namely the formation of a solitonic core together with its mass relation (equation (2.52)). Consequently, specific questions guiding the analysis of simulation results were: Does a core still form in the presence of baryons? If it does, what determines its properties?

First 3D numerical simulations with the aim to elaborate on these questions were done in [169]. The authors added N-body particles mimicking stars to FDM

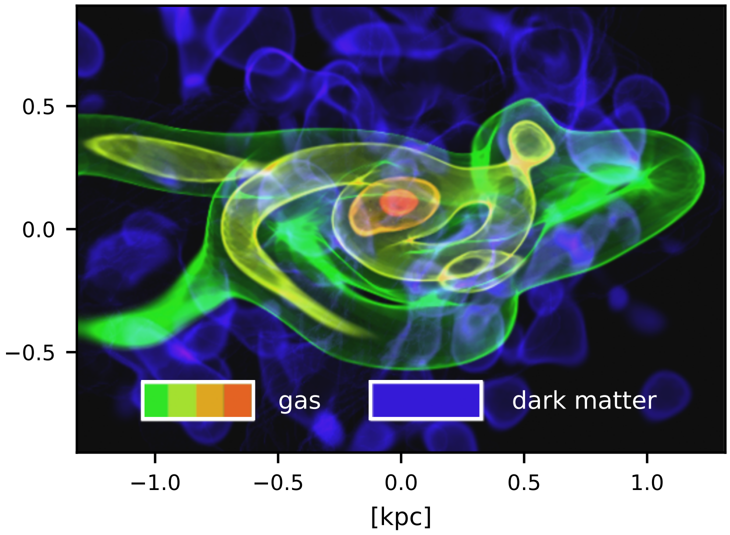

Figure 5.1: Density volume rendering of the central region of halo 1 at $z = 4.4$. © 2020 American Physical Society [4]

halos extracted from cosmological simulations and evolved the combined system further in an isolated box. They found that cores become more prominent and compact after adding stars.

5.1 Simulation setup

The simulations use the same numerical and cosmological parameters as in chapter 4 except for changes related to the inclusion of baryons. Now, the total matter fraction $\Omega_m = 0.25$ also contains a baryon fraction of $\Omega_b = 0.05$. The hydrodynamic equations of motion, radiative cooling, a uniform UV background, which is gradually ramped up between $z = 7 - 6.75$, and star formation/feedback with cooling suppression are treated with the methods discussed in section 3.2 using the same set-up of spatial grids as for dark matter. Parameters for star formation and feedback are $\eta = 100$, $m_{*,min} = 5000$ M$_\odot$, $f_* = 0.01$, $f_{SN} = 10^{-5}$. Cooling in cells which have received feedback energy is suppressed for 50 Myr. These parameters lie in the range commonly adopted by other authors to produce realistic amounts of star formation.

Like in the last chapter, halos in a low resolution CDM simulation are chosen and re-simulated with grids of higher resolution centered on that halo (zoom-in technique). This time, two halos are simulated, each with three high resolution runs: (1) collisionless N-body dynamics appropriate for CDM including baryonic physics, (2) FDM without baryons as in chapter 4, and (3) a full FDM simulation

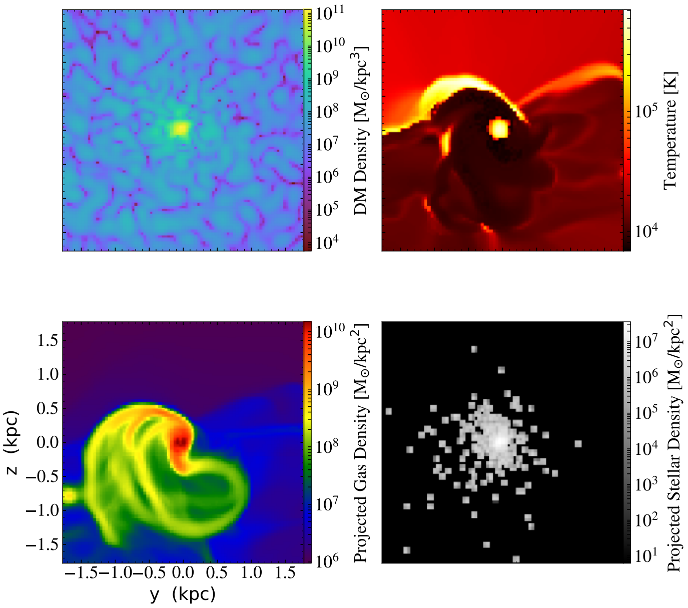

Figure 5.2: Dark matter density, temperature, gas density and stellar density of halo 1 at $z = 4$. The top row shows slices, whereas the bottom row shows projections.

including baryonic physics. Key results for the two halos are summarized in table 5.1.

Having virial masses of $M_h = 1.05 \times 10^{10}$ $M_\odot$ and $M_h = 1.25 \times 10^{10}$ $M_\odot$ at $z \approx 4$ the two halos are among the most massive ones in the simulated cosmological box. They were selected because, as discussed in section 2.2.1, the UV background prevents gas accretion in halos below $M_h \approx 10^9$ $M_\odot$. A significant impact of baryons can only be expected for halos larger than this threshold. Due to the high dark matter velocities in such massive halos, boosted by the baryons as discussed in the results section, the simulation have to be terminated at $z_f = 4$ and $z_f = 4.4$. At smaller redshifts, the de Broglie wavelength would not be sufficiently resolved.

5.2 Results

5.2.1 Star formation and feedback

In contrast to other galaxy formation simulations [56; 78], the baryon fraction inside the virial radius stays close to the cosmic baryon fraction $f_b = \Omega_b/\Omega_m$

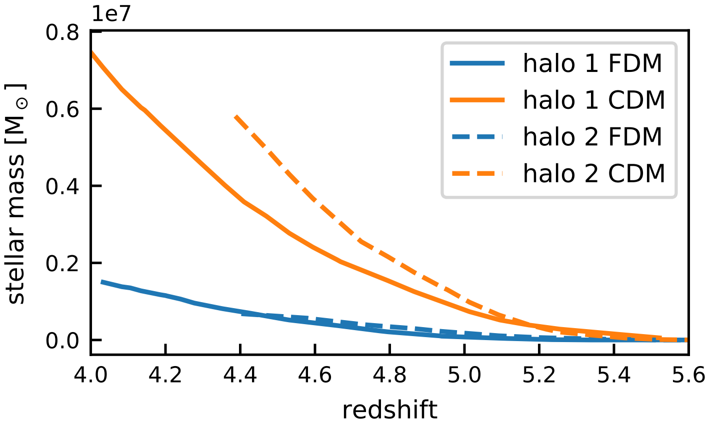

Figure 5.3: Star formation histories of both simulated halos in the FDM and the CDM runs.

throughout the simulations. Due to the relatively large halo masses, the UV background is not expected to reduce the baryon fraction [59], but stellar feedback should. Figure 5.2 shows the final configuration of dark matter, gas and stars in halo 1. As can be seen in the temperature slice, the effect of stellar feedback is limited to the central area, where it heats up the star forming gas providing pressure support in this region. Rapid expulsion of gas from the center or even the entire halo cannot be observed with the star formation and feedback model adopted here.

Figure 5.3 shows star formation histories of both halos. At $z = 4.0$ the total stellar mass of halo 1 is $M_* = 1.5 \times 10^6$ M$_\odot$ in the FDM run and $M_* = 7.1 \times 10^6$ M$_\odot$ in the CDM run. The values more or less match the modelled values in [46]. As further tests revealed, the difference of more than a factor of 4 between FDM and CDM runs is caused by different numerical timesteps Δt affecting star formation via equation (3.42). It is a numerical artifact of the star formation model and not physical.

Altogether, these findings motivate the focus on FDM properties in the rest of the results section. Star formation in the simulations mainly serves as a heating mechanism preventing central gas from runaway collapse. It should not be used for direct comparisons to observations.

5.2.2 Properties of the core

Figure 5.4 compares the radial dark matter density profiles of halo 1 at different redshifts. Also shown are the gas density profiles of the FDM run. They are

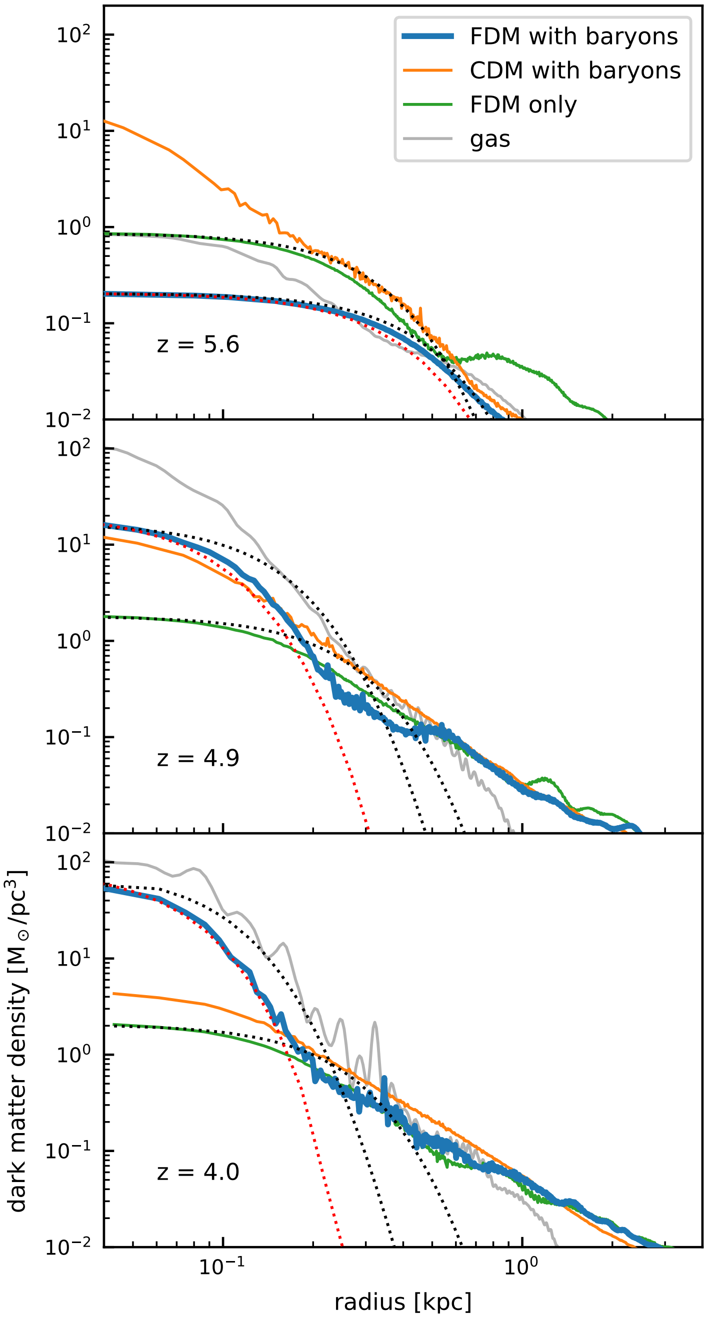

Figure 5.4: Radial dark matter density profiles of halo 1 comparing all three runs at three different redshifts. The inner profile of the FDM+baryon run matches the modified FDM ground state solution (red dotted line) instead of the dark matter only ground state solution (black dotted line). The gas density profiles in gray are taken from the FDM run. © 2020 American Physical Society [4]

halo #	z_{f}	M_{vir} [10^{10} M$_\odot$]	$M_{\mathrm{sol}}^{\mathrm{bar}}/M_{\mathrm{sol}}^{\mathrm{dm}}$	$M_{\mathrm{tot}}/M_{\mathrm{dm}}$	v_{sol} [km/s]	v_{c} [km/s]	v_{o} [km/s]	$\langle -K/W \rangle$
1	4.0	1.05	2.08	3.81	136	138	70	0.53 ± 0.07
2	4.4	1.25	3.00	3.07	159	147	77	0.54 ± 0.06

Table 5.1: Final redshift, virial mass, ratio of the soliton mass with baryons to the soliton mass without baryons given by the smoothed curve in figure 5.7, ratio of total mass to dark matter mass within $2\,r_c$, the velocities shown in figure 5.6 (soliton, central, outer), and the virial parameter $-K/W$ computed with equation (5.4) and equation (2.47) within $2\,r_c$ for both halos. All values are the final ones apart from the virial parameter which is averaged between $z = 5.6$ and z_{f}.

not significantly different to their CDM counterparts after $z \lesssim 5.4$. The highest redshift shown in figure 5.4 ($z = 5.6$) roughly corresponds to the time where the gaseous component has cooled and collapsed allowing star formation in the center. At this point, the CDM run is clearly the one with the highest central dark matter density. In contrast to its cuspy profile, the FDM runs show cores with relatively large radii, which can be expected due to the core-halo mass relation and the relatively low virial mass of the halo at this point. At $z = 4.0$, the situation has changed dramatically. The central FDM density is now more than a magnitude higher if baryons are included compared to the case where they not included. Even the central dark matter density in the CDM run is exceeded. Similar to the known results from FDM only runs, 2D-slices of the density field in figure 5.5 still show a central dark matter clump with a size roughly corresponding to the kink in the density profile at 0.2 kpc. It is surrounded by granular structure of apparently the same size. This result agrees with [169], who also found that the addition of stars to an FDM halo leads to a more prominent core. As in [169], the core profiles deviate from the soliton solution in vacuum (equation (2.49)). Their radii are too small given their central density. Instead, they are described by ground state solutions of the Schrödinger-Poisson system with the additional gravitational potential sourced by the baryon density taken into account, exactly like the authors of [108] pointed out for the simulations in [169].

The modified ground state solutions represented as red dotted lines in figure 5.4 are found as follows. Assuming spherical symmetry the gas density profile can be approximated by

$$\rho_b(r) = \frac{\rho_{b0}}{1 + (r/r_{b0})^3} \tag{5.1}$$

with the two parameters ρ_{b0} and r_{b0} fitted to the density profile found in the simulations. If the desired ground state solution is written as $\Psi(\mathbf{x}, t) = e^{-i\gamma t/\hbar}\phi(|\mathbf{x}|)$,

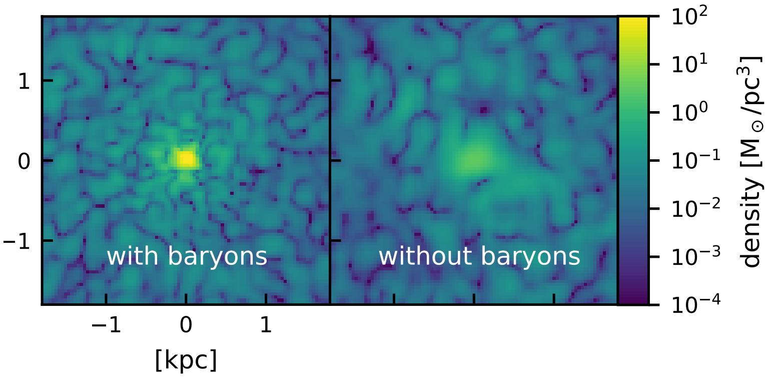

Figure 5.5: Slices of dark matter density of halo 1 with and without baryons at the final redshift $z = 4.0$. © 2020 American Physical Society [4]

then ϕ has to solve the time-independent Schrödinger-Poisson system in radial coordinates:

$$\frac{1}{r}\frac{\partial^2}{\partial r^2}(r\phi(r)) = 2(\frac{m^2}{\hbar^2}V(r) - \frac{m}{\hbar^2}\gamma)\phi \tag{5.2}$$

$$\frac{1}{r}\frac{\partial^2}{\partial r^2}(rV(r)) = 4\pi G(|\phi|^2(r) + \rho_b(r)) \tag{5.3}$$

Using a numerical ODE solver with the boundary conditions $\phi(0) = \sqrt{\rho_c}$ and $\frac{\partial}{\partial r}\phi(0) = 0$, a unique value for γ can be found, such that $\phi(\infty) = 0$ without zero-crossings. The corresponding solution $\phi(r)$ is the desired ground state.

As mean and standard deviation of the virial parameter in table 5.1 show, the simulated cores fulfill the virial condition like solitons in the vacuum. Here, the potential energy due to the collective gravitational force of baryons and the core itself is approximated as

$$W = -\frac{GM_{total}(< 2r_c)M_{dm}(< 2r_c)}{2r_c} \tag{5.4}$$

where M_{total} is the total and M_{dm} the dark matter mass enclosed within the radius 2 r_c. This expression and the kinetic energy

$$K = \frac{\hbar^2}{2m}\int \mathrm{d}^3\mathbf{x}|\nabla\Psi|^2 \tag{5.5}$$

with subtracted center-of-mass velocity of the host halo are evaluated inside the radius 2 r_c. Again, r_c is defined as the radius where the radial density profile has dropped to half the central value ρ_c. This integration radius r was chosen to include a large enough portion of the core (recall that the boundary of the soliton was at 3.5 r_c in figure 4.7). Since the resulting virial parameter depends on the exact choice of r and equation (5.4) is an approximation anyway, the values in table 5.1 should not be taken at face value.

Given an external potential from the baryons, ground state solutions depend on a single free parameter, their total mass or, as in the description above, their central density ρ_c. The empirically found core-halo mass relation (equation (2.52)) fixes this parameter in dark matter only simulations. As discussed in section 4.3, the relation can also be understood in terms of velocities. This finding, together with the decreasing granule size towards the center observed in figure 5.5, is the reason to compare the velocities of the simulated cores with velocities in their environment in figure 5.6.

Since the kinetic energy can be expressed in Fourier space as

$$K = \frac{\hbar^2}{2m}\int \mathrm{d}^3\mathbf{x}|\nabla\Psi|^2(\mathbf{x}) = \frac{1}{2}\int \mathrm{d}^3\mathbf{k}\left(\frac{\hbar k}{m}\right)^2|\tilde{\Psi}|^2(\mathbf{k}) \tag{5.6}$$

and, according to equation (4.1), $|\tilde{\Psi}|^2$ is equivalent to the spatially integrated Wigner distribution, the velocity dispersion can be computed with

$$v_{rms} = \sqrt{2\frac{K}{M}}\,. \tag{5.7}$$

M is the total field mass

$$M = \int \mathrm{d}^3\mathbf{x} m|\Psi|^2\,. \tag{5.8}$$

In figure 5.6, the core velocity is computed by evaluating the two integrals equations (5.5) and (5.8) up to a radius of 2 r_c, as in the calculation of the virial parameter. This time, the exact value does not matter much, because most of its effect cancels in the division in equation (5.7).

Local velocity dispersions in the environment of the core are determined by evaluating equation (5.7) for the field

$$\Psi_f(\mathbf{x}) = \exp\left[-\frac{(|\mathbf{x}| - f x_{vir})^2}{2\sigma^2}\right]\frac{\Psi(\mathbf{x})}{\sqrt{\rho_{prof}(|\mathbf{x}|)}} \tag{5.9}$$

Here, $\rho_{prof}(r)$ is the radial density profile of FDM. Dividing Ψ by its angular mean amplitude erases the core feature, but leaves the granular structure in the rest of the halo intact. The exponential serves as a window function at different

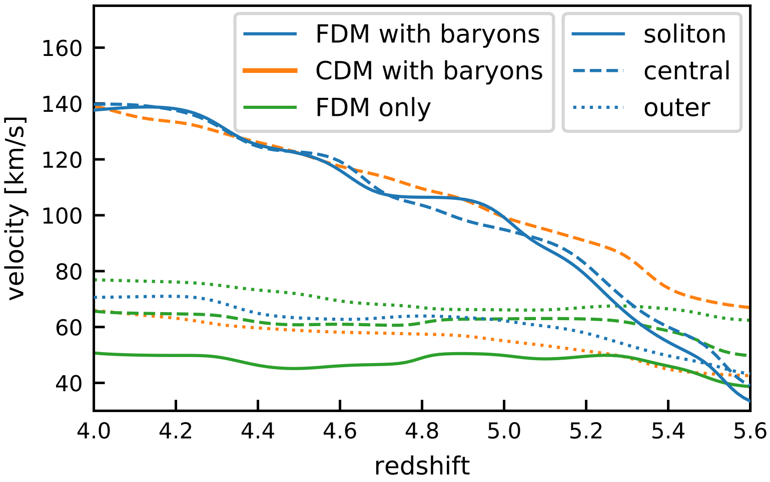

Figure 5.6: Redshift evolution of velocity dispersion in the soliton (only in the runs with FDM), its immediate surrounding and at $x_{vir}/2$ in the three different runs for halo 1. Data points are smoothed with a Gaussian filter with standard deviation of $\sigma = 0.08$ in redshift space. © 2020 American Physical Society [4]

radii, which are expressed here as fractions f of the virial radius x_{vir}.

Also plotted is the velocity dispersion of the N-body particles in the CDM run. To this end, particle masses are multiplied with the same window function as above.

$$v_{rms} = \left(\frac{\Sigma_i \exp\left[-(|\mathbf{x_i}| - f x_{vir})^2/(2\sigma^2)\right] m_i v_i^2}{\Sigma_i \exp\left[-(|\mathbf{x_i}| - f x_{vir})^2/(2\sigma^2)\right] m_i} \right)^{1/2} \tag{5.10}$$

In figure 5.6, $f = 0, 0.5$ was used for the inner and outer radius respectively and $\sigma = 0.4$ kpc, making sure to include a few de Broglie wavelengths but well below the virial radius $x_{vir} \sim 25$ kpc.

The most important finding in figure 5.6 is that the velocity dispersion of the soliton indeed matches the velocity dispersion of its immediate surrounding. Furthermore, the inclusion of baryons leads to a non-uniform velocity distribution. In all runs with baryons, the central velocity dispersion differs by up to a factor of 2 from the velocity dispersion at $x_{vir}/2$, whereas in the dark matter only runs, the velocity dispersion in the center and at the outer radius are similar. The similarity of the CDM and the FDM runs, both with baryons, suggests that the non-uniform velocity distribution is a generic result of the accumulation of gas in the center unrelated to the distinctive features of FDM.

The analysis so far does not clarify whether the core can reach the ground-state solutions with ever growing velocities by mere contraction or if it has to accumulate mass in this process. Figure 5.7 shows that the latter is the case.

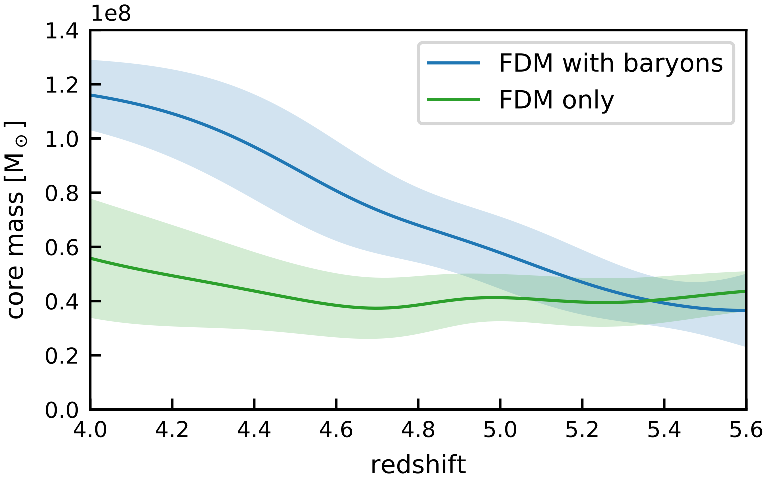

Figure 5.7: Evolution of dark matter mass within a radius $\lambda_{dB}/4$ from the center for halo 1. The lines show the Gaussian filtered data points with $\sigma = 0.2$. The shaded regions represent the corresponding standard deviation.
© 2020 American Physical Society [4]

Instead of using r_c, the core mass is here defined as the mass enclosed within a radius of $r = \lambda_{dB}/4$, where λ_{dB} is the de Broglie wavelength corresponding to the soliton velocity in figure 5.6. With this definition, the result is less dependent on the profile shape than using r_c, but values at different snapshots still show significant scattering, as the standard deviation in figure 5.7 shows. Nevertheless, one can see that the core grows by more than a factor of two in the run with baryons. In contrast, there is no clear sign of mass growth if baryons are absent, reproducing figure 4.5.

5.2.3 Core oscillations

Note that the quasi-normal frequency (equation (2.51)) is inversely proportional to the free-fall time (equation (3.40)) of the inner halo region with central FDM density ρ_c. If a baryonic component is present, the free-fall time depends on the total density ρ_{tot}. Assuming that the proportionality between quasinormal period and free-fall time holds, one expects the frequency to increase by a factor $\approx \sqrt{\rho_{tot}/\rho_c}$ in the presence of baryons. As shown in figure 5.8, the ground state configuration in the FDM simulation with baryons indeed oscillates with the frequency f multiplied by the square root of total mass divided by dark matter mass within 2 r_c averaged over time.

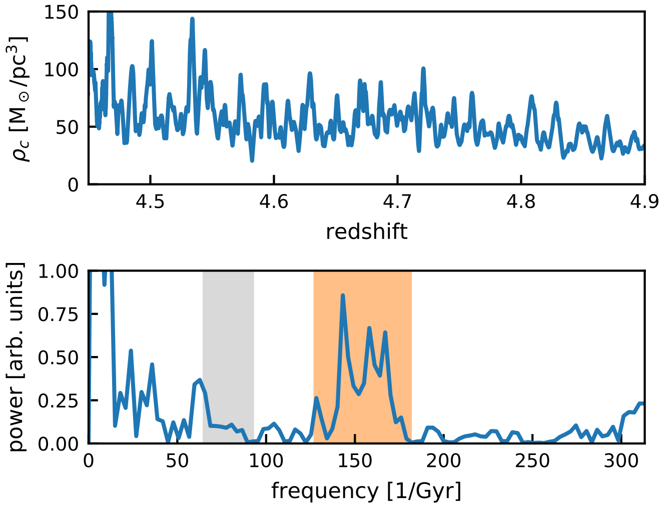

Figure 5.8: Top: Evolution of the central density in the FDM run with baryons. Bottom: Frequency spectrum of the time series above. The orange and gray regions are the expected quasinormal frequencies with and without baryons taken into account respectively. The boundaries are the expected quasinormal frequencies for the minimum and maximum central density averaged over a few periods.

5.3 Discussion

Returning to the initial questions about the existence and properties of the core, section 5.2.2 gives clear answers: The formation of central solitonic cores is a robust prediction for FDM halos, also if a significant amount of gas and stars accumulates in the center. If the local velocity dispersion increases, cores do not dissolve but adapt by growing in mass - an effect not visible in the results of chapter 4.

The core profile is determined by two effects. First, the accumulation of gas leads to a higher dark matter velocity in the center. This effect is also found in CDM simulations and not special to FDM. The velocity of the FDM core is fixed by this increased velocity. Secondly, the presence of baryons inside the core causes its profile to assume a modified ground state solution with the additional gravitational pull of the baryons taken into account. This modified profile has a mass-to-radius relation, or equivalently central density-to-radius relation, different from the one of a soliton in the vacuum. Both of these effects alter the core-halo mass relation.

It is interesting to compare the results in this chapter to those presented in [169]. There as well, the velocity dispersion of dark matter increases towards the center of the halo after the addition of a baryonic component (stars) and their cores are also described by the modified ground-states found in our simulations [108]. Over the course of a Hubble time, their cores are able to evacuate stars from the center thereby restoring the mass-to-radius relation of FDM-only solitons. Such a process is not observable in the simulations presented here. First of all, the simulation time is much shorter than a Hubble time. Apart from that, a possible evacuation effect of gas would be counteracted by the continuous gas accretion of the halo. Interestingly, the authors of [169] find that their cores are unable to acquire mass if the gravitational effect of baryons is mimicked by a static external potential. Instead, the core has to be able to transfer energy to the stellar component. If this is generally true, the mass growth of cores in this chapter hints towards a relaxation effect between baryons (star particles or gas) and FDM.

Chapter 6

Conclusion and outlook

In this thesis, a new hybrid method for simulating fuzzy dark matter was developed and applied to simulations of galaxy formation starting from cosmological initial conditions. The method combines the efficiency of N-body algorithms with the accuracy of finite difference schemes. In the applications, it has proven a viable alternative to existing codes for cosmological FDM simulations. Still, improvements are possible. One could try to use more accurate prescriptions for the construction of the boundary conditions of the finite difference scheme. *Gaussian beam* methods [170] for example would treat interference phenomena in the boundary region more accurately. Such methods inevitably come with more complexity and therefore higher computational cost. On the positive side, the region of the finite difference solver could be chosen smaller focusing only on the very central part of a halo. This way, simulations of Milky Way sized FDM halos are possibly within reach.

The dark matter only simulations in chapter 4 confirm the general halo structure found in similar works [1; 9]. Radial density profiles show a central solitonic core with a mass given by equation (2.52) while, at larger radii, they can be reproduced by CDM-like N-body simulations. Further quantitative analysis of the simulation results in chapter 4 contribute to a better understanding of the halo properties. Specifically, it was shown that the velocity distribution of FDM halos can be derived from the Schrödinger-Vlasov correspondence and is possibly part of an explanation for the core-halo mass relation. In the paper corresponding to chapter 4 ([3]), the core oscillations were quantified for the first time in cosmological simulations allowing to be probed by observations. Indeed, they were used in [125] to derive constraints on the scalar field mass from the stability of the central star cluster in a dwarf spheroidal galaxy. Furthermore, the correlation functions in figure 4.7 were used in [171] for constraints from the heating of galactic disks.

Regardless of first hydrodynamical cosmological FDM simulations in chapter 5 and [172], further dark matter only simulations can likely answer remaining questions. Interactions between FDM halos, for example through tidal forces, dynamical friction or mergers, have so far only been studied in non-cosmological setups [126; 166; 173]. Apart from that, the wave condensation/relaxation process, convincingly shown to exist in [129], deserves further studies especially with respect to its long-term behaviour. If computationally feasible, the core-halo mass relation should be tested for more massive halos than so far simulated.

Of all results presented in this thesis, chapter 5 has arguably the most direct consequences for constraints on the scalar field mass from astronomical observations and next steps are relatively clear. The results motivate a simple recipe to predict FDM core masses in galaxies for comparisons to observations: Given the baryonic contribution to the gravitational potential in a galaxy, one solves for the ground state solution of the Schrödinger-Poisson system with its velocity dispersion fixed by the central dark matter velocity dispersion. In principle, this was done in [108; 174] but their soliton velocities were given by the core-halo mass relation equation (2.52) instead of the local dark matter velocity. In chapter 5, cores become more massive and more compact when baryons are included. With this result, observed rotation curves would disfavour FDM masses around $m = 10^{-22}$ eV even more than already found in [108; 109] but detailed studies based on the above recipe are necessary. Note that the simulated halo masses ($M_h \approx 10^{10}$ $\mathrm{M}_{\odot}$) lie in the range for which rotation curve measurements are available [108; 175]. Thus, comparisons do not require an extrapolation of the recipe to higher masses than simulated.

The simulations in chapter 5 leave room for further FDM simulations with gas and star formation. The treatment of star formation and feedback should be improved leading to more realistic, perhaps more violent behaviour of the gas inside FDM halos. The best way to achieve this is obviously to increase resolution, at least for the baryonic component. Indeed, several dwarf galaxy simulations in the literature now have a high enough resolution to model supernova explosions individually as discrete events [57; 176]. Supernova blast waves, which are then resolved sufficiently, convert injected energy into momentum before it is radiated away, reducing the need for ad-hoc methods like cooling suppression. In cases where supernova blast waves are not resolved, many state-of-the-art sub-grid models for stellar feedback inject momentum instead of thermal energy into the gas causing its movement directly [176; 177; 178; 179]. However, even with these improvements the simulation of realistic galaxies remains challenging [180].

An improved treatment of feedback should reproduce the repeated expulsions of gas which, as discussed in section 2.2.2, allegedly cause core formation in CDM halos. Interaction of this process with FDM cores might lead to interesting phenomenology. In chapter 5, neither stellar feedback nor the UV background were able to expel gas from the FDM halos entirely, partly owing to their high mass. In contrast, as discussed in section 2.2, nowadays dark matter dominated dwarf galaxies might once have contained larger fractions of baryons. This leads to the question whether the core growth observed figure 5.7 is reversed when baryons leave the galaxy. If it is not, the entire history of a galaxy has to be taken into account in order to predict its FDM core mass. In this regard, it might be interesting to simulate galaxies closer to the formation threshold caused by the UV background [59] or galaxies that form before the UV background sets in (possible fossils of reionization).

As long as dark matter does not reveal its nature in direct detection experiments, astrophysical observations remain important for dark matter research. Cosmic structure on small spatial scales and at high redshifts allows us to distinguish between models like WDM, SIDM and FDM, and our knowledge in these areas will certainly increase in the next century with upcoming ground based and space based telescopes like Large Synoptic Survey Telescope (LSST), James Webb Space Telescope (JWST), Wide Field Infrared Survey Telescope (WFIRST), Extremely Large Telescope (ELT) and Euclid. To mention only a few possibilities, the detection of faint and distant galaxies will constrain the luminosity function at high redshifts and at low luminosities with more accuracy. Resolving stellar populations, star formation histories of dwarf galaxies including their formation time can be reconstructed [181]. Apart from that, measurements of 3D velocities of individual stars in dwarf galaxies of the local group will constrain their underlying dark matter distribution in more detail and gravitational lensing observations potentially allow us to detect small dark matter halos independent of their baryonic content [182]. In summary, future observations will probably show if dark matter indeed consists of ultralight bosonic particles and cosmological FDM simulations like the ones presented in this thesis play a crucial role in this process.

References

[1] H.-Y. Schive, T. Chiueh, and T. Broadhurst, “Cosmic structure as the quantum interference of a coherent dark wave,” *Nature Physics*, 10, 496–499, Jul 2014.

[2] J. Veltmaat and J. C. Niemeyer, “Cosmological particle-in-cell simulations with ultralight axion dark matter,” *Phys. Rev. D*, 94, 123523, Dec. 2016.

[3] J. Veltmaat, J. C. Niemeyer, and B. Schwabe, “Formation and structure of ultralight bosonic dark matter halos,” *Phys. Rev. D*, 98, 043509, Aug. 2018.

[4] J. Veltmaat, B. Schwabe, and J. C. Niemeyer, “Baryon-driven growth of solitonic cores in fuzzy dark matter halos,” *Phys. Rev. D*, 101, 083518, Apr. 2020.

[5] C. G. Lacey and J. P. Ostriker, “Massive black holes in galactic halos?,” *ApJ*, 299, 633–652, Dec. 1985.

[6] C. Alcock, R. A. Allsman, D. R. Alves, T. S. Axelrod, A. C. Becker, D. P. Bennett, K. H. Cook, N. Dalal, A. J. Drake, K. C. Freeman, M. Geha, K. Griest, M. J. Lehner, S. L. Marshall, D. Minniti, C. A. Nelson, B. A. Peterson, P. Popowski, M. R. Pratt, P. J. Quinn, C. W. Stubbs, W. Sutherland, A. B. Tomaney, T. Vand ehei, and D. Welch, “The MACHO Project: Microlensing Results from 5.7 Years of Large Magellanic Cloud Observations,” *ApJ*, 542, 281–307, Oct 2000.

[7] EROS-2 Collaboration, “Limits on the Macho content of the Galactic Halo from the EROS-2 Survey of the Magellanic Clouds,” *A&A*, 469, 387–404, Jul 2007.

[8] T. D. Brandt, “Constraints on MACHO Dark Matter from Compact Stellar Systems in Ultra-faint Dwarf Galaxies,” *ApJ*, 824, L31, Jun 2016.

[9] P. Mocz, L. Lancaster, A. Fialkov, F. Becerra, and P.-H. Chavanis, "Schrödinger-Poisson-Vlasov-Poisson correspondence," *Phys. Rev. D*, 97, 083519, Apr 2018.

[10] E. Hubble, "A Relation between Distance and Radial Velocity among Extra-Galactic Nebulae," *Proceedings of the National Academy of Science*, 15, 168–173, Mar. 1929.

[11] R. A. Alpher, H. Bethe, and G. Gamow, "The Origin of Chemical Elements," *Physical Review*, 73, 803–804, Apr. 1948.

[12] A. A. Penzias and R. W. Wilson, "A Measurement of Excess Antenna Temperature at 4080 Mc/s.," *ApJ*, 142, 419–421, July 1965.

[13] E. R. Harrison, "Fluctuations at the threshold of classical cosmology," *Phys. Rev. D*, 1, 2726–2730, May 1970.

[14] Y. B. Zeldovich, "A hypothesis, unifying the structure and the entropy of the Universe," *MNRAS*, 160, 1P, 1972.

[15] A. H. Guth, "Inflationary universe: A possible solution to the horizon and flatness problems," *Phys. Rev. D*, 23, 347–356, Jan. 1981.

[16] A. D. Linde, "A new inflationary universe scenario: A possible solution of the horizon, flatness, homogeneity, isotropy and primordial monopole problems," *Physics Letters B*, 108, 389–393, Feb. 1982.

[17] F. Zwicky, "Die Rotverschiebung von extragalaktischen Nebeln," *Helvetica Physica Acta*, 6, 110–127, Jan 1933.

[18] V. Iršič, M. Viel, M. G. Haehnelt, J. S. Bolton, S. Cristiani, G. D. Becker, V. D'Odorico, G. Cupani, T.-S. Kim, and T. A. M. Berg, "New constraints on the free-streaming of warm dark matter from intermediate and small scale Lyman-α forest data," *Phys. Rev. D*, 96, 023522, Jul 2017.

[19] G. Efstathiou, W. J. Sutherland, and S. J. Maddox, "The cosmological constant and cold dark matter," *Nature*, 348, 705–707, Dec. 1990.

[20] G. F. Smoot, C. L. Bennett, A. Kogut, E. L. Wright, J. Aymon, N. W. Boggess, E. S. Cheng, G. de Amici, S. Gulkis, M. G. Hauser, G. Hinshaw, P. D. Jackson, M. Janssen, E. Kaita, T. Kelsall, P. Keegstra, C. Lineweaver, K. Loewenstein, P. Lubin, J. Mather, S. S. Meyer, S. H. Moseley, T. Murdock, L. Rokke, R. F. Silverberg, L. Tenorio, R. Weiss, and D. T. Wilkinson, "Structure in the COBE differential microwave radiometer first-year maps," *ApJ*, 396, L1–L5, Sept. 1992.

[21] S. Perlmutter, G. Aldering, G. Goldhaber, R. A. Knop, P. Nugent, P. G. Castro, S. Deustua, S. Fabbro, A. Goobar, D. E. Groom, I. M. Hook, A. G. Kim, M. Y. Kim, J. C. Lee, N. J. Nunes, R. Pain, C. R. Pennypacker, R. Quimby, C. Lidman, R. S. Ellis, M. Irwin, R. G. McMahon, P. Ruiz-Lapuente, N. Walton, B. Schaefer, B. J. Boyle, A. V. Filippenko, T. Matheson, A. S. Fruchter, N. Panagia, H. J. M. Newberg, and W. J. Couch, "Measurements of Ω and Λ from 42 High-Redshift Supernovae," *ApJ*, 517, 565–586, June 1999.

[22] A. G. Riess, A. V. Filippenko, P. Challis, A. Clocchiatti, A. Diercks, P. M. Garnavich, R. L. Gilliland, C. J. Hogan, S. Jha, R. P. Kirshner, B. Leibundgut, M. M. Phillips, D. Reiss, B. P. Schmidt, R. A. Schommer, R. C. Smith, J. Spyromilio, C. Stubbs, N. B. Suntzeff, and J. Tonry, "Observational Evidence from Supernovae for an Accelerating Universe and a Cosmological Constant," *AJ*, 116, 1009–1038, Sep 1998.

[23] SDSS collaboration, "The Fifteenth Data Release of the Sloan Digital Sky Surveys: First Release of MaNGA-derived Quantities, Data Visualization Tools, and Stellar Library," *ApJS*, 240, 23, Feb 2019.

[24] Planck Collaboration, "Planck 2018 results. VI. Cosmological parameters," *arXiv e-prints*, arXiv:1807.06209, Jul 2018.

[25] H. Mo, F. C. van den Bosch, and S. White, *Galaxy Formation and Evolution.* Cambridge University Press, May 2010.

[26] Y. B. Zel'dovich, "Gravitational instability: An approximate theory for large density perturbations.," *A&A*, 5, 84–89, Mar. 1970.

[27] J. E. Gunn and J. R. Gott, III, "On the Infall of Matter Into Clusters of Galaxies and Some Effects on Their Evolution," *ApJ*, 176, 1, Aug. 1972.

[28] W. H. Press and P. Schechter, "Formation of Galaxies and Clusters of Galaxies by Self-Similar Gravitational Condensation," *ApJ*, 187, 425–438, Feb. 1974.

[29] G. L. Bryan and M. L. Norman, "Statistical Properties of X-Ray Clusters: Analytic and Numerical Comparisons," *ApJ*, 495, 80–99, Mar. 1998.

[30] J. F. Navarro, C. S. Frenk, and S. D. M. White, "The Structure of Cold Dark Matter Halos," *ApJ*, 462, 563, May 1996.

[31] S. M. Faber and D. N. C. Lin, "Is there nonluminous matter in dwarf spheroidal galaxies," *ApJ*, 266, L17–L20, Mar. 1983.

[32] B. Binggeli, A. Sandage, and M. Tarenghi, "Studies of the Virgo Cluster. I - Photometry of 109 galaxies near the cluster center to serve as standards," *AJ*, 89, 64–82, Jan. 1984.

[33] A. W. Graham and R. Guzmán, "HST Photometry of Dwarf Elliptical Galaxies in Coma, and an Explanation for the Alleged Structural Dichotomy between Dwarf and Bright Elliptical Galaxies," *AJ*, 125, 2936–2950, Jun 2003.

[34] DES Collaboration, "Eight Ultra-faint Galaxy Candidates Discovered in Year Two of the Dark Energy Survey," *ApJ*, 813, 109, Nov 2015.

[35] J. S. Bullock and M. Boylan-Kolchin, "Small-Scale Challenges to the ΛCDM Paradigm," *ARA&A*, 55, 343–387, Aug 2017.

[36] B. Willman, J. J. Dalcanton, D. Martinez-Delgado, A. A. West, M. R. Blanton, D. W. Hogg, J. C. Barentine, H. J. Brewington, M. Harvanek, S. J. Kleinman, J. Krzesinski, D. Long, E. H. Neilsen, Jr., A. Nitta, and S. A. Snedden, "A New Milky Way Dwarf Galaxy in Ursa Major," *ApJ*, 626, L85–L88, June 2005.

[37] V. Belokurov, D. B. Zucker, N. W. Evans, J. T. Kleyna, S. Koposov, S. T. Hodgkin, M. J. Irwin, G. Gilmore, M. I. Wilkinson, M. Fellhauer, D. M. Bramich, P. C. Hewett, S. Vidrih, J. T. A. De Jong, J. A. Smith, H. W. Rix, E. F. Bell, R. F. G. Wyse, H. J. Newberg, P. A. Mayeur, B. Yanny, C. M. Rockosi, O. Y. Gnedin, D. P. Schneider, T. C. Beers, J. C. Barentine, H. Brewington, J. Brinkmann, M. Harvanek, S. J. Kleinman, J. Krzesinski, D. Long, A. Nitta, and S. A. Snedden, "Cats and Dogs, Hair and a Hero: A Quintet of New Milky Way Companions," *ApJ*, 654, 897–906, Jan 2007.

[38] V. Belokurov, M. G. Walker, N. W. Evans, G. Gilmore, M. J. Irwin, D. Just, S. Koposov, M. Mateo, E. Olszewski, L. Watkins, and L. Wyrzykowski, "Big Fish, Little Fish: Two New Ultra-faint Satellites of the Milky Way," *ApJ*, 712, L103–L106, Mar. 2010.

[39] J. C. Richardson, M. J. Irwin, A. W. McConnachie, N. F. Martin, A. L. Dotter, A. M. N. Ferguson, R. A. Ibata, S. C. Chapman, G. F. Lewis, and N. R. Tanvir, "PAndAS' Progeny: Extending the M31 Dwarf Galaxy Cabal," *ApJ*, 732, 76, May 2011.

[40] S. E. Koposov, V. Belokurov, G. Torrealba, and N. W. Evans, "Beasts of the Southern Wild: Discovery of Nine Ultra Faint Satellites in the Vicinity of the Magellanic Clouds.," *ApJ*, 805, 130, Jun 2015.

[41] DES Collaboration, "Eight New Milky Way Companions Discovered in First-year Dark Energy Survey Data," *ApJ*, 807, 50, Jul 2015.

[42] A. Klypin, A. V. Kravtsov, O. Valenzuela, and F. Prada, "Where Are the Missing Galactic Satellites?," *ApJ*, 522, 82–92, Sep 1999.

[43] B. Moore, S. Ghigna, F. Governato, G. Lake, T. Quinn, J. Stadel, and P. Tozzi, "Dark Matter Substructure within Galactic Halos," *ApJ*, 524, L19–L22, Oct 1999.

[44] M. Tegmark, J. Silk, M. J. Rees, A. Blanchard, T. Abel, and F. Palla, "How Small Were the First Cosmological Objects?," *ApJ*, 474, 1, Jan. 1997.

[45] T. Abel, P. Anninos, M. L. Norman, and Y. Zhang, "First Structure Formation. I. Primordial Star-forming Regions in Hierarchical Models," *ApJ*, 508, 518–529, Dec 1998.

[46] P. S. Behroozi, R. H. Wechsler, and C. Conroy, "The Average Star Formation Histories of Galaxies in Dark Matter Halos from z = 0-8," *ApJ*, 770, 57, Jun 2013.

[47] R. Kuzio de Naray, S. S. McGaugh, and W. J. G. de Blok, "Mass Models for Low Surface Brightness Galaxies with High-Resolution Optical Velocity Fields," *ApJ*, 676, 920–943, Apr 2008.

[48] M. G. Walker, M. Mateo, and E. W. Olszewski, "Stellar Velocities in the Carina, Fornax, Sculptor, and Sextans dSph Galaxies: Data From the Magellan/MMFS Survey," *AJ*, 137, 3100–3108, Feb. 2009.

[49] J. Wolf, G. D. Martinez, J. S. Bullock, M. Kaplinghat, M. Geha, R. R. Muñoz, J. D. Simon, and F. F. Avedo, "Accurate masses for dispersion-supported galaxies," *MNRAS*, 406, 1220–1237, Aug. 2010.

[50] J. D. Simon, M. Geha, Q. E. Minor, G. D. Martinez, E. N. Kirby, J. S. Bullock, M. Kaplinghat, L. E. Strigari, B. Willman, P. I. Choi, E. J. Tollerud, and J. Wolf, "A Complete Spectroscopic Survey of the Milky Way Satellite Segue 1: The Darkest Galaxy," *ApJ*, 733, 46, May 2011.

[51] E. N. Kirby, J. S. Bullock, M. Boylan-Kolchin, M. Kaplinghat, and J. G. Cohen, "The dynamics of isolated Local Group galaxies," *MNRAS*, 439, 1015–1027, Mar. 2014.

[52] C. M. Simpson, G. L. Bryan, K. V. Johnston, B. D. Smith, M.-M. Mac Low, S. Sharma, and J. Tumlinson, "The effect of feedback and reionization on

star formation in low-mass dwarf galaxy haloes," *MNRAS*, 432, 1989–2011, Jul 2013.

[53] J. Oñorbe, M. Boylan-Kolchin, J. S. Bullock, P. F. Hopkins, D. Kereš, C.-A. Faucher-Giguère, E. Quataert, and N. Murray, "Forged in FIRE: cusps, cores and baryons in low-mass dwarf galaxies," *MNRAS*, 454, 2092–2106, Dec 2015.

[54] C. R. Christensen, R. Davé, F. Governato, A. Pontzen, A. Brooks, F. Munshi, T. Quinn, and J. Wadsley, "In-N-Out: The Gas Cycle from Dwarfs to Spiral Galaxies," *ApJ*, 824, 57, June 2016.

[55] T. Sawala, C. S. Frenk, A. Fattahi, J. F. Navarro, R. G. Bower, R. A. Crain, C. Dalla Vecchia, M. Furlong, J. C. Helly, A. Jenkins, K. A. Oman, M. Schaller, J. Schaye, T. Theuns, J. Trayford, and S. D. M. White, "The APOSTLE simulations: solutions to the Local Group's cosmic puzzles," *MNRAS*, 457, 1931–1943, Apr 2016.

[56] L. Wang, A. A. Dutton, G. S. Stinson, A. V. Macciò, T. Gutcke, and X. Kang, "NIHAO VII: predictions for the galactic baryon budget in dwarf to Milky Way mass haloes," *MNRAS*, 466, 4858–4867, Apr 2017.

[57] C. Wheeler, P. F. Hopkins, A. B. Pace, S. Garrison-Kimmel, M. Boylan-Kolchin, A. Wetzel, J. S. Bullock, D. Kereš, C.-A. Faucher-Giguère, and E. Quataert, "Be it therefore resolved: Cosmological Simulations of Dwarf Galaxies with 30 Solar Mass Resolution," *MNRAS*, 2485, Oct 2019.

[58] G. Efstathiou, "Suppressing the formation of dwarf galaxies via photoionization," *MNRAS*, 256, 43P–47P, May 1992.

[59] T. Okamoto, L. Gao, and T. Theuns, "Mass loss of galaxies due to an ultraviolet background," *MNRAS*, 390, 920–928, Nov. 2008.

[60] T. M. Brown, J. Tumlinson, M. Geha, J. D. Simon, L. C. Vargas, D. A. VandenBerg, E. N. Kirby, J. S. Kalirai, R. J. Avila, M. Gennaro, H. C. Ferguson, R. R. Muñoz, P. Guhathakurta, and A. Renzini, "The Quenching of the Ultra-faint Dwarf Galaxies in the Reionization Era," *ApJ*, 796, 91, Dec. 2014.

[61] M. Ricotti and N. Y. Gnedin, "Formation Histories of Dwarf Galaxies in the Local Group," *ApJ*, 629, 259–267, Aug 2005.

[62] C. Wheeler, J. Oñorbe, J. S. Bullock, M. Boylan-Kolchin, O. D. Elbert, S. Garrison-Kimmel, P. F. Hopkins, and D. Kereš, "Sweating the small

stuff: simulating dwarf galaxies, ultra-faint dwarf galaxies, and their own tiny satellites," *MNRAS*, 453, 1305–1316, Oct 2015.

[63] J. S. Bullock, A. V. Kravtsov, and D. H. Weinberg, "Reionization and the Abundance of Galactic Satellites," *ApJ*, 539, 517–521, Aug. 2000.

[64] L. Mayer, C. Mastropietro, J. Wadsley, J. Stadel, and B. Moore, "Simultaneous ram pressure and tidal stripping; how dwarf spheroidals lost their gas," *MNRAS*, 369, 1021–1038, Jul 2006.

[65] R. A. Flores and J. R. Primack, "Observational and Theoretical Constraints on Singular Dark Matter Halos," *ApJ*, 427, L1, May 1994.

[66] B. Moore, "Evidence against dissipation-less dark matter from observations of galaxy haloes," *Nature*, 370, 629–631, Aug 1994.

[67] S. S. McGaugh and W. J. G. de Blok, "Testing the Dark Matter Hypothesis with Low Surface Brightness Galaxies and Other Evidence," *ApJ*, 499, 41–65, May 1998.

[68] W. J. G. de Blok, F. Walter, E. Brinks, C. Trachternach, S. H. Oh, and J. Kennicutt, R. C., "High-Resolution Rotation Curves and Galaxy Mass Models from THINGS," *AJ*, 136, 2648–2719, Dec 2008.

[69] G. Gilmore, M. I. Wilkinson, R. F. G. Wyse, J. T. Kleyna, A. Koch, N. W. Evans, and E. K. Grebel, "The Observed Properties of Dark Matter on Small Spatial Scales," *ApJ*, 663, 948–959, July 2007.

[70] J. Wolf and J. S. Bullock, "Dark matter concentrations and a search for cores in Milky Way dwarf satellites," *arXiv e-prints*, arXiv:1203.4240, Mar 2012.

[71] N. W. Evans, J. An, and M. G. Walker, "Cores and cusps in the dwarf spheroidals," *MNRAS*, 393, L50–L54, Feb 2009.

[72] M. G. Walker and J. Peñarrubia, "A Method for Measuring (Slopes of) the Mass Profiles of Dwarf Spheroidal Galaxies," *ApJ*, 742, 20, Nov 2011.

[73] J. R. Jardel, K. Gebhardt, M. H. Fabricius, N. Drory, and M. J. Williams, "Measuring Dark Matter Profiles Non-Parametrically in Dwarf Spheroidals: An Application to Draco," *ApJ*, 763, 91, Feb 2013.

[74] J. F. Navarro, V. R. Eke, and C. S. Frenk, "The cores of dwarf galaxy haloes," *MNRAS*, 283, L72–L78, Dec 1996.

[75] S. Mashchenko, H. M. P. Couchman, and J. Wadsley, “The removal of cusps from galaxy centres by stellar feedback in the early Universe,” *Nature*, 442, 539–542, Aug 2006.

[76] A. Pontzen and F. Governato, “How supernova feedback turns dark matter cusps into cores,” *MNRAS*, 421, 3464–3471, Apr 2012.

[77] E. Tollet, A. V. Macciò, A. A. Dutton, G. S. Stinson, L. Wang, C. Penzo, T. A. Gutcke, T. Buck, X. Kang, C. Brook, A. Di Cintio, B. W. Keller, and J. Wadsley, “NIHAO - IV: core creation and destruction in dark matter density profiles across cosmic time,” *MNRAS*, 456, 3542–3552, Mar 2016.

[78] A. Fitts, M. Boylan-Kolchin, O. D. Elbert, J. S. Bullock, P. F. Hopkins, J. Oñorbe, A. Wetzel, C. Wheeler, C.-A. Faucher-Giguère, D. Kereš, E. D. Skillman, and D. R. Weisz, “fire in the field: simulating the threshold of galaxy formation,” *MNRAS*, 471, 3547–3562, Nov 2017.

[79] J. I. Read, O. Agertz, and M. L. M. Collins, “Dark matter cores all the way down,” *MNRAS*, 459, 2573–2590, Jul 2016.

[80] A. Del Popolo and M. Le Delliou, “Small Scale Problems of the ΛCDM Model: A Short Review,” *Galaxies*, 5, 17, Feb 2017.

[81] A. El-Zant, I. Shlosman, and Y. Hoffman, “Dark Halos: The Flattening of the Density Cusp by Dynamical Friction,” *ApJ*, 560, 636–643, Oct 2001.

[82] A. A. El-Zant, Y. Hoffman, J. Primack, F. Combes, and I. Shlosman, “Flat-cored Dark Matter in Cuspy Clusters of Galaxies,” *ApJ*, 607, L75–L78, Jun 2004.

[83] M. Boylan-Kolchin, J. S. Bullock, and M. Kaplinghat, “Too big to fail? The puzzling darkness of massive Milky Way subhaloes,” *MNRAS*, 415, L40–L44, Jul 2011.

[84] M. Boylan-Kolchin, J. S. Bullock, and M. Kaplinghat, “The Milky Way’s bright satellites as an apparent failure of ΛCDM,” *MNRAS*, 422, 1203–1218, May 2012.

[85] A. A. Dutton, A. V. Macciò, J. Frings, L. Wang, G. S. Stinson, C. Penzo, and X. Kang, “NIHAO V: too big does not fail - reconciling the conflict between ΛCDM predictions and the circular velocities of nearby field galaxies,” *MNRAS*, 457, L74–L78, Mar 2016.

[86] A. R. Wetzel, P. F. Hopkins, J.-h. Kim, C.-A. Faucher-Giguère, D. Kereš, and E. Quataert, "Reconciling Dwarf Galaxies with ΛCDM Cosmology: Simulating a Realistic Population of Satellites around a Milky Way-mass Galaxy," *ApJ*, 827, L23, Aug 2016.

[87] M. Viel, J. Lesgourgues, M. G. Haehnelt, S. Matarrese, and A. Riotto, "Constraining warm dark matter candidates including sterile neutrinos and light gravitinos with WMAP and the Lyman-α forest," *Phys. Rev. D*, 71, 063534, Mar 2005.

[88] M. R. Lovell, C. S. Frenk, V. R. Eke, A. Jenkins, L. Gao, and T. Theuns, "The properties of warm dark matter haloes," *MNRAS*, 439, 300–317, Mar 2014.

[89] D. Anderhalden, A. Schneider, A. V. Macciò, J. Diemand, and G. Bertone, "Hints on the nature of dark matter from the properties of Milky Way satellites," *J. Cosmology Astropart. Phys.*, 2013, 014, Mar 2013.

[90] A. V. Macciò, S. Paduroiu, D. Anderhalden, A. Schneider, and B. Moore, "Cores in warm dark matter haloes: a Catch 22 problem," *MNRAS*, 424, 1105–1112, Aug 2012.

[91] D. N. Spergel and P. J. Steinhardt, "Observational Evidence for Self-Interacting Cold Dark Matter," *Phys. Rev. Lett.*, 84, 3760–3763, Apr 2000.

[92] O. D. Elbert, J. S. Bullock, M. Kaplinghat, S. Garrison-Kimmel, A. S. Graus, and M. Rocha, "A Testable Conspiracy: Simulating Baryonic Effects on Self-interacting Dark Matter Halos," *ApJ*, 853, 109, Feb 2018.

[93] W. Hu, R. Barkana, and A. Gruzinov, "Fuzzy Cold Dark Matter: The Wave Properties of Ultralight Particles," *Phys. Rev. Lett.*, 85, 1158–1161, Aug 2000.

[94] S.-J. Sin, "Late-time phase transition and the galactic halo as a bose liquid," *Phys. Rev. D*, 50, 3650–3654, Sep 1994.

[95] D. J. E. Marsh, "Nonlinear hydrodynamics of axion dark matter: Relative velocity effects and quantum forces," *Phys. Rev. D*, 91, 123520, Jun 2015.

[96] E. Madelung, "Quantentheorie in hydrodynamischer form," *Zeitschrift für Physik*, 40, no. 3-4, 322–326, 1927.

[97] T.-P. Woo and T. Chiueh, "High-Resolution Simulation on Structure Formation with Extremely Light Bosonic Dark Matter," *ApJ*, 697, 850–861, May 2009.

[98] D. J. E. Marsh, "Axion cosmology," *Phys. Rep.*, 643, 1–79, Jul 2016.

[99] F. S. Guzmán and L. A. Ureña-López, "Evolution of the schrödinger-newton system for a self-gravitating scalar field," *Phys. Rev. D*, 69, 124033, Jun 2004.

[100] H.-Y. Schive, M.-H. Liao, T.-P. Woo, S.-K. Wong, T. Chiueh, T. Broadhurst, and W. Y. P. Hwang, "Understanding the Core-Halo Relation of Quantum Wave Dark Matter from 3D Simulations," *Phys. Rev. Lett.*, 113, 261302, Dec 2014.

[101] S.-R. Chen, H.-Y. Schive, and T. Chiueh, "Jeans analysis for dwarf spheroidal galaxies in wave dark matter," *MNRAS*, 468, 1338–1348, Jun 2017.

[102] E. Calabrese and D. N. Spergel, "Ultra-light dark matter in ultra-faint dwarf galaxies," *MNRAS*, 460, 4397–4402, Aug 2016.

[103] D. J. E. Marsh and A.-R. Pop, "Axion dark matter, solitons and the cusp-core problem," *MNRAS*, 451, 2479–2492, Aug 2015.

[104] A. X. González-Morales, D. J. E. Marsh, J. Peñarrubia, and L. A. Ureña-López, "Unbiased constraints on ultralight axion mass from dwarf spheroidal galaxies," *MNRAS*, 472, 1346–1360, Dec 2017.

[105] T. Broadhurst, I. de Martino, H. Nhan Luu, G. F. Smoot, and S. H. H. Tye, "Ghostly Galaxies as Solitons of Bose-Einstein Dark Matter," *arXiv e-prints*, arXiv:1902.10488, Feb 2019.

[106] M. Safarzadeh and D. N. Spergel, "Ultra-light Dark Matter is Incompatible with the Milky Way's Dwarf Satellites," *arXiv e-prints*, arXiv:1906.11848, Jun 2019.

[107] T. Bernal, L. M. Fernández-Hernández, T. Matos, and M. A. Rodríguez-Meza, "Rotation curves of high-resolution LSB and SPARC galaxies with fuzzy and multistate (ultralight boson) scalar field dark matter," *MNRAS*, 475, 1447–1468, Apr 2018.

[108] N. Bar, D. Blas, K. Blum, and S. Sibiryakov, "Galactic rotation curves versus ultralight dark matter: Implications of the soliton-host halo relation," *Phys. Rev. D*, 98, 083027, Oct 2018.

[109] V. H. Robles, J. S. Bullock, and M. Boylan-Kolchin, "Scalar field dark matter: helping or hurting small-scale problems in cosmology?," *MNRAS*, 483, 289–298, Feb 2019.

[110] H. Deng, M. P. Hertzberg, M. H. Namjoo, and A. Masoumi, “Can light dark matter solve the core-cusp problem?,” *Phys. Rev. D*, 98, 023513, Jul 2018.

[111] V. Iršič, M. Viel, M. G. Haehnelt, J. S. Bolton, and G. D. Becker, “First Constraints on Fuzzy Dark Matter from Lyman-α Forest Data and Hydrodynamical Simulations,” *Phys. Rev. Lett.*, 119, 031302, Jul 2017.

[112] E. Armengaud, N. Palanque-Delabrouille, C. Yèche, D. J. E. Marsh, and J. Baur, “Constraining the mass of light bosonic dark matter using SDSS Lyman-α forest,” *MNRAS*, 471, 4606–4614, Nov 2017.

[113] L. Hui, J. P. Ostriker, S. Tremaine, and E. Witten, “Ultralight scalars as cosmological dark matter,” *Phys. Rev. D*, 95, 043541, Feb 2017.

[114] B. Bozek, D. J. E. Marsh, J. Silk, and R. F. G. Wyse, “Galaxy UV-luminosity function and reionization constraints on axion dark matter,” *MNRAS*, 450, 209–222, June 2015.

[115] H.-Y. Schive, T. Chiueh, T. Broadhurst, and K.-W. Huang, “Contrasting galaxy formation from quantum wave dark matter, ψdm, with λcdm, using planck AND hubble data,” *ApJ*, 818, 89, Feb 2016.

[116] A. Sarkar, R. Mondal, S. Das, S. Sethi, S. Bharadwaj, and D. J. Marsh, “The effects of the small-scale dm power on the cosmological neutral hydrogen (hi) distribution at high redshifts,” *J. Cosmology Astropart. Phys.*, 04, no. 04, 012, 2016.

[117] P. S. Corasaniti, S. Agarwal, D. J. E. Marsh, and S. Das, “Constraints on dark matter scenarios from measurements of the galaxy luminosity function at high redshifts,” *Phys. Rev. D*, 95, 083512, Apr 2017.

[118] R. J. Bouwens, G. D. Illingworth, P. A. Oesch, M. Trenti, I. Labbé, L. Bradley, M. Carollo, P. G. van Dokkum, V. Gonzalez, and B. Holwerda, “UV Luminosity Functions at Redshifts z 4 to z 10: 10,000 Galaxies from HST Legacy Fields,” *ApJ*, 803, 34, Apr 2015.

[119] X. Fan, M. A. Strauss, R. H. Becker, R. L. White, J. E. Gunn, G. R. Knapp, G. T. Richards, D. P. Schneider, J. Brinkmann, and M. Fukugita, “Constraining the Evolution of the Ionizing Background and the Epoch of Reionization with z˜6 Quasars. II. A Sample of 19 Quasars,” *AJ*, 132, 117–136, July 2006.

[120] J. D. Bowman, A. E. E. Rogers, R. A. Monsalve, T. J. Mozdzen, and N. Mahesh, “An absorption profile centred at 78 megahertz in the sky-averaged spectrum,” *Nature*, 555, 67–70, Mar 2018.

[121] A. Lidz and L. Hui, “Implications of a prereionization 21-cm absorption signal for fuzzy dark matter,” *Phys. Rev. D*, 98, 023011, July 2018.

[122] B. Bar-Or, J.-B. Fouvry, and S. Tremaine, “Relaxation in a Fuzzy Dark Matter Halo,” *arXiv e-prints*, arXiv:1809.07673, Sept. 2018.

[123] B. V. Church, J. P. Ostriker, and P. Mocz, “Heating of Milky Way disc Stars by Dark Matter Fluctuations in Cold Dark Matter and Fuzzy Dark Matter Paradigms,” *arXiv e-prints*, arXiv:1809.04744, Sept. 2018.

[124] N. C. Amorisco and A. Loeb, “First constraints on Fuzzy Dark Matter from the dynamics of stellar streams in the Milky Way,” *arXiv e-prints*, arXiv:1808.00464, Aug. 2018.

[125] D. J. E. Marsh and J. C. Niemeyer, “Strong Constraints on Fuzzy Dark Matter from Ultrafaint Dwarf Galaxy Eridanus II,” *Phys. Rev. Lett.*, 123, 051103, Aug 2019.

[126] X. Du, B. Schwabe, J. C. Niemeyer, and D. Bürger, “Tidal disruption of fuzzy dark matter subhalo cores,” *Phys. Rev. D*, 97, 063507, Mar 2018.

[127] C. Uhlemann, M. Kopp, and T. Haugg, “Schrödinger method as N-body double and UV completion of dust,” *Phys. Rev. D*, 90, 023517, Jul 2014.

[128] L. M. Widrow and N. Kaiser, “Using the Schroedinger Equation to Simulate Collisionless Matter,” *ApJ*, 416, L71, Oct 1993.

[129] D. G. Levkov, A. G. Panin, and I. I. Tkachev, “Gravitational Bose-Einstein Condensation in the Kinetic Regime,” *Phys. Rev. Lett.*, 121, 151301, Oct 2018.

[130] J. Binney and S. Tremaine, *Galactic Dynamics: Second Edition*. Princeton University Press, 2008.

[131] R. D. Peccei and H. R. Quinn, “CP conservation in the presence of pseudoparticles,” *Physical Review Letters*, 38, 1440–1443, Jun 1977.

[132] C. A. Baker, D. D. Doyle, P. Geltenbort, K. Green, M. G. D. van der Grinten, P. G. Harris, P. Iaydjiev, S. N. Ivanov, D. J. R. May, J. M. Pendlebury, J. D. Richardson, D. Shiers, and K. F. Smith, “Improved Experimental Limit on the Electric Dipole Moment of the Neutron,” *Phys. Rev. Lett.*, 97, 131801, Sep 2006.

[133] A. Arvanitaki, S. Dimopoulos, S. Dubovsky, N. Kaloper, and J. March-Russell, “String axiverse,” *Phys. Rev. D*, 81, 123530, Jun 2010.

[134] J. Preskill, M. B. Wise, and F. Wilczek, “Cosmology of the invisible axion,” *Physics Letters B*, 120, 127–132, Jan. 1983.

[135] P. Sikivie and Q. Yang, “Bose-Einstein Condensation of Dark Matter Axions,” *Phys. Rev. Lett.*, 103, 111301, Sep 2009.

[136] O. Erken, P. Sikivie, H. Tam, and Q. Yang, “Cosmic axion thermalization,” *Phys. Rev. D*, 85, 063520, Mar 2012.

[137] N. Banik, A. Christopherson, P. Sikivie, and E. M. Todarello, “The Rethermalizing Bose-Einstein Condensate of Dark Matter Axions,” *arXiv e-prints*, arXiv:1509.02081, Sep 2015.

[138] S. Barnett, K. Burnett, and J. Vaccaro, “Why a condensate can be thought of as having a definite phase,” *Journal of Research of the National Institute of Standards and Technology*, 101, 03 1997.

[139] W.-M. Zhang, “Coherent States in Field Theory,” *arXiv e-prints*, hep–th/9908117, Aug 1999.

[140] S. Davidson, “Axions: Bose Einstein condensate or classical field?,” *Astroparticle Physics*, 65, 101–107, May 2015.

[141] E. Schrödinger, “Der stetige Übergang von der Mikro- zur Makromechanik,” *Naturwissenschaften*, 14, 664–666, July 1926.

[142] A. H. Guth, M. P. Hertzberg, and C. Prescod-Weinstein, “Do dark matter axions form a condensate with long-range correlation?,” *Phys. Rev. D*, 92, 103513, Nov 2015.

[143] P. Sikivie and E. M. Todarello, “Duration of classicality in highly degenerate interacting Bosonic systems,” *Physics Letters B*, 770, 331–334, Jul 2017.

[144] G. Dvali and S. Zell, “Classicality and quantum break-time for cosmic axions,” *J. Cosmology Astropart. Phys.*, 2018, 064, Jul 2018.

[145] G. L. Bryan, M. L. Norman, B. W. O’Shea, T. Abel, J. H. Wise, M. J. Turk, D. R. Reynolds, D. C. Collins, P. Wang, S. W. Skillman, B. Smith, R. P. Harkness, J. Bordner, J.-h. Kim, M. Kuhlen, H. Xu, N. Goldbaum, C. Hummels, A. G. Kritsuk, E. Tasker, S. Skory, C. M. Simpson, O. Hahn, J. S. Oishi, G. C. So, F. Zhao, R. Cen, Y. Li, and The Enzo Collaboration, “ENZO: An Adaptive Mesh Refinement Code for Astrophysics,” *ApJS*, 211, 19, Apr. 2014.

[146] J. Butcher, *Numerical Methods for Ordinary Differential Equations.* Wiley, 2016.

[147] R. M. Caplan and R. Carretero-González, "Numerical Stability of Explicit Runge-Kutta Finite-Difference Schemes for the Nonlinear Schrödinger Equation," *arXiv e-prints*, arXiv:1107.4810, Jul 2011.

[148] W. Press, S. Teukolsky, W. Vetterling, and B. Flannery, *Numerical Recipes 3rd Edition: The Art of Scientific Computing.* Cambridge University Press, 2007.

[149] M. Frigo and S. G. Johnson, "The design and implementation of FFTW3," *Proceedings of the IEEE*, 93, no. 2, 216–231, 2005. Special issue on "Program Generation, Optimization, and Platform Adaptation".

[150] F. Edwards, E. Kendall, S. Hotchkiss, and R. Easther, "PyUltraLight: a pseudo-spectral solver for ultralight dark matter dynamics," *J. Cosmology Astropart. Phys.*, 2018, 027, Oct 2018.

[151] P. Mocz and S. Succi, "Numerical solution of the nonlinear schrödinger equation using smoothed-particle hydrodynamics," *Physical Review E*, 91, 053304, May 2015.

[152] M. Nori and M. Baldi, "AX-GADGET: a new code for cosmological simulations of Fuzzy Dark Matter and Axion models," *MNRAS*, 478, 3935–3951, Aug. 2018.

[153] P. F. Hopkins, "A stable finite-volume method for scalar field dark matter," *MNRAS*, 489, 2367–2376, Oct 2019.

[154] C. Trahan and R. Wyatt, *Quantum Dynamics with Trajectories: Introduction to Quantum Hydrodynamics.* Interdisciplinary Applied Mathematics, Springer New York, 2005.

[155] A. Benseny, D. Tena, and X. Oriols, "On the Classical Schrödinger Equation," *Fluctuation and Noise Letters*, 15, 1640011, Oct 2016.

[156] O. Hahn and T. Abel, "Multi-scale initial conditions for cosmological simulations," *MNRAS*, 415, 2101–2121, Jul 2011.

[157] J. M. Stone and M. L. Norman, "ZEUS-2D: A Radiation Magnetohydrodynamics Code for Astrophysical Flows in Two Space Dimensions. I. The Hydrodynamic Algorithms and Tests," *ApJS*, 80, 753, Jun 1992.

[158] F. Haardt and P. Madau, "Radiative Transfer in a Clumpy Universe. IV. New Synthesis Models of the Cosmic UV/X-Ray Background," *ApJ*, 746, 125, Feb. 2012.

[159] S. C. O. Glover and A. K. Jappsen, "Star Formation at Very Low Metallicity. I. Chemistry and Cooling at Low Densities," *ApJ*, 666, 1–19, Sept. 2007.

[160] R. C. Kennicutt, Jr., "The Global Schmidt Law in Star-forming Galaxies," *ApJ*, 498, 541–552, May 1998.

[161] R. Cen and J. P. Ostriker, "Galaxy formation and physical bias," *ApJ*, 399, L113–L116, Nov. 1992.

[162] N. Katz, "Dissipational Galaxy Formation. II. Effects of Star Formation," *ApJ*, 391, 502, Jun 1992.

[163] C. B. Hummels and G. L. Bryan, "Adaptive Mesh Refinement Simulations of Galaxy Formation: Exploring Numerical and Physical Parameters," *ApJ*, 749, 140, Apr 2012.

[164] J. Vicens, J. Salvado, and J. Miralda-Escudé, "Bosonic dark matter halos: excited states and relaxation in the potential of the ground state," *arXiv e-prints*, arXiv:1802.10513, Feb 2018.

[165] R. Hložek, D. J. E. Marsh, D. Grin, R. Allison, J. Dunkley, and E. Calabrese, "Future CMB tests of dark matter: Ultralight axions and massive neutrinos," *Phys. Rev. D*, 95, 123511, June 2017.

[166] B. Schwabe, J. C. Niemeyer, and J. F. Engels, "Simulations of solitonic core mergers in ultralight axion dark matter cosmologies," *Phys. Rev. D*, 94, 043513, Aug. 2016.

[167] P. Mocz, M. Vogelsberger, V. H. Robles, J. Zavala, M. Boylan-Kolchin, A. Fialkov, and L. Hernquist, "Galaxy formation with BECDM - I. Turbulence and relaxation of idealized haloes," *MNRAS*, 471, 4559–4570, Nov. 2017.

[168] K. Choi, C. Rott, and Y. Itow, "Impact of the dark matter velocity distribution on capture rates in the Sun," *J. Cosmology Astropart. Phys.*, 5, 049, May 2014.

[169] J. H. H. Chan, H.-Y. Schive, T.-P. Woo, and T. Chiueh, "How do stars affect ψDM haloes?," *MNRAS*, 478, 2686–2699, Aug 2018.

[170] K. G. Kay, “Integral expressions for the semiclassical time-dependent propagator,” *J. Chem. Phys.*, 100, 4377–4392, Mar. 1994.

[171] A. El-Zant, J. Freundlich, F. Combes, and A. Halle, “The effect of fluctuating fuzzy axion haloes on stellar dynamics: a stochastic model,” *arXiv e-prints*, arXiv:1908.09061, Aug 2019.

[172] P. Mocz, A. Fialkov, M. Vogelsberger, F. Becerra, M. A. Amin, S. Bose, M. Boylan-Kolchin, P.-H. Chavanis, L. Hernquist, L. Lancaster, F. Marinacci, V. H. Robles, and J. Zavala, “First star-forming structures in fuzzy cosmic filaments,” *Phys. Rev. Lett.*, 123, 141301, Oct 2019.

[173] L. Lancaster, C. Giovanetti, P. Mocz, Y. Kahn, M. Lisanti, and D. N. Spergel, “Dynamical Friction in a Fuzzy Dark Matter Universe,” *arXiv e-prints*, arXiv:1909.06381, Sep 2019.

[174] N. Bar, K. Blum, J. Eby, and R. Sato, “Ultralight dark matter in disk galaxies,” *Phys. Rev. D*, 99, 103020, May 2019.

[175] F. Lelli, S. S. McGaugh, and J. M. Schombert, “SPARC: Mass Models for 175 Disk Galaxies with Spitzer Photometry and Accurate Rotation Curves,” *AJ*, 152, 157, Dec 2016.

[176] O. Agertz, A. Pontzen, J. I. Read, M. P. Rey, M. Orkney, J. Rosdahl, R. Teyssier, R. Verbeke, M. Kretschmer, and S. Nickerson, “EDGE I: the mass-metallicity relation as a critical test of galaxy formation physics,” *arXiv e-prints*, arXiv:1904.02723, Apr 2019.

[177] A. Pillepich, V. Springel, D. Nelson, S. Genel, J. Naiman, R. Pakmor, L. Hernquist, P. Torrey, M. Vogelsberger, R. Weinberger, and F. Marinacci, “Simulating galaxy formation with the IllustrisTNG model,” *MNRAS*, 473, 4077–4106, Jan 2018.

[178] P. F. Hopkins, A. Wetzel, D. Kereš, C.-A. Faucher-Giguère, E. Quataert, M. Boylan-Kolchin, N. Murray, C. C. Hayward, S. Garrison-Kimmel, C. Hummels, R. Feldmann, P. Torrey, X. Ma, D. Anglés-Alcázar, K.-Y. Su, M. Orr, D. Schmitz, I. Escala, R. Sanderson, M. Y. Grudić, Z. Hafen, J.-H. Kim, A. Fitts, J. S. Bullock, C. Wheeler, T. K. Chan, O. D. Elbert, and D. Narayanan, “FIRE-2 simulations: physics versus numerics in galaxy formation,” *MNRAS*, 480, 800–863, Oct 2018.

[179] C. M. Simpson, G. L. Bryan, C. Hummels, and J. P. Ostriker, “Kinetic Energy from Supernova Feedback in High-resolution Galaxy Simulations,” *ApJ*, 809, 69, Aug 2015.

[180] M. C. Smith, D. Sijacki, and S. Shen, "Cosmological simulations of dwarfs: the need for ISM physics beyond SN feedback alone," *MNRAS*, 485, 3317–3333, May 2019.

[181] C. Evans, M. Puech, J. Afonso, O. Almaini, P. Amram, H. Aussel, B. Barbuy, A. Basden, N. Bastian, G. Battaglia, B. Biller, P. Bonifacio, N. Bouché, A. Bunker, E. Caffau, S. Charlot, M. Cirasuolo, Y. Clenet, F. Combes, C. Conselice, T. Contini, J.-G. Cuby, G. Dalton, B. Davies, A. de Koter, K. Disseau, J. Dunlop, B. Epinat, F. Fiore, S. Feltzing, A. Ferguson, H. Flores, A. Fontana, T. Fusco, D. Gadotti, A. Gallazzi, J. Gallego, E. Giallongo, T. Gonçalves, D. Gratadour, E. Guenther, F. Hammer, V. Hill, M. Huertas-Company, R. Ibata, L. Kaper, A. Korn, S. Larsen, O. Le Fèvre, B. Lemasle, C. Maraston, S. Mei, Y. Mellier, S. Morris, G. Östlin, T. Paumard, R. Pello, L. Pentericci, C. Peroux, P. Petitjean, M. Rodrigues, L. Rodríguez-Muñoz, D. Rouan, H. Sana, D. Schaerer, E. Telles, S. Trager, L. Tresse, N. Welikala, S. Zibetti, and B. Ziegler, "The Science Case for Multi-Object Spectroscopy on the European ELT," *arXiv e-prints*, arXiv:1501.04726, Jan 2015.

[182] J. Simon, S. Birrer, K. Bechtol, S. Chakrabarti, F.-Y. Cyr-Racine, I. Dell'Antonio, A. Drlica-Wagner, C. Fassnacht, M. Geha, D. Gilman, Y. D. Hezaveh, D. Kim, T. S. Li, L. Strigari, and T. Treu, "Testing the Nature of Dark Matter with Extremely Large Telescopes," *BAAS*, 51, 153, May 2019.

Related publications

Jan Veltmaat, Jens C. Niemeyer and Bodo Schwabe
Formation and structure of ultralight bosonic dark matter halos
Physical Review D
volume 98, id 043509
Aug. 2018

Jan Veltmaat, Bodo Schwabe, and Jens C. Niemeyer
Baryon-driven growth of solitonic cores in fuzzy dark matter halos
Physical Review D
volume 101, id 083518
Apr. 2020

Danksagung

Diese Dissertation wäre ohne die Hilfe und Unterstützung vieler Personen nicht möglich gewesen. Vielen Dank an Jens Niemeyer für das Angebot in der Kosmologiegruppe zu promovieren, die Idee für das Forschungsprojekt und die gute Betreuung bei der Umsetzung. Steffen Schumann möchte ich für eine zweite Meinung bei den Betreuungsausschusstreffen danken. Allen, auch ehemaligen Mitarbeitern in der Kosmologiegruppe gilt mein Dank für die vielen fachlichen und nicht-fachlichen Gespräche und Aktivitäten, die mir die Arbeit erleichtert haben. Besonders danke ich meinem langjährigen Schreibtischnachbarn Bodo Schwabe für die gute Zusammenarbeit bei der Modifizierung des enzo codes und dem Verfassen der Journalartikel. Many thanks to David Ellis for proofreading a large portion of this thesis. Zuletzt danke ich meiner Familie und Gaoyuan Wang für viele Dinge, insbesondere für die mentale Unterstützung in dunklen und in hellen Zeiten.